

Copyright

by

Noah Avram Mosberg

2013

The Thesis Committee for Noah Avram Mosberg
Certifies that this is the approved version of the following thesis:

**Experimental Investigation of the Performance of a Fully Cooled Gas
Turbine Vane with and without Mainstream Flow and Experimental
Analysis Supporting the Redesign of a Wind Tunnel Test Section**

APPROVED BY
SUPERVISING COMMITTEE:

Supervisor:

David Bogard

Halil Berberoglu

**Experimental Investigation of the Performance of a Fully Cooled Gas
Turbine Vane with and without Mainstream Flow and Experimental
Analysis Supporting the Redesign of a Wind Tunnel Test Section**

by

Noah Avram Mosberg, B.S.M.E.

Thesis

Presented to the Faculty of the Graduate School of
The University of Texas at Austin
in Partial Fulfillment
of the Requirements
for the Degree of

Master of Science in Engineering

The University of Texas at Austin
December 2013

Dedication

In memory of Deborah Weintrob.

Acknowledgements

First, I would like to give my thanks to Dr. David Bogard, who has given me an inestimable amount of guidance in the year-and-a-half I have worked in his laboratory. Thanks also to Dr. Halil Berberoglu for taking the time to help me improve this document. Also, I would like to thank Pratt & Whitney for funding the project that I worked on, giving me so many opportunities to learn and develop my expertise.

I would, of course, like to thank all of the people that I had the good fortune of working with at the Turbulence and Turbine Cooling Research Laboratory. Dr. Tom Dyson and Emily Boyd gave me advice and wisdom that could only have been attained through the years of tireless work they did and countless long nights they spent in the laboratory. Dave Kistenmacher, James Winka, John McClintic, and Josh Anderson all showed me just how much it was possible to learn in a mere year in the laboratory. I thank Robbie Stewart and Sean Klavetter for being unsurpassed role models in the department of work ethic. Special thanks to Kyle Chavez, who, working on the same project as me and being in many of the same classes, tolerated me despite seeing my face most of the hours of any given waking day. I also must thank the students whom I wish I had had the opportunity to get to know better: Gavin Packard, Adam Vaclavik, Gary Leung, and Jennifer Lin.

I give thanks to all of those who supported me outside of the laboratory and department. I thank my family: my brother, the realist; my father, who encouraged me to work hard and persevere; my mother, always the voice of calm and optimism, whom I will dearly miss. I thank Tara Patel for listening to me rant, rave, and gush about

anything and everything at all sorts of unreasonable hours. And finally, I give thanks to all of the others who helped make my time in Austin everything it has been.

Abstract

Experimental Investigation of the Performance of a Fully Cooled Gas Turbine Vane with and without Mainstream Flow and Experimental Analysis Supporting the Redesign of a Wind Tunnel Test Section

Noah Avram Mosberg, M.S.E.

The University of Texas at Austin, 2013

Supervisor: David Bogard

This study focused on experimentally determining the cooling performance of a fully cooled, scaled-up model of a C3X turbine vane. The primary objective was to determine the differences in overall effectiveness in the presence and absence of a hot mainstream flowing over the vane. Overall effectiveness was measured using a thermally scaled matched Biot number vane with an impingement plate providing the internal cooling. This is the first study focused on investigating the effect of removing the mainstream flow and comparing the contour and laterally-averaged effectiveness data in support of the development of an assembly line thermal testing method. It was found that the proposed method of factory floor testing of turbine component cooling performance did not provide comparable information to traditional overall effectiveness test methods.

A second experiment was performed in which the effect of altering the angle of attack of a flow into a passive turbulence generator was investigated. Measurements in the approach flow were taken using a single wire hot-wire anemometer. This study was

the first to investigate the effects such a setup would have on fluctuating flow quantitates such as turbulence intensity and integral length scale rather than simply the mean quantities. It was found that both the downstream turbulence intensity and the turbulence integral length scale increase monotonically with approach flow incidence angle at a specified distance downstream of the turbulence generator.

Table of Contents

List of Tables	xii
List of Figures	xiii
Nomenclature.....	xvii
Chapter 1: Introduction	1
1.1 Gas Turbine Efficiency	1
1.2 Gas Turbine Cooling	3
1.3 Experimental Measurement of Cooling Effect.....	5
1.4 Important Parameters in Turbine Component Cooling.....	8
1.4.1 Coolant Flow Parameters.....	9
1.4.2 Geometric Parameters.....	10
1.4.3 Mainstream Flow Parameters	11
1.5 Objectives of Current Study.....	12
Chapter 2: Experimental Facilities and Procedures	14
2.1 Experimental Facility Overview	14
2.1.1 Wind Tunnel.....	14
2.1.2 Secondary Flow Loop.....	17
2.1.3 Vane Model	19
2.1.4 Data Acquisition	23
2.2 Measurements for Overall Effectiveness Testing	23
2.2.1 Overall Effectiveness Test Setup.....	23
2.2.2 IR Camera Measurement	25
2.2.3 Thermocouple Measurement	27
2.2.4 Pressure Measurement.....	29
2.2.5 Experimental Procedure for Overall Effectiveness Study	30
2.2.6 Overall Effectiveness Data Processing.....	35
2.3 Measurements for Approach Flow Turbulence Testing.....	37
2.3.1 Approach Flow Test Setup	37
2.3.2 Hot Wire Anemometer Measurement of Approach Flow	41

2.3.3 Thermocouple Measurement of Approach Flow.....	43
2.3.4 Pressure Measurement.....	44
2.3.5 Experimental Procedure for Approach Flow Turbulence Testing.....	44
2.4 Experimental Uncertainty Analysis	49
2.4.1 Uncertainty in Overall Effectiveness Measurement Test Results	49
2.4.2 Uncertainty in Approach Flow Measurement Test Results.....	56
Chapter 3: Evaluation of Vane Cooling Performance with No Mainstream Flow	63
3.1 Purpose of No-Mainstream Overall Effectiveness Study	63
3.2 Discussion of Overall Effectiveness Results.....	65
3.2.1 Comparison of With-Mainstream Data to Prior Results	65
3.2.2 Comparison of No-Mainstream and With-Mainstream Cases	67
3.2.3 Discussion of No-Mainstream Results	74
3.3 Suggestions for Future Work in Testing of Vane Models in the Absence of a Mainstream.....	76
3.4 Overall Effectiveness Test Conclusions.....	77
Chapter 4: Design of a Turbulence Generator and Other Components in Support of a Wind Tunnel Test Section Redesign.....	79
4.1 Investigation of the Effect of Inlet Flow Incidence Angle on the Flow Downstream of a Turbulence Generator.....	79
4.1.1 Scope of Academic Literature	80
4.1.2 The Design of a Turbulence Generator to be used with Off-Normal Approach Angle Flow	83
4.1.3 Angled Turbulence Generator Test Experimental Results and Conclusions ...	89
4.1.4 Future Work in Quantifying the Turbulence Downstream of a Turbulence Generator with Off-Normal Approach Flow Angle	100
4.1.5 Wake Influence Test Experimental Results.....	102
4.1.6 Approach Flow Test Conclusions.....	106
4.2 Investigation of Total Pressure Losses within Different Segments of a Closed-Loop Wind Tunnel.....	107
4.3 Design of a Coolant Flow Loop Based on Test Article Blowing Ratio Requirements	110
4.4 Conclusions and Recommendations Regarding Total Pressure Measurements for Wind Tunnel Redesign.....	114

References.....	116
Vita.....	120

List of Tables

Table 2.1: Geometry specifications for film cooling holes.....	21
Table 2.2: Blowing ratio matrix for overall effectiveness tests.....	33
Table 2.3: Turbulence grid angle test matrix.....	37
Table 2.4: Sample blowing ratio uncertainty calculation.....	51
Table 2.5: Summary of uncertainty in nominal and showerhead blowing ratios.....	52
Table 2.6: Summary of uncertainty in mass flow rate.....	53
Table 4.1: Mean turbulence intensity for each angle and solidity tested.....	92
Table 4.2: Average integral length scales for each approach flow turbulence test configuration.....	99
Table 4.3: Total pressure losses within wind tunnel sections.....	108

List of Figures

Figure 1.1: The ideal Brayton cycle (Dagdas, Brayton Cycle: The Ideal Cycle for Gas Turbines, 2009).....	2
Figure 1.2: Cutaway of turbine blades showing internal cooling geometry (Hoffman, 2002)	4
Figure 1.3: External view of high pressure turbine blade showing film cooling geometry (YXLON, 2011).....	4
Figure 1.4: The development of turbine cooling has allowed for higher inlet temperatures (Han, Dutta, & Ekkad, 2013)	5
Figure 2.1: Closed-loop wind tunnel facility used in experiments	14
Figure 2.2: Wind tunnel test section schematic	15
Figure 2.3: Measurement of the C3X vane model pressure coefficient distribution (McClintic, 2013).....	16
Figure 2.4: Coolant flow loop diagram.....	18
Figure 2.5: Aft passage orifice plate calibration	19
Figure 2.6: Fully cooled C3X vane film cooling hole layout	20
Figure 2.7: Cameras positioned around midspan to enable full optical coverage	24
Figure 2.8: Installing a surface thermocouple at a hole exit to maximize its in-test temperature range.....	27
Figure 2.9: Typical thermocouple calibration curve.....	28
Figure 2.10: Constant temperature glycol bath used to calibrate thermocouples	29
Figure 2.11: Typical pressure transducer calibration.....	30

Figure 2.12: Laterally averaged effectiveness curve collapse at thermal steady state, variation over a 25-minute interval shown	32
Figure 2.13: Vane model showerhead and pressure side with locating lines	35
Figure 2.14: Example of the flattening of raw data into a contour plot.....	36
Figure 2.15: Turbulence grid setup schematic; 45d in black, and 0d in red	39
Figure 2.16: Schematic of local change in solidity due to the buckling of a single rod in the turbulence grid	39
Figure 2.17: Hot wire and Pitot probe location method.....	41
Figure 2.18: The A.A. Laboratory Systems AN-1003 hot wire anemometer system.....	42
Figure 2.19: Example image of a TSI 1210-10W single hot wire probe tip.....	42
Figure 2.20: Sample hot wire anemometer system response curve	45
Figure 2.21: Example hot wire test velocity multiplier curve fit.....	46
Figure 2.22: Sample in-test repeatability of laterally-averaged overall effectiveness using the P20 camera.....	55
Figure 2.23: Estimated bias uncertainty in hot wire calibration due to mainstream velocity measurement uncertainty	57
Figure 2.24: Mainstream temperature effect on hot wire calibration	59
Figure 2.25: Measured variation of mainstream temperature within the wind tunnel at $T_u \approx 6\%$, $U_\infty = 9.5$ m/s	61
Figure 3.1: Validation of current overall effectiveness experiment's results by comparison to previous laboratory results.....	66
Figure 3.2: Laterally averaged effectiveness data for both with-mainstream and no-mainstream cases	68

Figure 3.3: Subtractive and multiplicative difference between effectiveness values taken with and without mainstream.....	70
Figure 3.4: Heat transfer coefficient for an uncooled C3X vane, mainstream Tu = 20% (Dees, 2011).....	71
Figure 3.5: Effect of TBC on the overall effectiveness of a vane with round holes and an active showerhead (Davidson, Kistenmacher, & Bogard, 2012).....	72
Figure 3.6: Contour plots of overall effectiveness (A) $M^* = 2.0$, Mainstream OFF; (B) $M^* = 1.0$; Mainstream OFF; (C) $M^* = 2.0$, Mainstream ON; (D) $M^* = 1.0$, Mainstream ON.....	73
Figure 4.1: Common passive turbulence generator configurations: (A) Bi-planar square rods; (B) Perforated plate; (C) Planar rods	81
Figure 4.2: Flow angle defect caused by non-normal incident flow for a non-axisymmetric flow obstruction is avoided by using an element that is axisymmetric	84
Figure 4.3: Predicted turbulence integral length scales downstream of a passive turbulence generator (Roach, 1987).....	87
Figure 4.4: Transverse integral length scales as a function of normalized downstream distance from turbulence generator (Baines & Peterson, 1951)	88
Figure 4.5: Turbulence intensity across the width of the wind tunnel at different grid angle configurations at $x/b = 39.5$	90
Figure 4.6: Mean velocity profiles along traversing planes during turbulence quantity experiments	94
Figure 4.7: Increased velocity gradient magnitude across angled turbulence grid wakes	94

Figure 4.8: Turbulence intensity with downstream distance from a grid placed at 45 degrees with respect to the approach flow	95
Figure 4.9: Turbulence intensity correlation coefficient for varying distance downstream of a grid	97
Figure 4.10: Integral length scales measured across the width of a wind tunnel test section	99
Figure 4.11: Two wake simulation rod placements used in the wake destruction test... ..	104
Figure 4.12: Effect of an upstream wake on grid-generated turbulence intensity uniformity	105
Figure 4.13: Probe locations for wind tunnel total pressure loss measurements	108
Figure 4.14: Velocity downstream of turning vane section deviates from the expected value.....	110

Nomenclature

Symbols:

A	area
b	turbulence rod diameter
Bi	Biot number
C	chord length
C_d	discharge coefficient
C_p	pressure coefficient
d	diameter
DR	density ratio
h	heat transfer coefficient
H	vane height
I	momentum flux ratio
k	thermal conductivity
\dot{m}	mass flow rate
M	blowing ratio, turbulence rod spacing
N	number
p	hole pitch
P	pressure
R	ideal gas constant
R_{xx}	autocorrelation
Re	Reynolds number
s	surface stream-wise distance from stagnation line
t	time, wall thickness
T	temperature, integral time scale
Tu	turbulence level: u_{rms}/U
U	mean velocity
u_{rms}	root mean squared velocity
V	voltage
W	wind tunnel width
x	stream-wise coordinate, surface stream-wise distance from row of holes
y	spanwise coordinate
z	wall-normal coordinate

Greek:

β	ratio of orifice to pipe diameters
χ	coolant warming factor
δ	uncertainty, difference
Δ	change
ϕ	overall cooling effectiveness
γ	heat capacity ratio
η	adiabatic effectiveness
Λ_x	intergral length scale
ρ	density
τ	autocorrelation lag time

Subscripts and Accents:

<i>approach</i>	pertaining to the approach flow
<i>atm</i>	atmospheric
<i>aw</i>	adiabatic wall
<i>c</i>	coolant
<i>h</i>	coolant holes
<i>i</i>	vane inlet
<i>f</i>	with film cooling
<i>NM</i>	no mainstream
<i>o</i>	without film cooling, orifice
<i>p</i>	pipe
<i>PS</i>	pressure side
<i>SH</i>	showerhead
<i>solid</i>	blocked flow-normal area
<i>SS</i>	suction side
<i>static</i>	static
<i>t</i>	total
<i>w</i>	vane wall
∞	pertaining to the approach or mainstream flow
*	normalized by approach flow
-	laterally averaged, mean

Chapter 1: Introduction

1.1 Gas Turbine Efficiency

Gas turbines have become ubiquitous in the fields of modern aeronautical propulsion and land-based power generation, as they power virtually all modern passenger and military aircraft, and produced 20% of the electrical power generated in the United States in 2012 (U.S. Energy Information Administration, 2012). The amount of fuel consumed by gas turbines is correspondingly large, with nearly \$51 billion spent on jet fuel (Research and Innovative Technology Administration, 2012) and \$39 billion spent on fuel for natural gas land generators (U.S. Energy Information Administration, 2012) in 2012 in the United States alone. With such a vast amount of money being spent on fuel annually, even an incremental across-the-board increase in turbine efficiency would decrease annual fuel costs by millions of dollars. As such, turbine manufacturers continually push toward developing ever more efficient gas turbines with the goal of decreasing the cost of their operation, making their products a more attractive choice for potential customers.

The process by which a gas turbine does thermodynamic work most closely resembles the ideal Brayton cycle (Moran & Shapiro, 2008). There are three stages to a Brayton cycle: a compressor, a combustor, and a turbine. A working fluid, typically air, is fed into the compressor and raised to a higher pressure. This fluid is then sent to the combustor, where the fluid is mixed with fuel and combusted, thereby raising the fluid temperature. Finally, this hot high-pressure fluid is sent through a turbine, where it expands isentropically to generate shaft work within the system (Figure 1). In any type

of a gas turbine, the rotating compressor stage is powered by the rotation developed in the turbine stage. In a jet engine, the rotation of the turbine typically also drives a fan, which is used to propel the aircraft that it powers. In a land-based turbine, this rotation is instead used to generate electricity through an induction process.

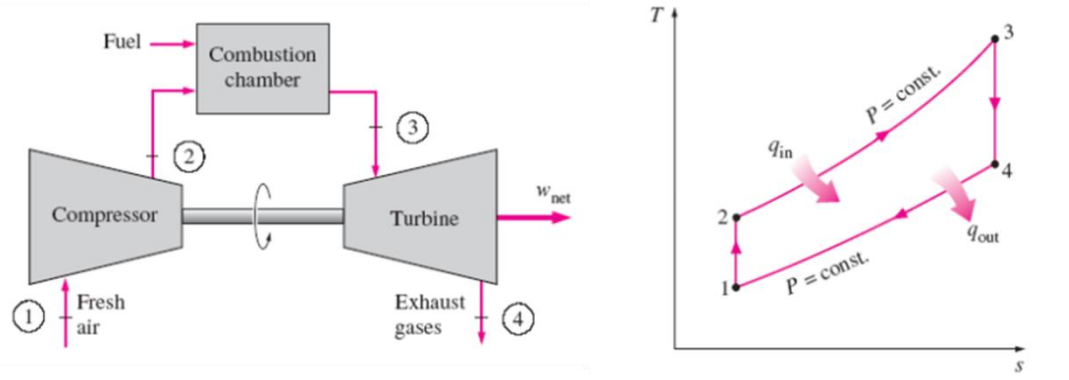


Figure 1.1: The ideal Brayton cycle (Dagdas, Brayton Cycle: The Ideal Cycle for Gas Turbines, 2009)

The thermodynamic efficiency of the Brayton cycle is a function of the pressure ratio (determined by the compressor) and the maximum temperature seen by the turbine (determined by the combustor). Efficiency increases monotonically with both of these values; as such, one of the major drives in increasing the efficiency of a gas turbine is in increasing the maximum temperature in the turbine stage. However, this does not simply entail developing hotter combustion processes, as the major limitation to turbine efficiency is not whatever temperature can be produced—rather, the key limitation is in creating turbine components that can survive the elevated temperatures downstream of the combustor. The temperature of the fluid coming out of the combustor can be in excess of 500 K above the melting temperature of the turbine blade and vane material (Special Metals, 2004). Therefore, these components require active cooling to ensure the

devices' sustained operation. Depending on the proximity of the particular component to the combustor, this involves either internal cooling or the combination of internal cooling and external film cooling.

1.2 Gas Turbine Cooling

Cooling of turbine blades and vanes is achieved by designing these components so that they contain internal channels through which coolant can be flowed (Figure 1.2). In addition to these internal channels, components that require the greatest amount of cooling also have film cooling holes, allowing coolant passing through the channels to be directed over the surface of the component (Figure 1.3). The holes are designed so that coolant ejected in this manner forms a cool, insulating film of fluid protecting the component from the hot mainstream surrounding it. The cooling fluid in a gas turbine is obtained by bleeding off a portion of the relatively cool fluid from the compressor and routing it through the blades and vanes. However, this bleed process has the effect of reducing the amount of mass flow that participates in the Brayton cycle, thereby reducing the maximum work that the device can produce. In maximizing the gas turbine's thermodynamic efficiency, it is therefore important to optimize all cooling configurations so that the turbine components can withstand the greatest temperatures while using the least amount of coolant.



Figure 1.2: Cutaway of turbine blades showing internal cooling geometry (Hoffman, 2002)

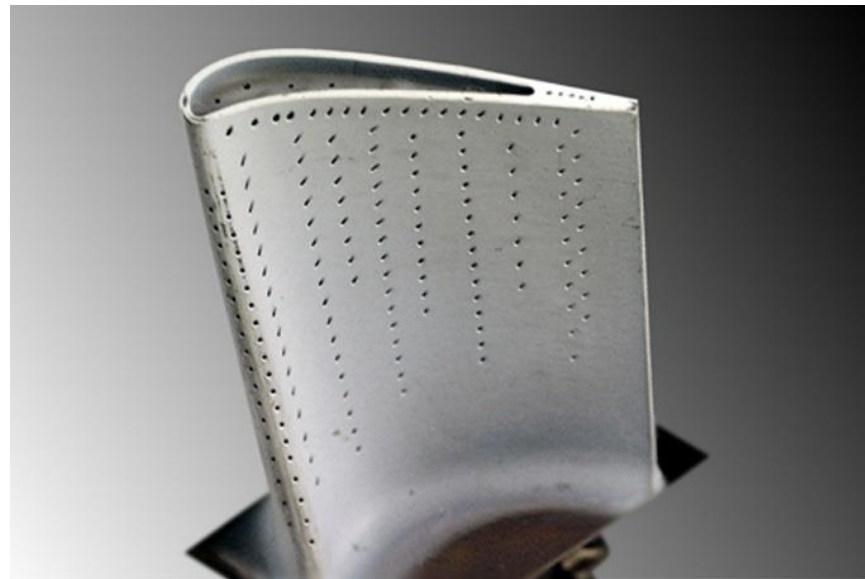


Figure 1.3: External view of high pressure turbine blade showing film cooling geometry (YXLON, 2011)

Cooling technology has become increasingly sophisticated over the decades since its inception (Figure 1.4). Internal cooling channels have evolved from being smooth to including various types of trips and turbulators designed to increase the internal heat

transfer coefficient, allowing for better cooling within the blade. Similarly, perforated plates can be placed inside of the channels so that coolant passing through the holes forms a jet that impinges on the inner surface of the blade, increasing the cooling effect. Major developments in film hole configurations include the introduction of diffuser-shaped holes that reduce the momentum of the film coolant jets, inducing them to stay attached to the blade or vane surface and provide better protection from the mainstream.

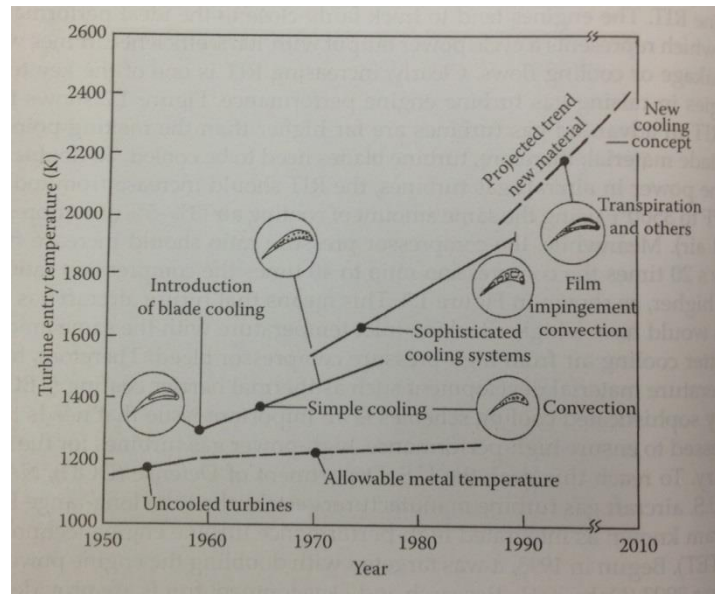


Figure 1.4: The development of turbine cooling has allowed for higher inlet temperatures (Han, Dutta, & Ekkad, 2013)

1.3 Experimental Measurement of Cooling Effect

The method and metrics for evaluating cooling performance are important in the development of new coolant schemes. One common metric for evaluating external cooling performance is adiabatic effectiveness:

$$\eta = \frac{T_{\infty} - T_{aw}}{T_{\infty} - T_c} \quad (1.1)$$

Here, T_∞ is the mainstream temperature, T_c is the coolant temperature at the hole exit, and T_{aw} is the adiabatic wall temperature. This quantity is representative of how well the surface of a model is cooled by film jets only: since the wall is adiabatic, the adiabatic wall temperature can only be affected by the external jet and mainstream temperatures. In other words, the adiabatic condition prevents coolant on the inside of a vane model from affecting the temperatures on the outside, isolating the film effect. Adiabatic effectiveness is a normalized temperature: when it is equal to 1, the adiabatic wall temperature is equal to the coolant temperature. When it is 0, the adiabatic wall temperature is equal to the mainstream temperature. It is important to recognize that adiabatic effectiveness is a local quantity: for example, its value will typically be closest to 1 nearer a film cooling hole exit, and closer to 0 further downstream or between individual film cooling jets. Since a real turbine blade or vane conducts thermally, the adiabatic wall temperature is not representative of a metal surface temperature that exists anywhere in a real engine. However, the adiabatic effectiveness gives a clear representation of the footprint of the film cooling jets and is useful in determining the worth of a particular film hole configuration. Adiabatic effectiveness is not explored in the studies presented in this document, but it is important to mention because of its widespread use and its relation to overall effectiveness:

$$\phi = \frac{T_\infty - T_w}{T_\infty - T_{c,i}} \quad (1.2)$$

Here, T_w refers to the external conducting wall temperature, and $T_{c,i}$ is the temperature of the coolant at the inlet of the test article. Note that the coolant temperature here is not the same as that used for the adiabatic effectiveness. Overall

effectiveness is a normalized local temperature, but instead of the wall in question being adiabatic, it is thermally conductive. Therefore, overall effectiveness is a metric for measuring the combined effect of internal and external cooling. One advantage of overall effectiveness is that it is a bottom-line result. It is a representation of the surface temperature of the part, and given information about the coolant temperature, mainstream temperature, and maximum acceptable wall temperature, the measured value for overall effectiveness can be compared to what is required to keep the part operational. It is also useful in identifying local hotspots, giving valuable information on how a cooling configuration might be improved. However, overall effectiveness also has some disadvantages: first, since the internal cooling has a strong effect and lateral conduction can cause jet profiles to “wash out” in IR images, it can be difficult to distinguish individual jet footprints more than a few diameters downstream of a given hole. This means that it is impossible to separate the contributions of the internal and film cooling schemes’ impact on the overall effectiveness. Overall effectiveness is also incomplete in that it provides no information about external heat transfer coefficients, which are important in determining heat flux into the turbine component. Disadvantages aside, it is a useful tool to obtain a good idea about how well a particular part will be cooled at engine conditions.

It is important to mention that by using 1-dimensional heat transfer analysis, the overall effectiveness can be expressed as follows:

$$\phi = \frac{1 - \chi\eta}{1 + Bi + \frac{h_f}{h_i}} + \chi\eta \quad (1.3)$$

In the above equation, χ is a factor representing the amount by which the coolant warms in a conducting blade between the blade plenum and the hole exit; the quotient $\frac{h_f}{h_i}$ is the ratio of external to internal heat transfer coefficients, which can be matched to engine conditions by matching the internal and external Reynolds numbers. The symbol Bi is the Biot number of the blade:

$$Bi = \frac{h_f t}{k} \quad (1.4)$$

In this formulation of the Biot number, k is the blade material's thermal conductivity; h_f is the convective heat transfer coefficient; and t is the blade's wall thickness.

This result implies that the overall effectiveness of an actual engine blade or vane can be determined by using a scaled model that matches the component's Biot number and the ratio of the external and internal heat transfer coefficients. This allows for scaled-up testing of overall effectiveness to take place, much in the way that is done for adiabatic effectiveness. A more complete treatment of the derivation of this form of the overall effectiveness can be found in the paper, *Adiabatic and Overall Effectiveness for a Film Cooled Blade* (Albert, Bogard, & Cunha, 2004).

1.4 Important Parameters in Turbine Component Cooling

There are several sets of parameters that are important in determining the effect of a particular turbine blade or vane cooling configuration. These sets of parameters could be divided into three separate categories: coolant flow parameters, geometric parameters, and mainstream flow parameters.

1.4.1 Coolant Flow Parameters

One of the main fluid flow parameters is the density ratio, which is simply the ratio of the density of the coolant air to the density of the mainstream:

$$DR = \frac{\rho_c}{\rho_\infty} \quad (1.5)$$

Here, ρ_c is the density of the coolant, and ρ_∞ is the density of the mainstream flow. The density ratio can impact cooling effectiveness because the relative densities of the coolants determines in part how the diffusion and mixing processes transpire between the coolant jet and the mainstream. A typical turbine blade cooling scheme operates at a nominal density ratio of 2.0. Experiments undertaken in this study were at a density ratio of $DR = 1.2$, which is somewhat lower than the 1.8 – 2.0 range typically seen in an engine. This unmatched quantity can be justified by the fact that effectiveness tends to increase with density ratio for a given blowing ratio or momentum flux ratio (each explained below), so the experiments run here could be considered a conservative estimate of real turbine vane operation (Pederson, Eckert, & Goldstein, 1977), (Sinha, Bogard, & Crawford, 1991).

Another important coolant flow parameter is the blowing ratio:

$$M = \frac{\rho_c V_c}{\rho_\infty V_\infty} \quad (1.6)$$

Here, V_c refers to the velocity of the coolant exiting a film hole, and V_∞ refers to the mainstream velocity at the hole location. This the ratio of the coolant and mainstream mass fluxes at the film cooling hole exit. This parameter is useful in scaling film effectiveness for a particular configuration; film effectiveness is more typically seen to

scale with blowing ratio when the jets stay attached to the wall. Similar to the blowing ratio is the momentum flux ratio, which is the ratio of the momentum of a film cooling jet to the momentum of the mainstream:

$$I = \frac{\rho_c V_c^2}{\rho_\infty V_\infty^2} \quad (1.7)$$

This parameter is useful in determining the scaling of cooling effectiveness when the jets have separated from the wall; jets of higher momentum flux ratio are more likely to separate. Although results in this study will not be presented in terms of the momentum flux ratio, it is useful for conceptualizing the setup of the experiments performed in chapter three.

1.4.2 Geometric Parameters

An additional set of important parameters that determine cooling effectiveness is the physical geometry of the coolant configuration itself. These parameters include the hole pitch relative to the hole diameter p/d ; the hole injection angle; any compound angle included in the hole injection; and, when applicable, the hole shape when it differs from a simple cylinder. The geometry of the part itself (e.g. its curvature) is also important in determining how well a particular coolant scheme will work; however, it is important to note that the coolant delivery design is based on the aerodynamic design of the blade or vane, and not the other way around.

1.4.2.1 Geometric Tolerances and Inspection

In light of how sensitive a particular coolant configuration's function is to its geometry, it is important to recognize that manufacturing defects and tolerances can impact the function of each individual blade differently as it leaves the manufacturing or

refurbishing facility. These blades will typically undergo heavy scrutiny in the quality assurance process to ensure that, for example, all the film cooling holes are “through” and free of blockage. However, this process is time- and labor-intensive, and does not quantify how the cooling effectiveness is impacted by the tolerances of the particular part (e.g. if a hot spot will occur on a particular blade whose holes are incorrectly angled, pitched, or sized). There is therefore a degree of incentive to add into the assembly line a system that would be able to evaluate the cooling effectiveness of every blade being manufactured at the facility.

1.4.3 Mainstream Flow Parameters

Another set of parameters important in determining how well a coolant configuration operates relates to fluid qualities of the mainstream flow itself. The mainstream flow seen by a first stage blade or vane is highly turbulent: a first stage vane regularly sees turbulence intensities as high as 20% (Han, Dutta, & Ekkad, 2013), (Koutmos & McGuirk, 1989), and the mainstream that reaches the blades just downstream has turbulence intensities of roughly 5% - 10% (Han, Dutta, & Ekkad, 2013). A mainstream with higher turbulence intensity will mix more rapidly with the film jets, decreasing their effectiveness at lower blowing ratios (Cutbirth, 2000). Another important turbulence quantity is the integral length scale of turbulent eddies within the mainstream. The length scale determines how the turbulence will interact with the jets: eddies that are large with respect to the diameter of a film cooling hole can have so strong an effect as to cause periodic variation of the spanwise position of the jet (Cutbirth, 2000). As such, when modeling the film cooling of an engine article, it is important to ensure that the mainstream flow conditions are comparable to the ones seen in an engine,

or else film effectiveness and heat transfer coefficient results will not be correctly captured.

1.4.3.1 Existing Research on Mainstream Flow Parameter Design

Many studies on wind tunnel turbulence generation have been performed that are relevant to this topic. Correlations relating turbulence intensity to normalized distance downstream of a passive turbulence generator have been developed by Baines and Peterson (1951) as well as Roach (1987). These correlations have been developed for a number of different turbulence generator geometries. Both of these studies are for flow coming in normal to the turbulence generator. Since data for these correlations was gathered along a line parallel to the mean flow direction, neither of these studies address turbulence quantity uniformity across the width of a tunnel. Similarly, analysis on how the mainstream mean velocity profile is affected by a turbulence generator has been performed by Laws and Livesey (1978) as well as Davis, (1962). However, only the uniformity of mean velocity values was investigated; no such attempt was made to quantify or qualify the uniformity of turbulent values.

1.5 Objectives of Current Study

The work described in Chapter 3 serves as an initial background investigation into how much useful information could be gathered from a system not making use of a wind tunnel in its evaluation of blade and vane cooling configuration effectiveness. To the author's knowledge, there have been no prior attempts to quantify the cooling effect of a turbine component in the absence of a mainstream.

Work described in Chapter 4 focuses on the development of a new turbulence generator designed to operate at various angles of approach flow attack. To the author's

knowledge, no study in the academic literature has been performed on the effect of angling the approach flow into the turbulence generator with respect to the turbulence generator plane's normal. Information on this effect would be useful, as different blade and vane designs have different target inlet angles. A new TTCRL wind tunnel design that will be able to accept different vane and blade models in the same test section will require the flow incoming to the turbulence generator to be at differing angles depending on the particular blade or vane model being tested. Therefore, a study of the effect of turbulence generator inlet angle on downstream turbulence intensity and length scale was needed to provide correlational data that would be used in the design of a turbulence generator for a given blade or vane design with an arbitrary angle of attack.

Chapter 2: Experimental Facilities and Procedures

2.1 Experimental Facility Overview

2.1.1 Wind Tunnel

A low-speed recirculating wind tunnel (Figure 2.1) was used as the test facility for all experiments described in this document. The flow loop was powered by an adjustable speed and blade pitch 50 horsepower axial fan. The test section was located in a wind tunnel corner to allow the test vane to turn the flow at this location, similar to how it would turn flow in typical turbine operation. The cross-section of the test section measured 40" in width and 21.6" in height.

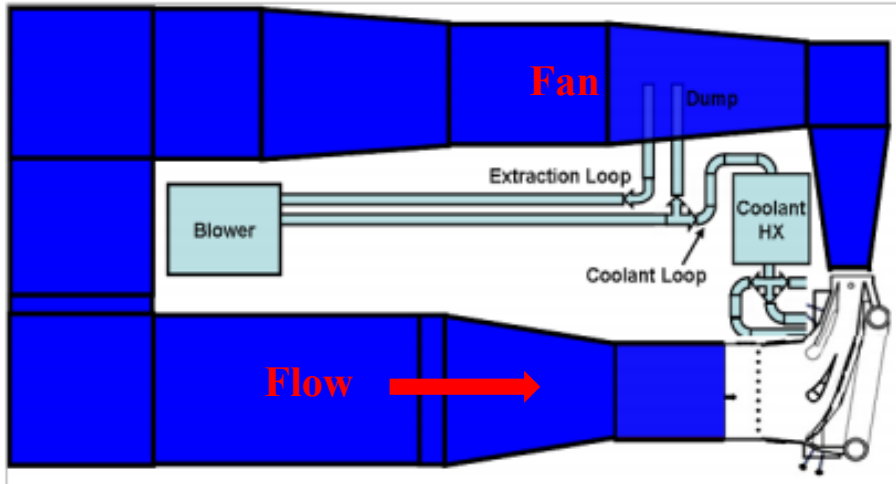


Figure 2.1: Closed-loop wind tunnel facility used in experiments

The test section consisted of a simulated 3-vane cascade (Figure 2.2). The cascade was used to simulate the way that adjacent vanes in a stage would affect one another's pressure distributions. The outer "vanes" consisted of leading edge models true to the geometry of the vane being tested, with the outer wall of the wind tunnel simulating the pressure side of the outer vane, and the inner wall of the wind tunnel

simulating the suction side of the inner vane. These outer walls were adjustable in order to be able to force the correct pressure distribution on the center airfoil (Figure 2.3). On the far sides of the inner and outer vanes were two bleed flow passages, which could be constricted to move the stagnation line on the outer airfoils to the correct position. Having the correct stagnation line location on these outer vanes assured that the correct amount of mass flow was flowing on either side of the center vane.

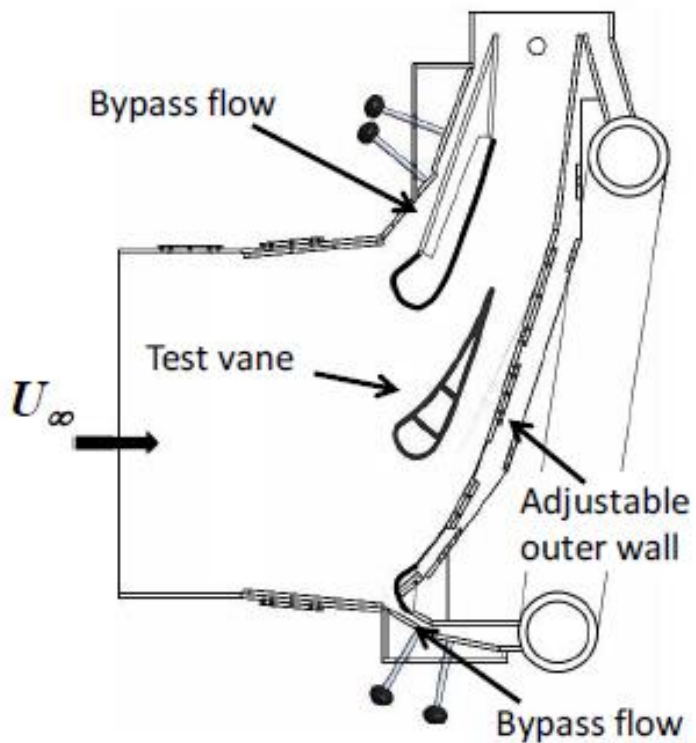


Figure 2.2: Wind tunnel test section schematic; 0° inlet angle

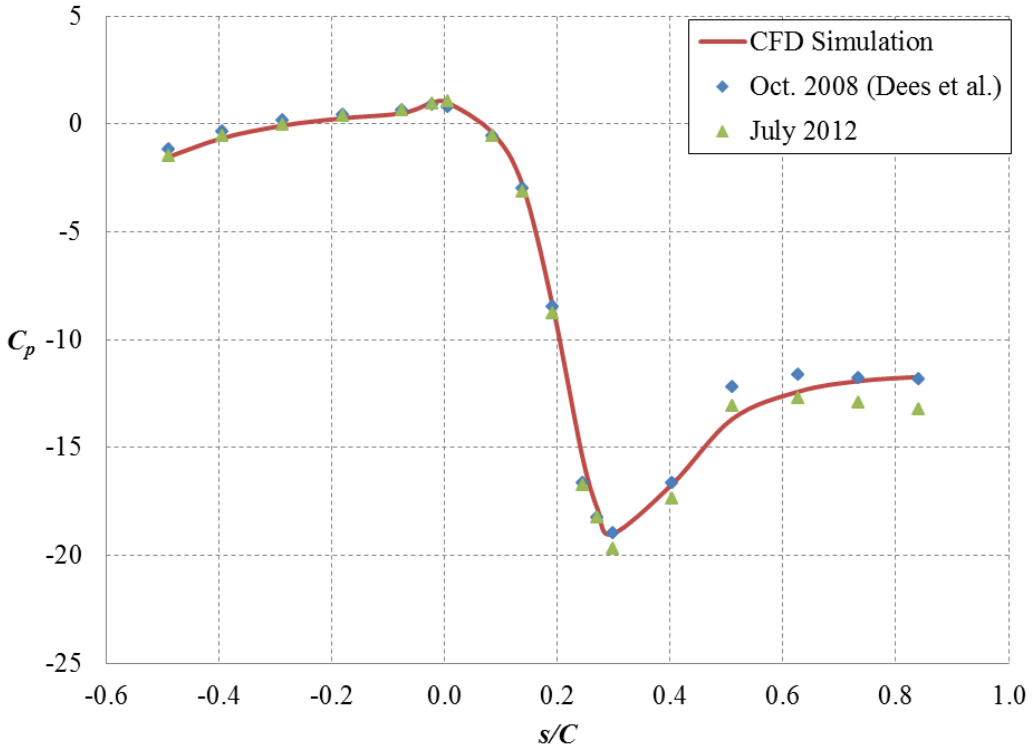


Figure 2.3: Measurement of the C3X vane model pressure coefficient distribution (McClintic, 2013)

The center vane was a complete aerodynamic model; this vane, described in greater detail in a following section, included a cooling configuration and relevant test instrumentation.

The velocity and temperature of the mainstream were measured during these experiments. Velocity measurements were used to support the calculation of blowing ratio in-test; mainstream temperature was measured to provide a reference temperature by which to extract the values for overall effectiveness. Two thermocouples were placed 18" upstream of the vane leading edge to measure the mainstream temperature throughout the duration of the overall effectiveness tests. These thermocouples were calibrated using the method described in section 2.2.3. The mainstream velocity was

measured approximately 4" downstream of the contraction nozzle that leads into the test section using a Pitot-static probe; the probe was placed at the mid-width of the tunnel, with the probe head extending 3" away from the tunnel wall.

The mainstream velocity and temperature were controlled using an operator-controlled open-loop system. The mainstream velocity was adjusted using the variable frequency drive linked to the wind tunnel's axial fan. Alternately, the mainstream velocity could be adjusted by altering the fan blade pitch in-situ. The mainstream temperature was adjusted using a fin-tube type heat exchanger that laid in-line with the wind tunnel mainstream flow. Water flowed through the heat exchanger, altering the temperature of the flow passing over it. The water temperature was adjusted manually using hot and cold water taps.

2.1.2 Secondary Flow Loop

A secondary flow loop (Figure 2.4) was used to deliver coolant to the vane model during the overall effectiveness tests. The positive pressure differential in this loop was created using a 5.6 kW constant speed centrifugal blower capable of generating roughly 8.2 kPa of static pressure at the coolant flow rates used during testing. The blower pulled air from the wind tunnel, pressurized it, and delivered it into a heat exchanger where it was cooled using liquid nitrogen. The liquid nitrogen was supplied to this heat exchanger from pressurized tanks. This air-nitrogen mixture in the heat exchanger was then sent through two 2 ½-inch schedule 40 PVC pipes, one of which led to the fore internal channel of the test vane, and the other of which led to the aft internal channel of the test vane.

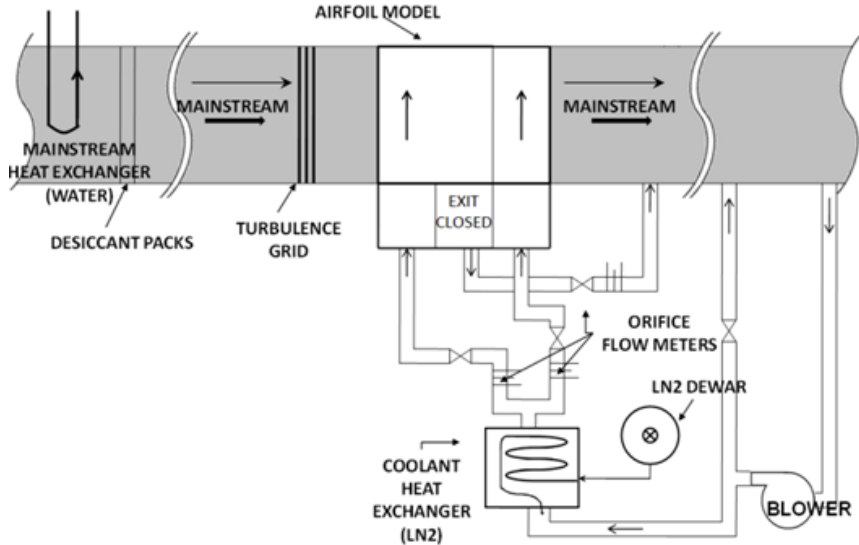


Figure 2.4: Coolant flow loop diagram

The coolant mass flow rate in each channel was metered using an orifice meter with a diameter ratio of $\beta = 0.85$. The pressure differential across the orifice plate was measured, as were the local fluid temperature and static pressure, which enabled a calculation of the fluid density using the ideal gas properties for nitrogen. Each of the orifice plates used in these experiments were calibrated in-situ (Figure 2.5) using a laminar flow element as the standard. A sixth-order fit was applied to the relation between C_d and Re_d ; this resulted in a calibration that could not be accurately extrapolated past a pipe Reynolds number range of about 10,000 $Re_d < 100,000$. However, this proved to be unimportant, since the pipe Reynolds number remained in the range of about 40,000 $< Re_d < 60,000$ throughout the course of all experiments. The coolant flow rates measured using the orifice meters were used in concert with mass flow splits determined by Dyson (2012) to calculate the blowing ratio for each row of holes for the vane model being used.

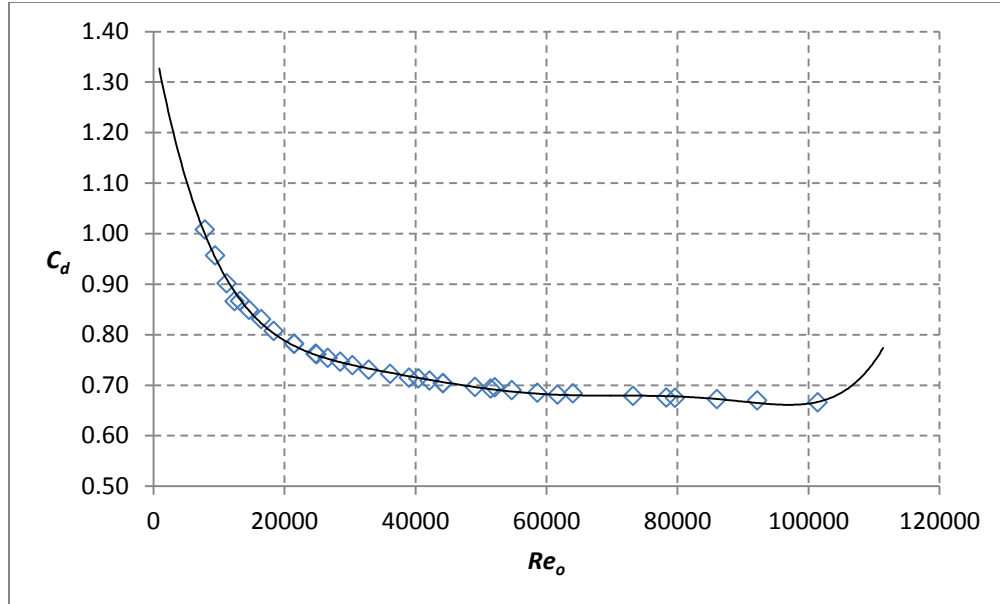


Figure 2.5: Aft passage orifice plate calibration

An inlet channel was installed in line with the coolant flow loop just upstream of the test vane. This inlet channel had channels of the same internal dimensions as the internal cooling passages of the vane article in order to allow the flow to develop fully prior to entering the test vane. Perforated plates and screens were installed in the channel to ensure that the incoming flow velocity would be uniform (Dees, 2010).

Coolant flow rate in the secondary flow loop was adjusted manually using Nibco T-134 gate valves. This in-situ adjustment of mass flow allowed for multiple blowing ratios to be tested during a single experiment.

2.1.3 Vane Model

A relatively complex fully-cooled conducting NASA C3X first stage vane model was used in overall effectiveness experiments to simulate a turbine vane in actual engine conditions (Figure 2.6). The vane model was an extrusion of the shape of the actual

vane's midspan profile. The vane model had two internal cooling passages: a purely radial passage in the aft section of the blade with no turbulators, and an impingement cavity in the fore section of the vane. The fore section (Figure 2.6) fed a showerhead consisting of five rows of holes plus two rows of smaller gill holes; this fore section also fed two rows placed on the suction side of the vane, and two rows of holes placed on the pressure side of the vane. The aft passage fed two rows of holes on the pressure side of the vane.

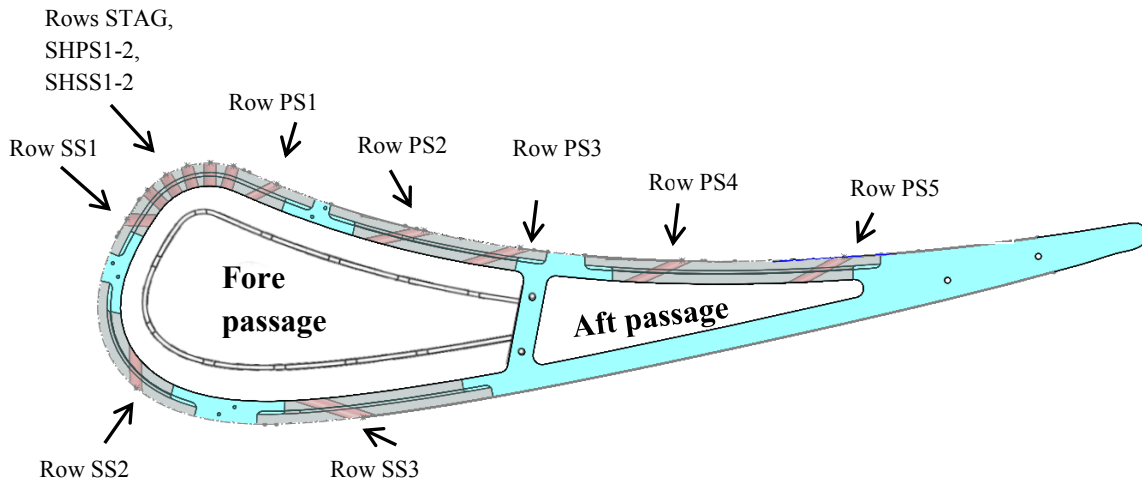


Figure 2.6: Fully cooled C3X vane film cooling hole layout

A table detailing the diameters, pitches, locations, and angles of the holes is found below (Table 2.1).

Table 2.1: Geometry specifications for film cooling holes

Row Name	Position (s/C)	Surface Angle (°)	Compound Angle (°)	d (mm)	Pitch (p/d)	Number of Holes
PS5	-0.68	25	0	4.78	5.3	13
PS4	-0.52	25	0	4.78	5.3	14
PS3	-0.35	25	0	4.78	5.3	13
PS2	-0.25	25	0	4.78	5.3	14
PS1	-0.096	30	60	4.78	5.3	13
SH-PS2	-0.048	25	90	6.35	6	9
SH-PS1	-0.024	25	90	6.35	6	8
SH-Stag	0.0	25	90	6.35	6	9
SH-SS1	0.024	25	90	6.35	6	8
SH-SS2	0.048	25	90	6.35	6	9
SS1	0.084	35	68	6.35	4	13
SS2	0.28	30	60	6.35	4	13
SS3	0.51	30	0	6.35	4	13

The model was scaled to have a true chord length of $C = 531$ mm, an axial chord length of $C_{ax} = 330$ mm, and a height of $H = 547$ mm, equal to the height of the wind tunnel test section. These dimensions correspond to a 15.52-scale version of the original C3X vane geometry. To scale the model thermally, a wall thickness of 12.7 mm was used, and the model was made of DuPont™ Corian® ($k = 1.0 \pm 0.1$ W/m-K) to match the Biot number to ensure that the overall effectiveness values would be representative of cooling effect in a real engine part. The expected value of the area-averaged external heat transfer coefficient at engine conditions was assumed to be $h_f = 5850$ W/m²-K, a

typical value for a first-stage turbine vane (Bunker, 2009). Since the value of the external heat transfer coefficient would be expected to exhibit strong spatial variation over the surface of the vane, the assumed range of local external heat transfer coefficients was assumed to be $1000 < h_f < 10000 \text{ W/m}^2\text{-K}$ (McClintic, 2013). The thickness of the airfoil wall was assumed to be $t = 2 \text{ mm}$, and the thermal conductivity of the engine part was assumed to be $k \approx 20 \text{ W/m-K}$ (Special Metals, 2004). This yielded a range of possible engine part Biot numbers between $0.1 < Bi < 1.0$. Experiments performed on the vane model used in these experiments showed a range of external heat transfer coefficients between $40 < h_f < 110 \text{ W/m}^2\text{-K}$. This, combined with the thermal conductivity of the Corian® and the model wall thickness yielded model Biot numbers in a range of $0.5 < Bi < 1.4$. An internal impingement cooling scheme designed to match the heat transfer coefficient ratio h_f/h_i was developed by TTCRL researcher Tom Dyson. Recall from section 1.3 that the overall effectiveness is a function of the Biot number, the adiabatic effectiveness, and this same heat transfer coefficient ratio, hence the basis for setting this quantity to match the engine conditions. It is worth noting that impingement cooling was only used in the vane's fore cavity; the aft passage was a purely radial channel using no turbulators, and therefore probably had a significantly reduced internal heat transfer coefficient. In this region, the heat transfer coefficient ratio may not have been matched. However, the regions where data was gathered in this experiment focused on the film rows fed by the impingement-fed passage, so this shortcoming is not considered to be problematic for the purposes of this study.

2.1.4 Data Acquisition

Data acquisition was managed using VIs written for National Instruments LabVIEW 2011. Voltage data from thermocouples was obtained using NI SCXI 1102 units; these units utilize a reference thermistor against to which the thermocouple junction voltage is compared in order to get a thermocouple temperature output. Voltage data from all other sources (e.g. pressure transducers, hot wire anemometer output) was obtained through an NI 1100 unit. Each of these units is capable of obtaining single-channel data at a rate of 166 kS/s. The data was multiplexed using an NI SCXI 1000 multiplexing chassis, which can interpret and send data to a data acquisition device from any combination of four of the voltage input units described above. The DAQ card used in this setup was an NI PCIe-6321 X-series data acquisition device with 16 bit resolution over a ± 10 V range. With the exception of hot wire data, measurements on all channels were taken at 1000 Hz for 1 second and averaged to provide representative instantaneous data.

2.2 Measurements for Overall Effectiveness Testing

2.2.1 Overall Effectiveness Test Setup

To help ensure that no coolant would leak between the location of the coolant mass flow measurements and the exits of the holes in the vane model, the vane model was bolted to the plenum, using a gasket and high vacuum grease to form an airtight seal in between.

Infrared cameras were placed outside of the tunnel and aimed at the midspan of the vane model (Figure 2.7). Salt crystal windows were used to allow infrared radiation

emanating from the vane model to reach the cameras. The salt crystal windows used had acceptable transmissivity over the 7-14 μm range, encompassing the entire band of wavelengths over which the cameras could measure. The cameras were placed so that the views of the cameras provided continuous chord-wise coverage of the vane model for the values of x/C being investigated. In this way, contour plots and charts expressing laterally averaged overall effectiveness along the vane could be produced without any gaps in the data.

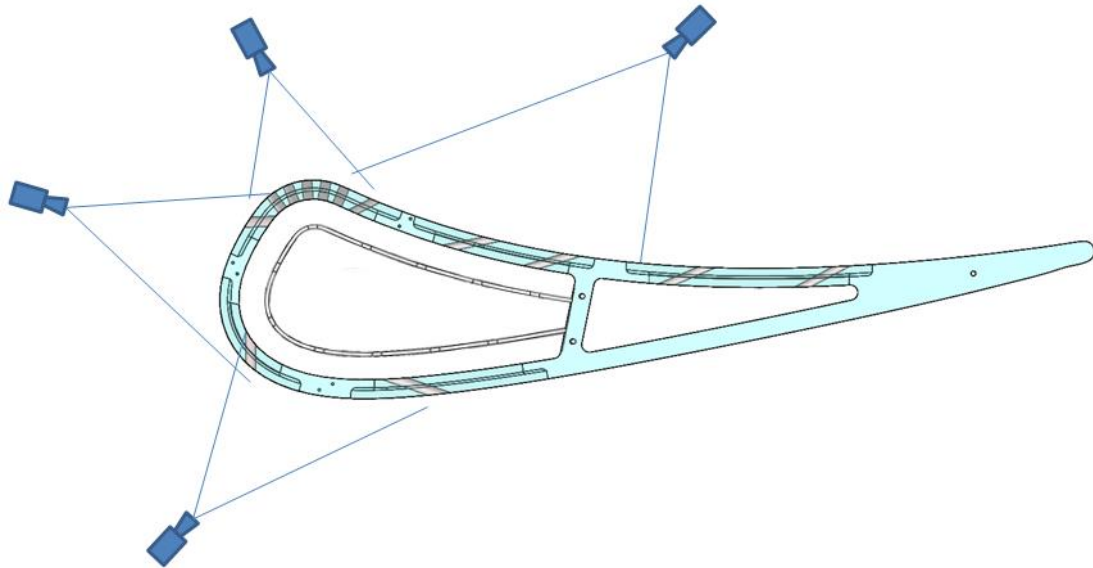


Figure 2.7: Cameras positioned around midspan to enable full optical coverage

A turbulence generator designed to produce 20% turbulence intensity and integral length scale $\Lambda_x = 37$ mm was installed upstream of the vane model. This was done to ensure that the approach flow had turbulence characteristics equivalent to what a C3X vane would see in actual engine conditions. Tests of turbulence quantity uniformity were performed by Polanka (1999) and validated later by Pichon (2009). The turbulence intensity at a plane 0.07 C upstream of the leading edge of the vane model was not

constant across the width of the tunnel due to the impact of the vanes on the upstream mean velocity profile, but had a mean turbulence intensity of 20%. The RMS velocities were uniform across the width of the tunnel indicating proper performance of the turbulence generator. Note that for the no-mainstream condition of the overall effectiveness tests, this turbulence generator would not in fact be producing any turbulence, since there would be no mainstream that would allow the individual rods to generate wakes. Therefore, a single test setup allowed for the vane model to be tested as though it were on an assembly line with no mainstream flow, and then also at actual engine conditions with a highly turbulent approach flow.

In order to prevent the formation of frost inside or on the surface of the vane model, which could divert the coolant flow and cause unrealistic results, desiccant packs were used to absorb the humidity of the mainstream air. These packs were placed just downstream of the axial fan powering the wind tunnel; due to their being so far upstream of the test section and there being multiple screens downstream, the insertion of this material into the wind tunnel had no impact on the test section aerodynamics. These desiccant packs were put into the wind tunnel prior to beginning the test in order to avoid having to open the wind tunnel partway through the experiment.

2.2.2 IR Camera Measurement

Surface temperature measurements in the overall effectiveness experiments were taken using FLIR P20 and FLIR T-620 infrared cameras. These cameras were calibrated in-situ during each experiment against ribbon E-type thermocouples that were placed at multiple locations on the surface of the vane model within view of the cameras. The surface thermocouples were placed near the exits of film cooling holes so that they would

be exposed to the coldest possible temperatures (Figure 2.8), thereby allowing the camera to be calibrated across the entire range of temperatures that it would see in a given experiment. These thermocouples were installed permanently so that calibrations could be performed in-situ for every experiment. The method of using the thermocouples on the surface of the vane model and calibrating the cameras in-situ makes it possible to remove any measurement bias that would be caused by incident radiation from the test section walls. This radiation reflects off of the test article surface and influences the temperature recorded by the camera. By correlating the radiation surface temperature that the camera sees to the actual surface temperature that the thermocouples experience, this source of bias is automatically accounted for during data processing. Additionally, any source of bias incurred by taking images through a salt crystal window is also removed by calibrating in this fashion. Painting the vane surface and thermocouples flat black maximizes the test article emissivity, thereby mitigating any incident radiation reflection into the camera and maximizing the thermal radiation output of the test article.

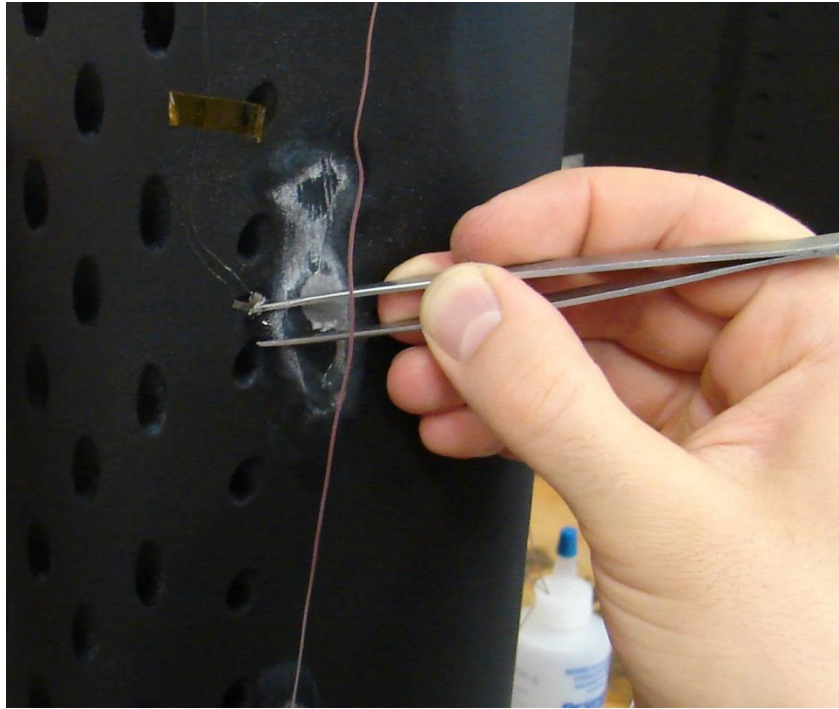


Figure 2.8: Installing a surface thermocouple at a hole exit to maximize its in-test temperature range

A non-uniformity correction (NUC) was applied prior to taking each IR image. The non-uniformity correction is a way of re-determining the calibration for individual pixels within the camera's microbolometer detector array, as they can individually or collectively drift with time. This is done by exposing the detector array to a shutter held at a known constant temperature; the zero of each of the pixels is then readjusted based on this measurement. This process takes place entirely within the confines of the camera, and is activated manually by depressing a button on the camera chassis. Legacy work within the TTCRL had demonstrated that performing a NUC prior to each image prevented temperature bias errors from occurring from one image to the next.

2.2.3 Thermocouple Measurement

Thermocouples used in the camera calibration were calibrated against a high-accuracy thermistor (Figure 2.9). The thermistor and the thermocouples were placed in a

temperature-controlled glycol bath (Figure 2.10) and calibrated down to 248 K, the lowest temperature that the bath was able to support. The thermocouples were connected to the same data acquisition ports for the calibration as in the actual overall effectiveness experiment. This was done to ensure that any bias in voltage reading (and therefore also temperature reading) that would be incurred by changing the port could be avoided.

Thermocouples used to measure coolant and mainstream temperature were calibrated in the same manner described above.

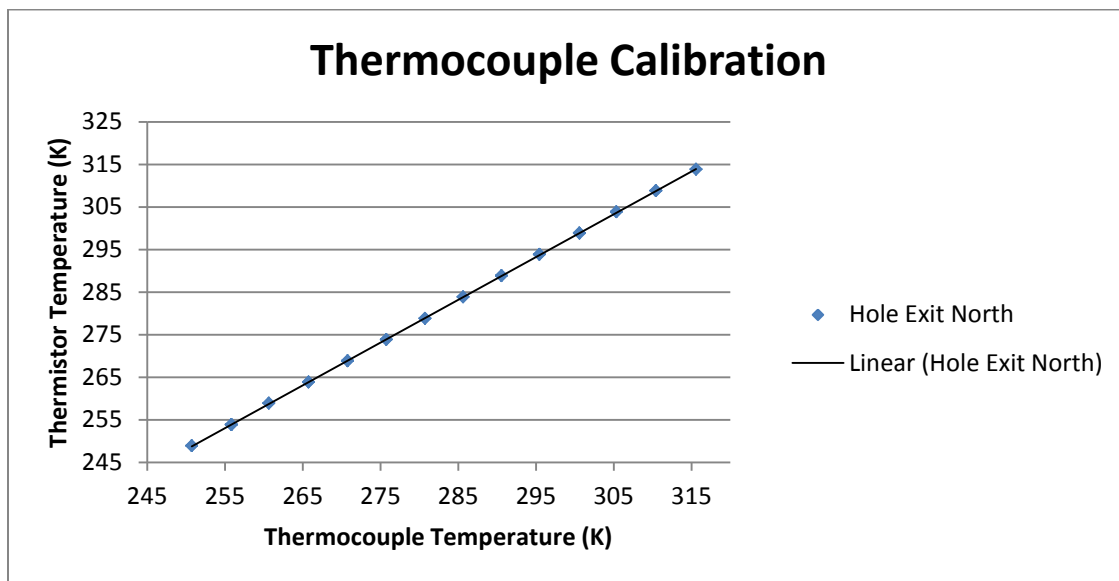


Figure 2.9: Typical thermocouple calibration curve



Figure 2.10: Constant temperature glycol bath used to calibrate thermocouples

2.2.4 Pressure Measurement

Pressure was measured using pressure transducers of various ranges, depending on the particular application. Mainstream velocity was measured using a 0.0 – 0.5 inAq transducer linked to a Pitot-static probe. The pressure differential used in calculating the mass flow rate through the fore coolant passage was measured using a 0.0 – 2.0 inAq pressure transducer; the aft passage was measured using a 0.0 – 1.0 inAq transducer. The static pressure at the fore orifice plate location was measured with respect to atmosphere in order to obtain as accurate a measurement of fluid density as possible; the transducer used for this measurement had a range of 0.0 – 27.0 inAq. The static pressure at the aft orifice plate was assumed to be equal to the static pressure at the fore orifice plate throughout the duration of these experiments.

Every pressure transducer used in these experiments was calibrated against a micromanometer. A curve fit was applied to the calibration data to allow LabVIEW to interpret voltage output from the transducers as pressures (Figure 2.11). The zero location of the pressure transducer calibration was checked and altered if necessary prior

to running each experiment in order to ensure that voltage drift would not cause a bias in any measurements being taken.

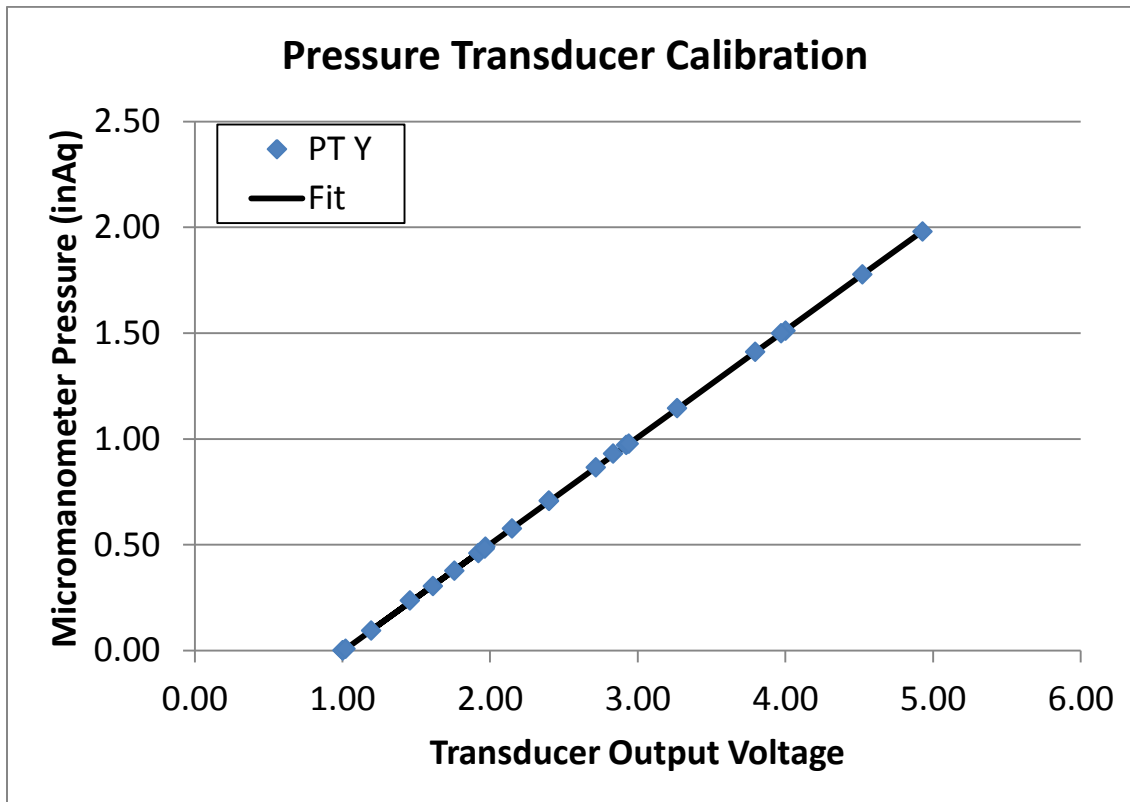


Figure 2.11: Typical pressure transducer calibration

2.2.5 Experimental Procedure for Overall Effectiveness Study

The first step in the experimental procedure was to ensure that all equipment was nominal. This primarily involved adjusting the calibration intercept of any pressure transducers whose zero readings were off by more than 0.0001 inAq and ensuring that no thermocouple ports were failing to read a reasonable temperature (roughly room temperature). All infrared cameras were turned on to allow the detector arrays to warm up. After any necessary adjustments were made, the wind tunnel fan was turned on.

The operating conditions of the vane required a Reynolds number, defined by the axial chord length and approach flow mainstream velocity, of $Re_c = 190,000$. This corresponded to a mainstream velocity of 5.8 m/s in the approach flow within the test section at a temperature of $305\text{ K} \pm 0.5\text{ K}$. The mainstream velocity was maintained $\pm 0.05\text{ m/s}$ throughout the duration of the with-mainstream portions of the experiment. A mainstream velocity of 0 m/s was maintained for the no-mainstream case by shutting off the wind tunnel fan for this portion of the experiment.

Prior to taking IR data, liquid nitrogen was run through the heat exchanger to bring it down to an appropriate temperature and to reach the target density ratio of 1.2 for the test. This process involved pumping coolant through the vane model, allowing it to gradually cool down to a thermal steady state condition. Throughout this cool-down process, IR camera and LabVIEW thermocouple data were taken intermittently to provide comparative data points for an in-situ IR camera calibration that would be applied during post-processing. Since this cool-down was necessarily a transient process, IR camera images and LabVIEW data points were taken as closely spaced in time to one another as possible to ensure that minimal surface temperature change would occur between taking data using each system.

All effectiveness measurements were taken while the test vane was at thermal steady state. This was defined during the test as being an extended period of constant blowing ratio, density ratio, mainstream velocity, and mainstream temperature. Multiple images were taken for each blowing ratio to ensure that steady state had in fact been reached. Post processing was done to ensure that steady state had been reached by determining if all laterally averaged overall effectiveness curves for a particular blowing

ratio “collapse” onto one another over a span of several minutes (i.e. the surface temperature of the article stays constant over time with respect to the coolant and mainstream temperatures) (Figure 2.12).

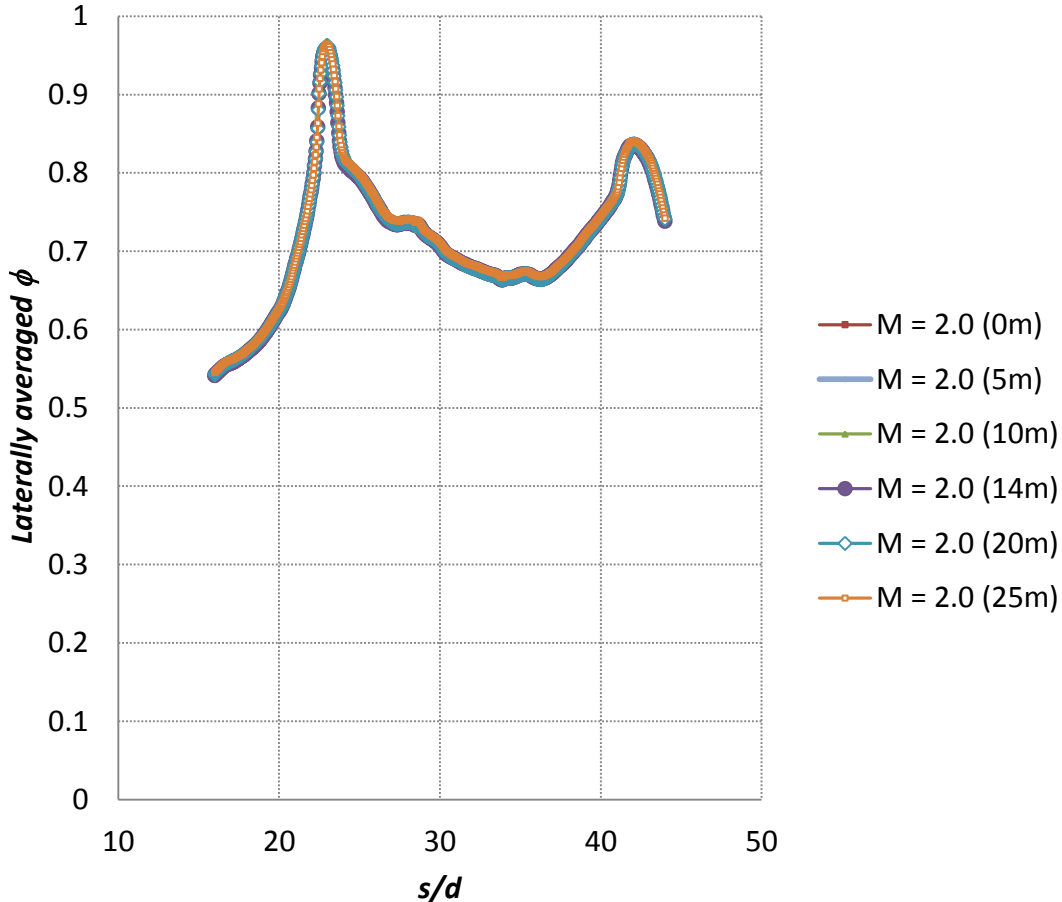


Figure 2.12: Laterally averaged effectiveness curve collapse at thermal steady state, variation over a 25-minute interval shown

Rather than tracking the blowing ratio for each row of holes during the experiment, a showerhead-averaged blowing ratio was used as the test metric. A secondary definition for the showerhead blowing ratio is as follows:

$$M^* = \frac{\rho V_c}{\rho V_{\infty, approach}} \quad 2.1$$

Note that the $V_{\infty, approach}$ used in this definition is not a local velocity, but the velocity measurement of the approach flow. This alternate definition is chosen because the showerhead is located nominally in the stagnation region, where local velocities reach zero, driving the value of the ordinary blowing ratio at that location to infinity. This M^* formulation allows a finite blowing ratio to be defined in the showerhead region. This definition of M^* is constant for a particular row of holes; the average blowing ratio value across the whole showerhead is used as a test parameter in this experiment.

The blowing ratio test matrix is shown in the following table (Table 2.2):

Table 2.2: Blowing ratio matrix for overall effectiveness tests

Point Number	Blowing Ratio (M^*)	Density Ratio (DR)	Mainstream Condition
1	2.0	1.2	With
2	1.0	1.2	With
3	1.0	1.2	Without
4	2.0	1.2	Without
5 (1 Repeat)	2.0	1.2	With
6 (4 Repeat)	1.0	1.2	Without

Since blowing ratios for the no-mainstream case are infinity for any amount of positive mass flux from the film cooling holes, a new definition was required for the no-mainstream blowing ratios. The mass flow rate for a given blowing ratio at the nominal condition was therefore defined as the mass flux required to produce the same pseudo-

blowing ratio for the no-mainstream condition. That is, the mass flow rates for a given nominal blowing ratio and the same given pseudo-blowing ratio were equal.

The no-mainstream condition was obtained by intermittently shutting off the wind tunnel and allowing the vane model to come to thermal steady state. This transition was done at least two times in any given test, as per the test matrix outlined in Table 2.2. To return the tunnel to the with-mainstream case, the tunnel was simply turned on once more, the velocity was adjusted to the appropriate value, and the test article was allowed to reach thermal steady state prior to taking IR data once more.

Internal validity of measurements was ascertained by performing in-test repeat points. The mainstream-on and mainstream-off $M^* = 2.0$ cases were chosen as the repeat points. Pressure transducers that were used to measure pressure drop across orifice plates were checked for drift and re-zeroed if necessary to remove any bias in mass flow calculations. This in turn helped ensure that the blowing ratio did not differ between the initial points and repeat points.

After all effectiveness measurements had been taken, the flow of nitrogen into the coolant loop was shut off, and the system was allowed to warm up. The centrifugal blower was still used to push air into the heat exchanger and out through the vane model throughout this process, allowing the vane model to gradually increase in temperature. As the vane model surface temperature increased, additional IR and LabVIEW data points were taken to provide repeat data for the in-situ camera calibration. After the vane had reached room temperature, all systems were shut off and the experiment was concluded.

2.2.6 Overall Effectiveness Data Processing

An image processing scheme was developed to be able to map the curvilinear geometry of the turbine vane model to the flat two-dimensional array of temperatures captured in an IR image. In order to do this, location lines were drawn at constant spanwise values along the vane (Figure 2.13), with demarcations made every centimeter, starting at the stagnation line location. These lines were drawn with silver paint pen, which had a different emissivity from the black paint used on the rest of the vane model. This difference in emissivity and corresponding apparent surface temperature allowed the lines to be resolved in the IR images.

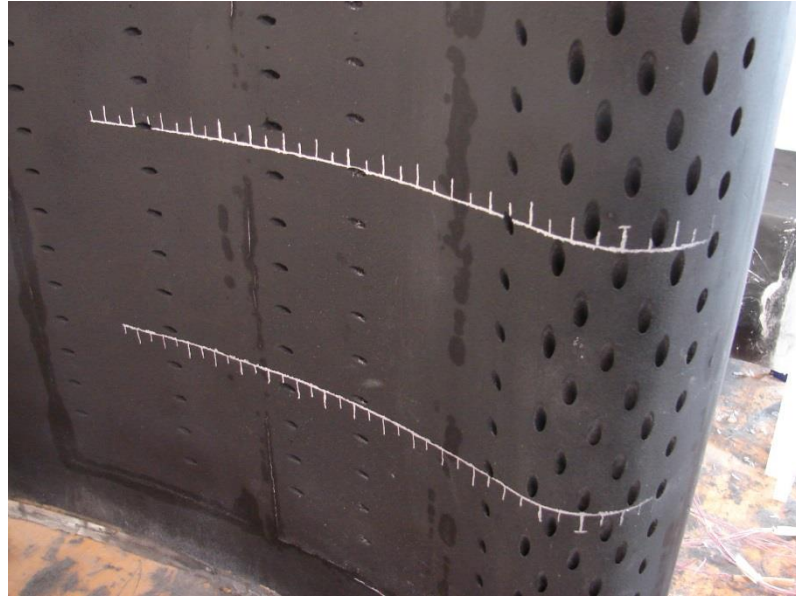


Figure 2.13: Vane model showerhead and pressure side with locating lines

The spanwise locations of these locating lines were known, and the tick marks made at every centimeter could be converted into x/C locations by dividing the distances between the tick and the stagnation location by the blade chord length. Therefore, a correlation relating the distance between tick marks to the number of pixels between each

individual tick mark along each line could be made. Similarly, a correlation relating the known spanwise distance to the number of pixels between the locating lines could likewise be made. Having this information relating pixel location to known physical distances along the vane surface allowed for an algorithm to be written that would flatten the raw camera data into a rectangular shape (Figure 2.14). This translation of the image data to physical x-y coordinates allowed for quantities to be averaged in the spanwise direction—a useful way of compactly expressing the effectiveness of a vane cooling configuration. Similarly, this flattened image provided a better visual reference for contour plots of the overall effectiveness across the surface of the vane.

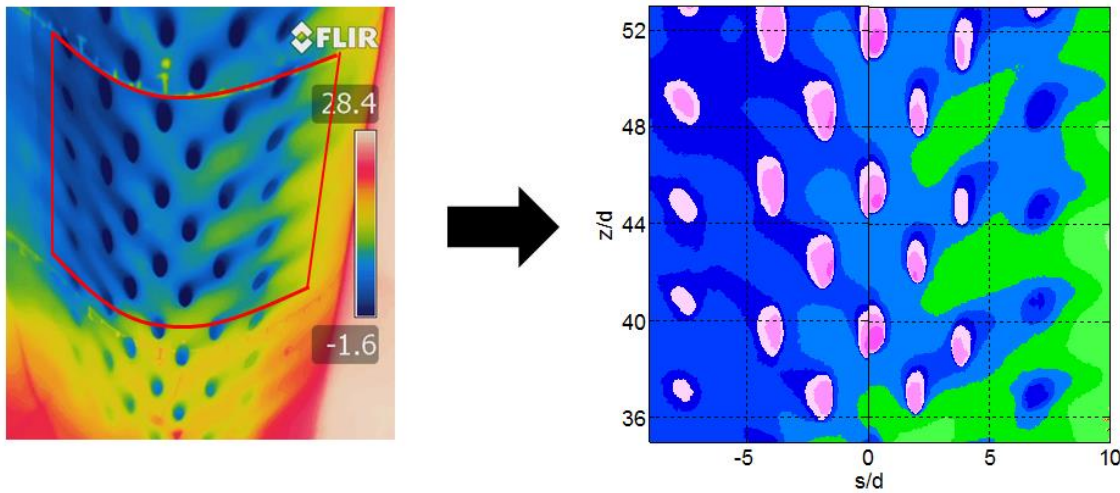


Figure 2.14: Example of the flattening of raw data into a contour plot

After the temperature data was flattened, the temperature values were converted to overall effectiveness values in MATLAB by using the coolant and mainstream temperatures recorded at the time that the IR image was taken. Lateral averaging of overall effectiveness data was done by simply averaging all effectiveness values over an integer number of hole pitches at a particular x/C value.

2.3 Measurements for Approach Flow Turbulence Testing

2.3.1 Approach Flow Test Setup

A series of experiments were performed in order to quantify the effect that altering the inflow angle into a passive turbulence generator would have on the turbulence quantities at a measurement plane downstream of the generator. The only test parameter varied in this experiment was the angle of the grid; rod diameter remained constant throughout these experiments (Table 2.3). Grid solidity was altered for one test as a reference case, but solidity was not used as a fully varied parameter over all test cases. The effect of altering the Reynolds number as defined by the approach flow velocity and the rod diameter was not investigated, noting that turbulence intensity is not expected to vary significantly over the range of velocities that would be accessible to a low-speed wind tunnel (Baines & Peterson, 1951).

Table 2.3: Turbulence grid angle test matrix

Test Number	Approach Flow Angle (°)	Approach Velocity (m/s)	Nominal Rod Diameter (in)	Solidity
1	0	9.5	0.375	0.25
2	0	9.5	0.375	0.50
3	25	9.5	0.375	0.25
4	35	9.5	0.375	0.25
5	45	9.5	0.375	0.25

The rationale for choosing these particular values as the test parameters is explained in detail in chapter 4.

The test setup for each angle of the turbulence grid was unique. However, each setup had a number of aspects in common. For all tests, the turbulence grid was set up in

a section of the wind tunnel that had a constant cross-sectional area (Figure 2.15). The turbulence generator was placed within the tunnel so that the measurement plane, 14" downstream of the grid in each case, was far upstream of any vane model (greater than 0.43 C) in the tunnel. This was done so that the presence of the vane leading edge would not impact the mean velocity distribution or turbulent length scales at the location of measurement (Polanka, 1999), (Radomsky & Thole, 1999). All tests were set up so that the grid extended across the entire width of the tunnel—this was done to mitigate the risk of having a mean velocity gradient across the tunnel, which would impact the values calculated for the turbulence intensity. In all cases, the turbulence rods spanned at least 95% of the height of the tunnel; the small gap between the ends of some of the turbulence rods and the tunnel ceiling was not expected to cause any issues along the measurement line, which was located at the tunnel midspan. The turbulence rods were made of extruded 6061 aluminum. A small gap was left intentionally in order to prevent the wind tunnel floor and ceiling from compressing any rod and causing it to begin to buckle, decreasing its dimensionality and potentially causing local changes in grid solidity (Figure 2.16). A local change in grid solidity could be expected to impact the local mean velocity and turbulence intensity values, as flow would travel preferentially through any less-blocked section of the wind tunnel. This effect was seen for an early iteration of the turbulence rods, which were made of wood dowel and friction-fit into the tunnel, causing some rods to buckle.

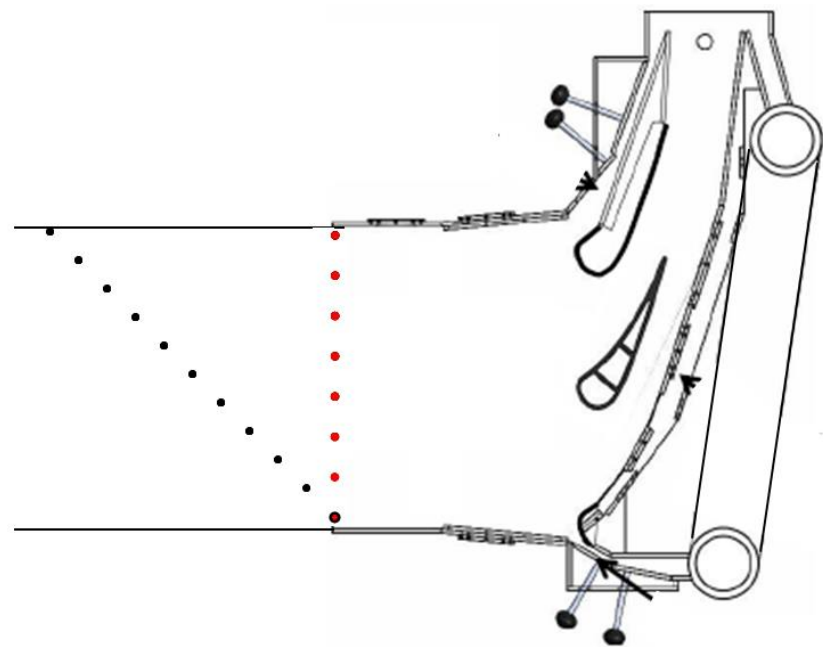


Figure 2.15: Turbulence grid setup schematic; 45d in black, and 0d in red

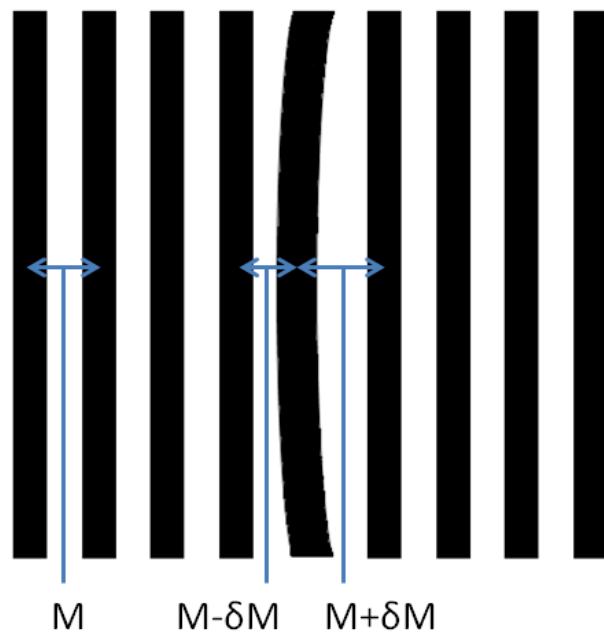


Figure 2.16: Schematic of local change in solidity due to the buckling of a single rod in the turbulence grid

The angle at which each grid was set up was measured using an adjustable angle square. The expected accuracy of the measurement of this angle was $\pm 0.5^\circ$. After setting up the grid, the linear stages used to traverse the probe across the width of the tunnel were set up so that their direction of actuation was parallel to the turbulence grid. This was likewise accomplished by using the adjustable angle square, with outer tunnel test section walls comprising the angle measurement datum.

A method was employed to enable the repeatable locational placement of a probe, either hot wire or Pitot-static, within the tunnel. After a probe was given its initial placement within the tunnel, a pair of marks was made on the acrylic wind tunnel walls so that the locations of the two marks and the probe head were collinear (Figure 2.17). If the three marks appeared were aligned when viewed from outside of the tunnel, then the probe head was located somewhere along the line “connecting” the two marks. A second pair of marks was then made in the same manner at different locations on the wind tunnel walls. If the probe head appeared to be on both of these sets of lines, then the probe location could be assumed to be within a volume equal to the volume of the intersection of the two imaginary lines drawn across the tunnel. This means that if the diameter of the marks made on the tunnel was 2 mm, the probe could be repeatably placed at the same location, ± 1 mm in any direction. This level of spatial placement repeatability was deemed sufficient for the approach flow testing.

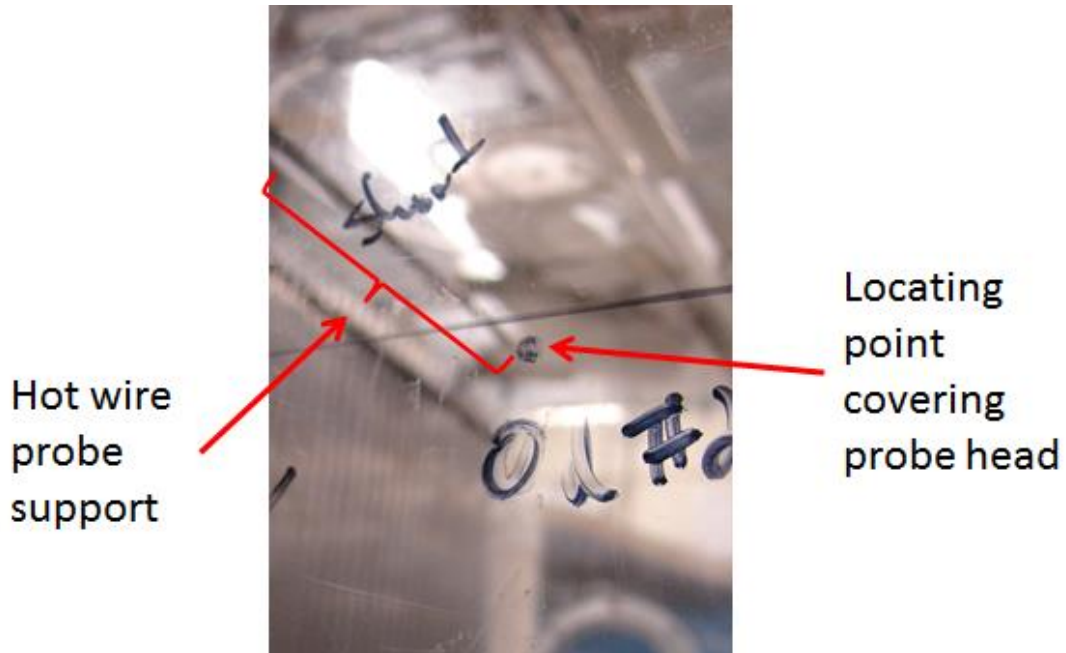


Figure 2.17: Hot wire and Pitot probe location method

The method of probe placement described above was useful in developing a calibration for the hot wire probe for each experiment. This process is explained in detail in section 2.3.5.

2.3.2 Hot Wire Anemometer Measurement of Approach Flow

An A.A. Laboratory Systems AN-1003 hot wire anemometer system (Figure 2.18) was used to provide the feedback circuit for the constant temperature hot wire probe and to output voltages to the data acquisition system. A TSI 1210-10W single-component hot wire probe was used (Figure 2.19); the use of a single-wire probe rather than a multiple-component probe was justified by the expectation that all measurements would be taken far downstream of the plane at which the individual rod wakes merged and the turbulence became isotropic ($x/b \approx 10$). The hot wire diameter was $5 \mu\text{m}$ and a nominal overheat ratio of 1.5 was used.



Figure 2.18: The A.A. Laboratory Systems AN-1003 hot wire anemometer system



Figure 2.19: Example image of a TSI 1210-10W single hot wire probe tip

The 42"-long probe support was made in-house and consisted of a non-magnetic stainless steel tube $\frac{3}{16}$ " in diameter that was friction-fit to a TSI 1150-6 hot wire probe support. The hot wire probe support was connected to the anemometer system via a BNC cable. The hot wire and probe support were physically set up onto a set of linear actuator

stages. The response circuit was tuned after the linear stage setup was completed to ensure that no bias in cable resistance would be incurred due to physically moving the probe support after tuning the anemometer.

2.3.3 Thermocouple Measurement of Approach Flow

An E-type gas thermocouple was used to investigate the temperature uniformity across the width of the wind tunnel in support of the hot wire anemometer experiments. This was done because the voltage readout of the hot wire probe (and therefore the velocity it measured) was a function of both fluid velocity and fluid temperature. Therefore, it was important to ensure that the calibration-changing effect of a temperature gradient inside of the tunnel would not influence data being taken in the approach flow. The minimum acceptable temperature variation was deemed to be ± 0.5 K, and subsequent the completion of this test, the hot wire probe was only traversed in a region that exhibited a sufficiently small temperature gradient.

The thermocouple was calibrated against a thermistor using the same method as discussed in a previous section. It was traversed across roughly one half-width of the wind tunnel using numerically controlled linear stages to ensure that the probe position could be accurately and repeatably determined. The minimum resolution of the linear stage was 0.5 μ m, with a position locating repeatability of 4 μ m, far smaller than the either the minimum traversing distance used (2.54 mm) or the repeatability of probe setup within the tunnel (± 1 mm in any direction).

2.3.4 Pressure Measurement

As with the overall effectiveness testing that was performed, pressure transducers were used to measure differential pressures during all approach flow tests. A Pitot-static probe connected to a 0.5 inAq pressure transducer was used to measure the mainstream velocity, and another Pitot-static probe connected to a different 0.5 inAq pressure transducer was used to measure the mean velocity at the spatial location at which the hot wire anemometer would be calibrated. These pressure transducers were calibrated using the same method as those used in the overall effectiveness testing, described in section 2.2.4.

2.3.5 Experimental Procedure for Approach Flow Turbulence Testing

The hot wire response circuit was tuned by first connecting a shorting probe to the probe support and adjusting a trim potentiometer until the electrical resistance of the probe, probe support, and wire were balanced out. This shorting probe was then replaced by the actual sensing probe head, and the Wheatstone bridge was balanced by adjusting a tunable resistor on the bridge. Then, the overheat ratio was set by further increasing this resistance until it was equal to the original resistance multiplied by a pre-specified overheat ratio. A nominal overheat ratio of 1.5 was used in all of these experiments—this corresponded to a nominally 120 K increase in wire temperature. The overheat ratio was applied while the surrounding air was at room temperature, typically 296 K within the laboratory. After the bridge was balanced, the control system damping was adjusted using a damping potentiometer. This was done to obtain a system response curve similar to the one shown in (Figure 2.20) when measured using an oscilloscope.

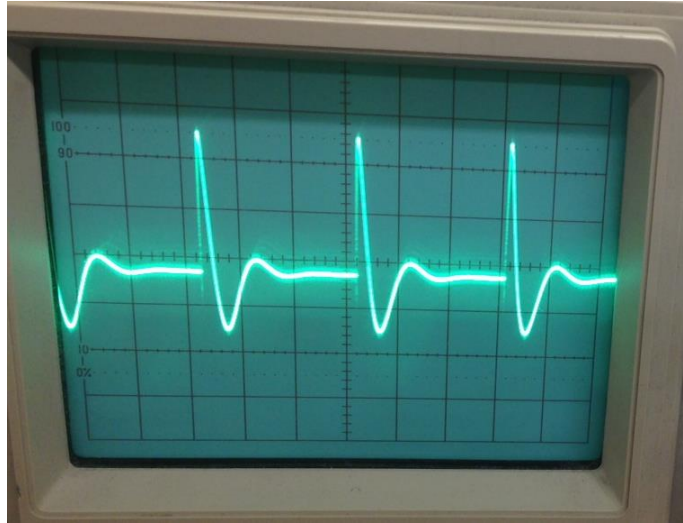


Figure 2.20: Sample hot wire anemometer system response curve

The hot wire calibration was done in two steps. The first step was to determine the local velocity at the position the hot wire was to be calibrated, relative to the standard mainstream velocity. To determine this, a “velocity multiplier” was established using a Pitot-static probe placed at the location used for hot wire calibration. This mainstream velocity reference came from the permanently installed Pitot-static probe that is used to measure mainstream velocity for all tests conducted within this facility. A different velocity multiplier test was done for each of the different test setups, since the velocity multiplier depends on the incoming flow field as well as local tunnel geometry; the multiplier obtained was always nominally close to unity. An example of the results of a velocity multiplier test can be seen in (Figure 2.21). All velocity multiplier tests were conducted at a mainstream temperature of $310\text{ K} \pm 0.2\text{ K}$, the same temperature range in which the hot wire calibrations and tests were themselves performed.

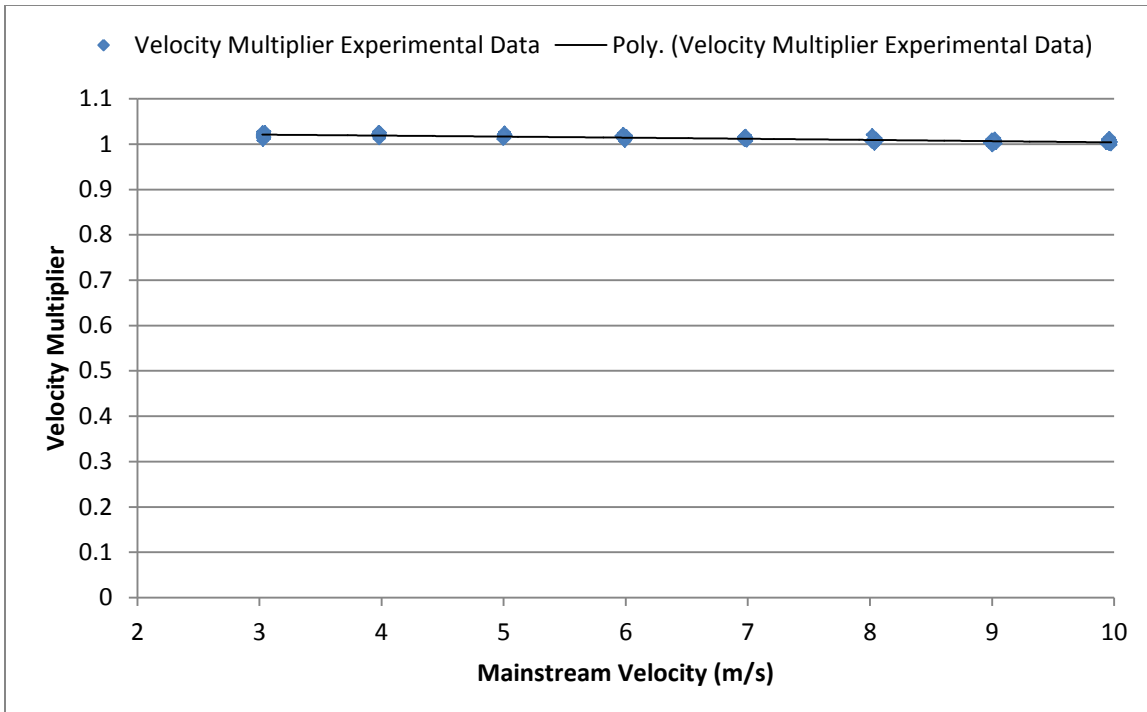


Figure 2.21: Example hot wire test velocity multiplier curve fit

The second step of the hot wire calibration was done in-situ to the turbulence quantity experiments. The hot wire calibration takes the following form, where u is the velocity, and V is the anemometer output voltage:

$$u = AV^4 + BV^2 + C \quad (2.2)$$

Two calibrations were performed for every experiment: one prior to taking turbulence data and one after all turbulence data had been collected; this was done to ensure that the hot wire calibration did not drift over the course of the experiment. The calibration consisted of correlating voltages output by the anemometer system to the local velocity at the hot wire probe location, which was obtained using the velocity multiplier method as described above. A curve fit to this correlation was determined in Microsoft

Excel then implemented directly into the LabVIEW VI for use on subsequent measurements.

It is necessary to mention that the calibration obtained was extrapolated during the experiment, since instantaneous velocities downstream of the turbulence generator could exceed the maximum mean velocity that the wind tunnel was capable of producing. Extrapolation over a small range (roughly 1 m/s greater than the maximum mean velocity) is justified by the fact that the calibration is not an arbitrary polynomial; rather, the form of the calibration curve fit is an analytical expression of the rate that heat is transferred away from a hot cylinder in cross-flow. These formulations for hot wire calibrations were developed by King (1914) in his investigation of convective heat transfer around a thin cylinder, and refined later by Comte-Bellot specifically for hot wire (1976).

Data was taken at a rate of 10 kHz for a duration of 5 seconds for each individual data point; multiple points were taken at each location to establish the precision error envelope. The probe was traversed across the width of the tunnel along a line parallel to the turbulence grid in increments of 0.1" to 1", depending on the spatial resolution desired for the data. After the extent of the linear stage traversing distance had been crossed, repeat points were taken every 2" to provide references that could be used to evaluate in-test repeatability.

The mean velocity profile was established by taking the average of the mean velocities measured at each location over the duration of a test. Turbulence intensity was calculated by taking the standard deviation of the instantaneous velocities being

measured, dividing this quantity by the mean velocity at that location, and multiplying by 100%:

$$Tu = \frac{u_{rms}}{\bar{U}} * 100\% \quad (2.3)$$

Integral time scales were calculated by integrating the autocorrelation of the instantaneous velocities taken at a particular data point. Given that the data was discrete rather than a continuous function of time, the discrete formulation of the autocorrelation function was used:

$$R_{xx} = \sum_n \frac{(u_n - \bar{u})(\bar{u}_{n-j} - \bar{u})}{u_{rms}^2} \quad (2.4)$$

In the above formulation, R_{xx} is the autocorrelation value for a given point; u_n is the value of the n^{th} instantaneous velocity data point in the series; \bar{u} is the average velocity among data points in the series; and \bar{u}_{n-j} is the value of an instantaneous data point j time steps away from n . The integral time scale is obtained by integrating the autocorrelation. The integration of the autocorrelation function is ended at the point where the autocorrelation crosses the axis at $R_{xx} = 0$:

$$T_{int} = \int_0^{\tau_0} R_{xx}(\tau) d\tau \quad (2.5)$$

The integral length scales are obtained by multiplying the time scale by the mean velocity for the same data point:

$$\Lambda_x = T_{int} * \bar{U} \quad (2.6)$$

Here, Λ_x is the integral length scale; T_{int} is the integral time scale; and \bar{U} is the mean velocity across a given data point series.

2.4 Experimental Uncertainty Analysis

Separate experimental uncertainty analyses were performed for the overall effectiveness experiments and the approach flow turbulence experiments.

2.4.1 Uncertainty in Overall Effectiveness Measurement Test Results

2.4.1.1 *Uncertainty in Blowing Ratio*

Quantifying the uncertainty in blowing ratio is important because all of the overall effectiveness data in this document is presented in terms of blowing ratio. It can be a useful parameter for scaling cooling effectiveness, so in differentiating between the effect of two different blowing ratios it is likewise important to know how accurately this value can be measured. In order to quantify the uncertainty in the blowing ratio, it must be expressed in terms of its measurable components. All densities are calculated assuming the fluid is nitrogen as an ideal gas:

$$\rho = \frac{P}{RT} \quad (2.7)$$

The mainstream velocity was measured using a Pitot-static probe, using the following expression:

$$U_\infty = \sqrt{\frac{2P_{dyn}}{\rho_\infty}} \quad (2.8)$$

The coolant velocity was defined by rearranging the expression for flow continuity:

$$U_c = \frac{\dot{m}}{\rho_c A_h} \quad (2.9)$$

In the above equation, the hole area A_h is known from the model geometry, and the coolant mass flow rate \dot{m} is measured using an orifice plate. The mass flow rate for the fore and aft passages were measured independently using separate orifice plates installed in separate coolant feed channels. The expression used to calculate the mass flow is as follows:

$$\dot{m} = \rho_o A_o \frac{C_d}{\sqrt{1 - \beta^4}} \sqrt{\frac{2\Delta P_o}{\rho_o}} \quad (2.10)$$

Where β is the diameter ratio of the orifice plate to the coolant pipe inner diameter:

$$\beta = \frac{d_o}{d_p} \quad (2.11)$$

By combining the above equations, the blowing ratio can be found in terms of its measurable components:

$$M = \frac{\sqrt{T_\infty}}{\sqrt{T_o}} \frac{\sqrt{P_o}}{\sqrt{P_\infty}} \frac{\sqrt{\Delta P_o}}{\sqrt{P_{dyn}}} \frac{d_o^2}{N_{SS}d_{SS}^2 + N_{PS}d_{PS}^2} \frac{C_d}{\sqrt{1 - \frac{d_o^4}{d_p^4}}} \quad (2.12)$$

Where the total film cooling hole area is comprised of the area of all pressure side holes and all suction side holes, which have different diameters (as outlined in Table 2.1).

The uncertainty in blowing ratio was calculated using the sequential perturbation method of Moffat. A sample calculation of the uncertainty in blowing ratio is provided below, with the measured parameters listed in order of decreasing contribution to the overall uncertainty:

Table 2.4: Sample blowing ratio uncertainty calculation

Measured Parameter	Nominal Value	Measurement Uncertainty	Elemental Uncertainty
Coolant Pipe Diameter, d_p (mm)	62.7	0.879	0.00546
Coolant Hole Diameter SS, d_{ss} (mm)	6.35	0.127	0.00529
Mainstream Dynamic Pressure, P_{dyn} (Pa)	19.4	0.5	0.00090
Inlet Orifice Discharge Coefficient, C_d	0.64	0.008	0.00088
Coolant Hole Diameter PS, d_{ps} (mm)	4.78	0.127	0.00075
Pressure Drop Across Inlet Orifice, ΔP_o (Pa)	197.1	1.3	0.00006
Orifice Plate Diameter, d_o (mm)	53.9	0.083	0.00005
Mainstream Pressure, P_∞ (Pa abs)	101400	500	0.00003
Inlet Orifice Static Pressure, P_o (Pa abs)	105877	500	0.00003
Inlet Orifice Temperature, T_o (K)	248	1	0.00002
Mainstream Temperature, T_∞ (K)	305	0.5	0.00000
Calculated M	2.37		
Total M Uncertainty, δM	0.116		
Percent Uncertainty, $\delta M/M$	5.3%		

In the above calculation, the measurement uncertainty of the coolant pipe diameter is based on caliper measurements of the internal diameter of coolant piping used in the coolant loop, plus the expected change in diameter due to thermal contraction (PipeBid). The coolant hole diameter uncertainty is based on the estimated manufacturing tolerance of the holes. Differential pressure measurement uncertainties

are based on the precision uncertainties of the pressure transducers used to measure these values, plus a bias from pressure transducer drift seen over the course of an experiment. Temperature measurement uncertainties are likewise based on the bias uncertainties for the thermocouples made to make these measurements. The orifice plate discharge coefficient uncertainty had a bias uncertainty that was determined by another member of the TTCRL (Anderson, 2013) during the orifice plate calibration process. The uncertainty in the orifice plate diameter is based on the expected thermal contraction of the device during operation (MatWeb, 2013). Lastly, the uncertainty in the absolute pressure measurements is based on typical values for the drift in atmospheric pressure over the course of the experiment.

This method of uncertainty analysis was undertaken for both of the blowing ratios that were tested. The showerhead blowing ratio is based on mass flow split calculations undertaken by Albert. The uncertainties are presented in the following table:

Table 2.5: Summary of uncertainty in nominal and showerhead blowing ratios

Nominal Blowing Ratio, M	Showerhead Blowing Ratio, M*	Uncertainty in M, δM	Uncertainty in M*, δM^*	Uncertainty in M*, $\delta M^*/M^*$
2.37	2.04	0.112	0.106	5.2%
1.53	1.00	0.074	0.053	5.3%

Since the concept of blowing ratio is not meaningful when there is no mainstream flow around the turbine vane model, it is also worthwhile presenting the uncertainty in coolant mass flow rate, since this was ultimately the parameter that was matched between the with-mainstream and no-mainstream cases. This analysis was performed using

sequential perturbation. Since there are no additional sources of uncertainty in mass flow rate compared to blowing ratio, no broken-down analysis such as the one presented in Table 2.4 is presented in this document. However, the final results in mass flow rate uncertainty are as follows:

Table 2.6: Summary of uncertainty in mass flow rate

Showerhead Blowing Ratio, M^*	Mass Flow Rate, \dot{m} (g/s)	Uncertainty in Mass Flow, $\delta\dot{m}$ (g/s)	Uncertainty, $\delta\dot{m} / \dot{m}$
1	34.02	0.50	1.5%
2.04	52.73	0.77	1.5%

2.4.1.2 Uncertainty in Overall Effectiveness

The uncertainty in overall effectiveness was determined using the Kline-McClintock method. The following equation is used to express the uncertainty in ϕ :

$$\delta\phi = \sqrt{\left(\delta T_\infty \frac{\partial\phi}{\partial T_\infty}\right)^2 + \left(\delta T_c \frac{\partial\phi}{\partial T_c}\right)^2 + \left(\delta T_w \frac{\partial\phi}{\partial T_w}\right)^2 + \left(\delta M \frac{\partial\phi}{\partial M}\right)^2} \quad (2.13)$$

The sensitivity of overall effectiveness to the blowing ratio, $\frac{\partial\phi}{\partial M}$, was determined by comparing the overall effectiveness at different blowing ratios at the locations on the vane that were most sensitive to a change in blowing ratio. The other sensitivities, $\frac{\partial\phi}{\partial T_\infty}$, $\frac{\partial\phi}{\partial T_c}$, and $\frac{\partial\phi}{\partial T_w}$, can be found analytically by taking partial derivatives of the equation that defines overall effectiveness.

The largest contributor to the uncertainty in overall effectiveness was from the uncertainty in the wall temperature, which was measured using an IR camera. Based on

the findings of McClintic (2013) regarding the change of effectiveness data from test to test based on different in-test camera calibrations, the bias uncertainty for the P20 camera was $\delta\Phi = \pm 0.01$. Since this set of experiments involved no test-to-test repeat measurements using the T-620 camera, data from these tests could not be used to define an expected bias $\delta\Phi$ for this camera. It was therefore assumed that this camera would perform similarly to the P20 camera and likewise yield $\delta\Phi = \pm 0.01$. The estimated bias in the coolant temperature was based on the estimated bias uncertainty in a thermocouple using the NIST standard calibration ($\delta T_c = \pm 1$ K); the estimated bias in the mainstream temperature was based on the estimated bias for an in-house calibrated thermocouple ($\delta T_\infty = \pm 0.5$ K).

The precision uncertainty in this measurement was estimated using the same equation. Here, the precision uncertainty of both the mainstream and coolant temperatures were $\delta T_c = \delta T_\infty = \pm 0.05$ K based on observed fluctuation in thermocouple reading at a known constant temperature. The precision uncertainty in the measurement of the wall temperature was based on the observed scatter in data taken by each of the cameras. For both cameras, this uncertainty was $\delta T_w = \pm 2$ K.

The sensitivity of overall effectiveness to blowing ratio was determined to be $\frac{\partial\phi}{\partial M} = \pm 0.05$ from the data; this is a conservative evaluation of how much the effectiveness is changed with blowing ratio. This particular value is seen in the showerhead region for the mainstream-on case; however, it is worth noting that $\frac{\partial\phi}{\partial M}$ is a spatially varying quantity, and is lower elsewhere on the vane. The uncertainty in blowing ratio used in this calculation, δM , was determined in the previous section.

Based on this analysis, the total uncertainty in overall effectiveness for both cameras is $\delta\phi = \pm 0.041$. The individual contributions from precision and bias uncertainty are ± 0.040 and ± 0.01 , respectively.

The validity of this estimate of uncertainty is supported by in-test repeat measurements, which consistently showed a greater repeatability than the estimated precision-only uncertainty in overall effectiveness. Additionally, test-to-test repeatability was evaluated by comparing overall effectiveness test results taken at the same location on the vane on different days with different cameras. (Unfortunately, in only one instance was the same camera used for the same viewing port on different days, so evaluating the test-to-test repeatability of results taken by a single camera is largely not possible for this data set.) Figure 2.22 shows an example of in-test repeatability, demonstrating very good repeatability:

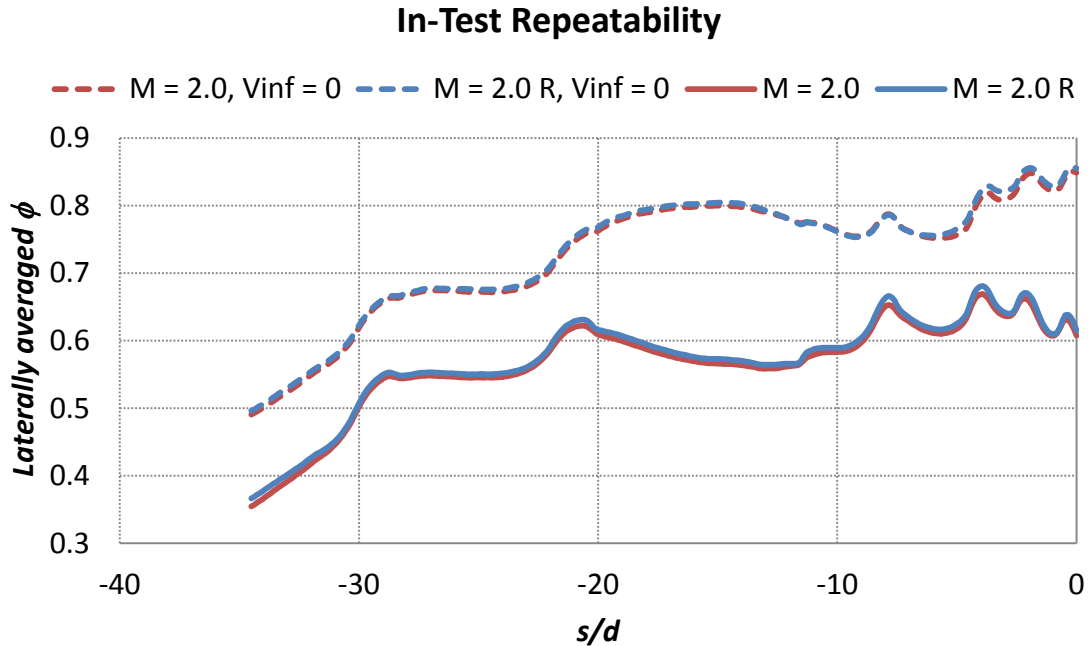


Figure 2.22: Sample in-test repeatability of laterally-averaged overall effectiveness using the P20 camera

2.4.1.3 Uncertainty in Vane Location

The uncertainty in the values for s/d used in the plots of overall effectiveness was determined by comparing the known locations of the film cooling hole rows on the vane model to the s/d value at which these featured appeared in the IR images taken. Since the s/d values used to display the data were obtained from spatial correlations, it was important to ensure that these values matched those on the physical model. The typical uncertainty in the s/d correlation was ± 0.5 hole diameters. Since this uncertainty was small, it is not tremendously important to take into account when examining the plotted data of a single experiment or camera view. However, calculating this uncertainty was worthwhile in that the laterally averaged data of two runs superposed on the same graph may not be perfectly aligned; this uncertainty quantifies how significant any misalignment may be.

2.4.2 Uncertainty in Approach Flow Measurement Test Results

2.4.2.1 Uncertainty in Measured Velocity and Turbulence Intensity

The bias uncertainty in the hot wire calibration can be estimated by evaluating the effect of the uncertainty in the Pitot-static mainstream velocity measurement against which it is calibrated. The uncertainty in the mainstream velocity comes from the uncertainty in the pressure transducer measuring the dynamic pressure, the thermocouple measuring the mainstream temperature, and the local static pressure at the probe location. A visual representation of this uncertainty is shown in Figure 2.23. Due to the increased pressure being reported by the transducer at higher velocities, this source of bias tapers off rapidly at increased velocities. At the testing velocity of 9.5 m/s, this fossilized bias is expected to be $\pm 0.5\%$.

Estimated Hot Wire Calibration Uncertainty

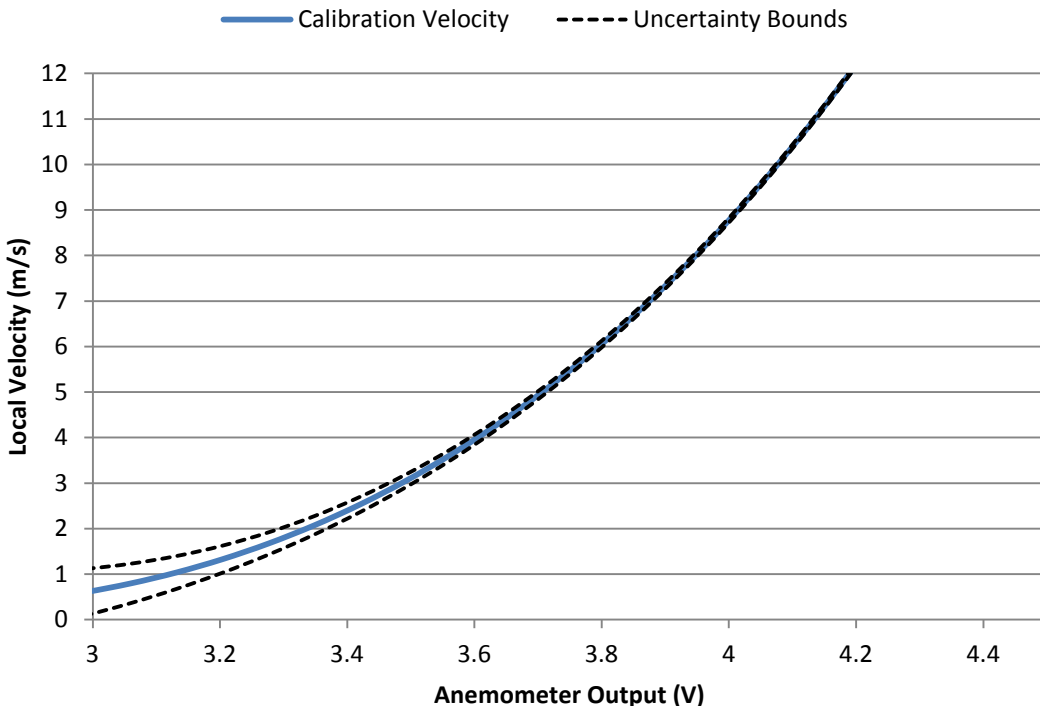


Figure 2.23: Estimated bias uncertainty in hot wire calibration due to mainstream velocity measurement uncertainty

Another potential source of bias comes from the determination of the velocity multiplier. Pitot-static probe misalignment can cause incorrect measurements of dynamic pressure, which would in turn affect the velocity being calculated at the probe location. However, this error in dynamic pressure is expected to be vanishingly small for an angle defect of $< 12^\circ$ (Tavoularis, 2009). Therefore, this was not considered to be a likely cause of significant bias in these experiments.

An additional source of bias error in the mean velocity was established by evaluating the calibration drift of the hot wire over the course of an experiment. As described in section 2.3.5, this was accomplished by performing calibrations both before

and after performing each experiment. Typically, the difference in reported velocity between the two calibrations associated with any one experiment was $< \pm 1.5\%$. Bias error in the RMS velocity was evaluated by comparing the difference in the calibration slope before and after the experiment; this uncertainty was evaluated to be $< \pm 2\%$.

The precision uncertainty envelope for mean and RMS velocity measurements was determined by evaluating the scatter in the data being collected. The sample size was increased until an acceptable level of precision uncertainty was observed. The precision uncertainty of the mean velocity was $\frac{\partial u_\infty}{u_\infty} = \pm 0.9\%$, and the precision uncertainty of the RMS velocity was $\frac{\partial u_{rms}}{u_{rms}} = \pm 2.9\%$ for all measurements taken.

It is important to note that since the power required to hold the hot wire probe at a constant temperature is a function of the rate at which it transfers heat into a flow, the hot wire calibration is dependent not only on the local velocity, but on the local fluid temperature as well. The mainstream temperature, as measured by a pair of thermocouples permanently installed into the tunnel, was kept at 310.0 ± 0.2 K. This level of variation in the mainstream temperature across the course of a test was not expected to significantly alter the hot wire calibration. This hypothesis was confirmed by the results of an experiment testing the sensitivity of the hot wire calibration to a change in mainstream temperature of up to ± 2 K. The change in the calibrations is shown in (Figure 2.24). Given the relatively small effect on calibration that a change of even 1 K had the nominal measurement velocity of 9.5 m/s, it was determined that an envelope of ± 0.2 K was more than sufficient to be able to provide unbiased data. This conclusion is

also supported by the previously mentioned $<1\%$ change in calibration over the course of an experiment at 310 ± 0.2 K.

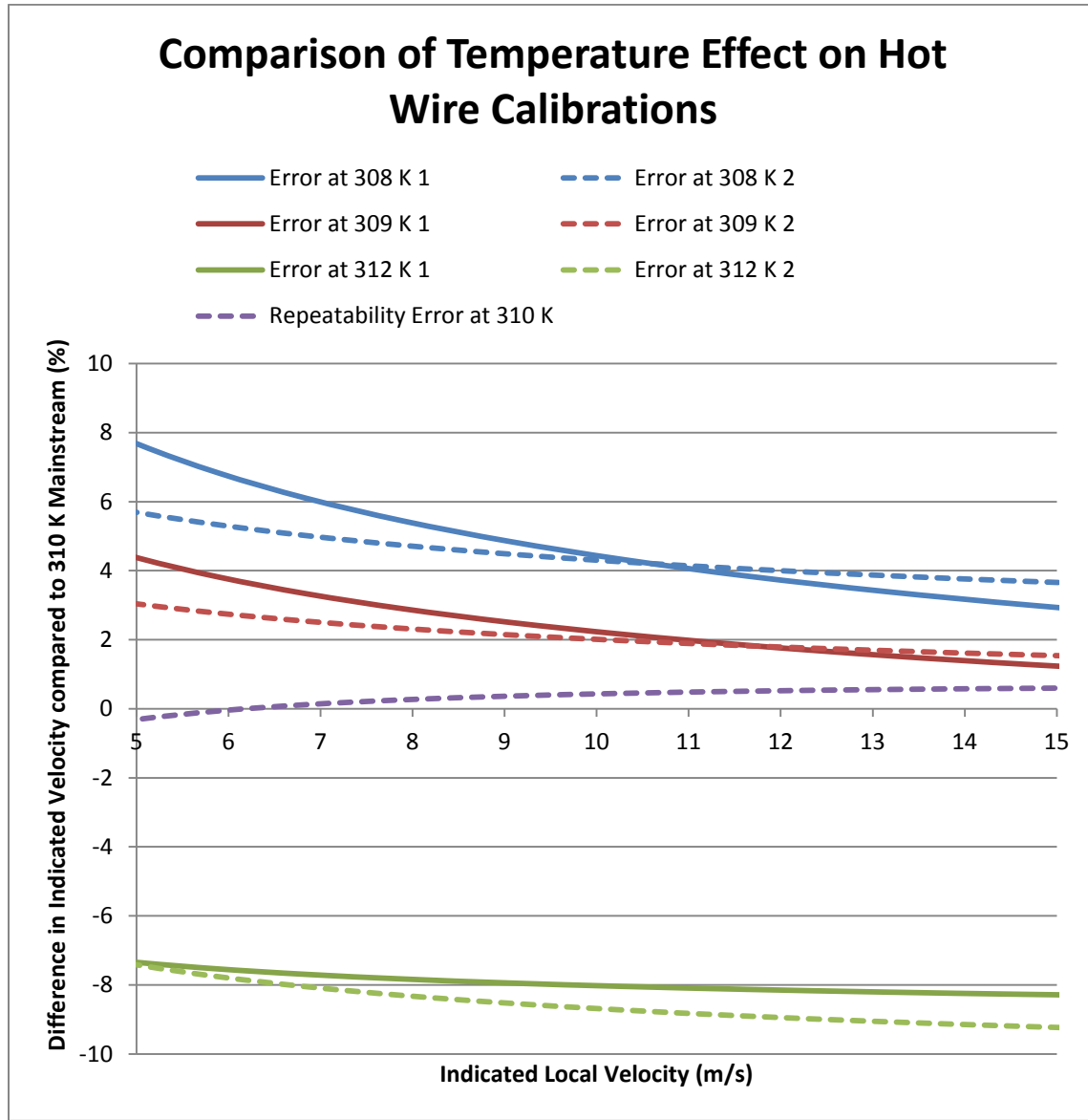


Figure 2.24: Mainstream temperature effect on hot wire calibration

In Figure 2.24, a flat line at 0% error would be indicative of zero difference in hot wire calibration as compared to a calibration performed at 310 ± 0.2 K. Notice that a temperature change causes a difference in calibration that is greater than the repeatability

uncertainty of calibrations performed at nominally 310 K. All mainstream temperatures in this experiment were within ± 0.2 K of the reported values.

Since the mainstream temperature recorded by the permanent thermocouples was a local quantity, it was important to establish how uniform the fluid temperature was across the width of the tunnel. For example, improper fluid mixing, an uneven heat flux distribution across the water heat exchanger, or thermal conduction through the tunnel walls could be expected to have an impact on temperature uniformity. Therefore, a calibrated E-type gas thermocouple was traversed across the width of the tunnel to determine the temperature profile along the tunnel's midspan (Figure 2.25). Near the middle of the tunnel, the temperature profile was reasonably uniform; toward the tunnel wall, a temperature decrease of approximately 0.8 K was apparent. Therefore, measurements in subsequent hot wire tests were confined to areas of the tunnel with the greatest temperature uniformity in order to ensure that spatial temperature deviation would not impact approach flow measurement.

Cross-width Temperature Variation in Wind Tunnel

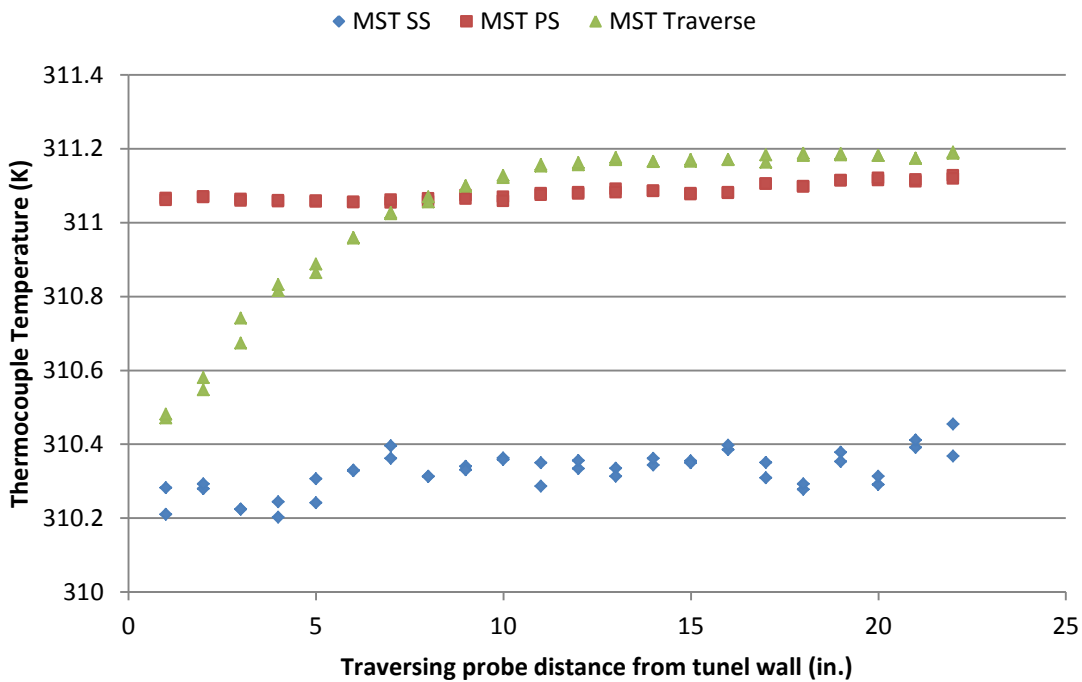


Figure 2.25: Measured variation of mainstream temperature within the wind tunnel at $T_u \approx 6\%$, $U_\infty = 9.5$ m/s

In Figure 2.25, “MST Traverse” refers to the local temperature within the tunnel; “MST SS” and “MST PS” are the tunnel’s permanent stationary thermocouples. Data from the two permanent thermocouples are presented to demonstrate that the variation in the mainstream temperature at fixed points did not vary significantly when compared to the moving thermocouple, indicating that a real temperature gradient is present within the tunnel.

The uncertainty in the turbulence intensity is calculated using the sequential perturbation method. The estimated uncertainty for both of the measured components of the turbulence intensity—the RMS and mean velocity measurements from the hot wire

probe—is addressed above. The uncertainty associated with a typical value of mean velocity $\bar{U} = 9.5$ m/s was used for the purpose of this analysis. Since the degree of bias uncertainty in the RMS velocity due to calibration shift over the course of an experiment varied from experiment to experiment, a value of 2% uncertainty in RMS velocity was chosen for a mean velocity of 9.5 m/s in order to make the most conservative possible estimate. Combined with the anticipated mean velocity bias, this yielded a bias uncertainty of 2.1% of the reported turbulence intensity value. Precision uncertainty was estimated by evaluating the scatter in the calculated turbulence intensity data. The total uncertainty in the turbulence intensity for this set of tests was $\pm 3.3\%$ of the indicated value; using a typical observed value of turbulence intensity in these tests as an example, this would be interpreted as 7 ± 0.23 turbulence intensity.

2.4.2.3 Uncertainty in Integral Length Scales

The uncertainty in the length scale measurement was evaluated by determining its precision envelope. The variability in the calculated length scale from data point to data point was significant, even when multiple measurements were taken at the same location: the observed precision uncertainty in this measurement was ± 1.5 cm for 9 measurements taken of 50,000 data points apiece. Because of this variability, accurately measuring the uniformity of the integral length scale across the width of the tunnel would have been a prohibitively highly data-intensive exercise. Length scale data will instead be presented as a single value for a given turbulence rod setup, with a precision uncertainty that is likewise unique to the setup, and dependent on the number of measurements taken during that particular experiment.

Chapter 3: Evaluation of Vane Cooling Performance with No Mainstream Flow

Overall effectiveness was evaluated for a fully cooled matched Biot number turbine vane model featuring a 5-row showerhead, five pressure side hole rows, and two suction side hole rows. Measurements were taken at a showerhead-averaged $M^* = 2.0$ and 1.0 at a density ratio of $DR = 1.2$. A nominal mainstream velocity of $U_\infty = 5.8$ m/s was used to obtain a matched chord Reynolds number for the vane in the nominal operation case; a mainstream velocity of $U_\infty = 0$ m/s was used to simulate test conditions on a factory floor.

3.1 Purpose of No-Mainstream Overall Effectiveness Study

This study was designed to mimic the way that turbine blade and vane cooling schemes may be tested as an individual blade or vane is taken off of an assembly line and put into a cooling test rig as described in Chapter 1, such that coolant is flowing through it but no mainstream is present. A special case in which the wind tunnel was turned off was used to simulate this condition. In order to mimic the thermal properties of a real turbine vane, a thermally conducting prototype model using a matched Biot number was used. The results are compared to a baseline in which the same vane and coolant geometry are used, but the article is exposed to a mainstream velocity that is scaled to the design Reynolds number of the turbine vane at operating conditions. The intent of this study was to determine the applicability of this no-mainstream method in determining how well a turbine component's cooling configuration will perform at engine conditions.

It is worth noting in advance that the test methodology in which no mainstream flow is applied is clearly flawed: a turbine vane not exposed to a hot mainstream would only exist in a gas turbine that has not yet been turned on. This situation requires no cooling. However, the experiment was completed in hopes of being able to evaluate the value of a factory floor test of a turbine vane cooling scheme by drawing comparisons between results obtained in this non-traditional methodology and results obtained in a typical fully-cooled overall effectiveness test that would be performed in a wind tunnel. For example, perhaps a correlation could be formed relating the results of the two types of tests, or perhaps this test might provide a useful comparison against which hole blockage study effects could be performed, since the blade manufacturing process invariably involves testing for hole manufacturing defects.

This test was performed on a conducting model only. Adiabatic effectiveness was not investigated for the non-traditional cooling test scheme, as the expectation was that in the absence of a mainstream, each coolant jet would have a momentum ratio of $I = \infty$ and immediately separate, leaving no thermal footprint that could be detected using surface temperature measurements. (That is, the adiabatic effectiveness would be zero at all locations.) Using an adiabatic model would also not fit in with the intent of drawing an analogy between this experiment and any data that would be taken in tests performed on real vanes after their manufacture, since all real turbine components are thermally conducting.

3.2 Discussion of Overall Effectiveness Results

3.2.1 Comparison of With-Mainstream Data to Prior Results

In order to validate the measurements taken for this test, the with-mainstream test case was compared to data taken previously in the laboratory. A matched Biot number vane model with the same dimensions and film cooling scheme had been tested previously and served as a point of comparison for the results of this experiment (Figure 3.1). The vanes both used impingement schemes for internal cooling—however, the impingement plates were slightly different in their dimensions. The same showerhead-averaged blowing ratios were tested, making comparison fairly straightforward. The laterally averaged overall effectiveness results for the showerhead-averaged blowing ratios of $M^* = 2.0$ and $M^* = 1.0$ are presented on different axes for the sake of visual clarity, since laterally averaged effectiveness is similar for all four data sets being presented and would appear cluttered if presented without a secondary axis. The arrows indicate which plots belong to which axis.

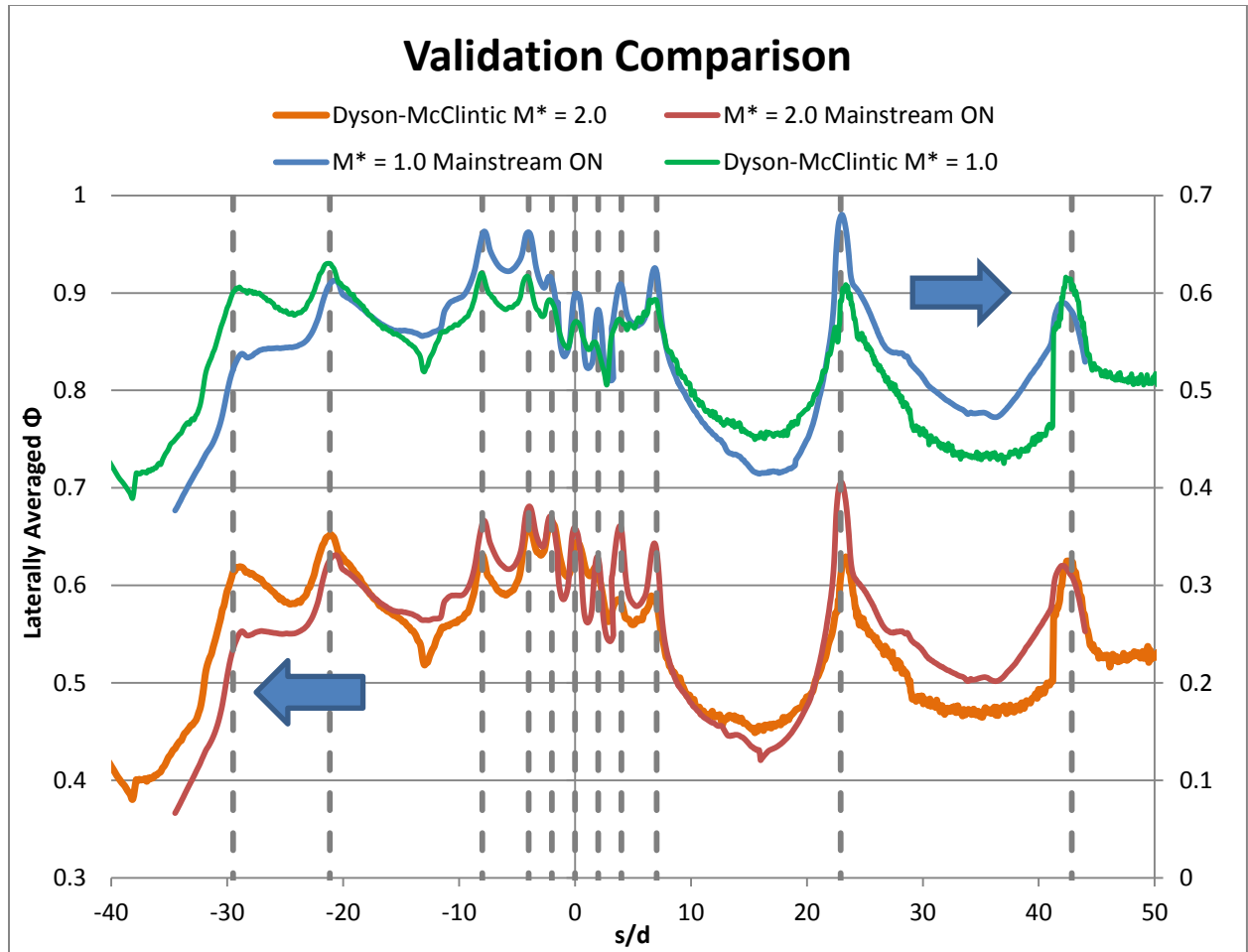


Figure 3.1: Validation of current overall effectiveness experiment's results by comparison to previous laboratory results

For the most part, the effectiveness measurements at each of the blowing ratios match fairly well. The laterally averaged overall effectiveness in the current experiment tends to be higher along the suction side and lower on the pressure side in comparison to prior results. This might be indicative of a slightly different internal coolant flow field inside of the vane due to the different impingement plates being used. Note that the prior experiment shows a hot spot at an s/d of approximately 13—this zone of higher temperature was caused artificially due to the use of a spackle of low thermal conductivity to seal a hatch in that experimental setup. This defect is not present in the

current study; since this difference in results is easily explained, this is not considered a substantial issue. In general, the results appear to be in good agreement with one another, indicating that the results of the current experiment are valid and reproducible.

3.2.2 Comparison of No-Mainstream and With-Mainstream Cases

3.2.2.1 Laterally Averaged Data

Below is a figure showing a comparison between the laterally averaged overall effectiveness experiment results for the with- and without- mainstream cases (Figure 3.2). Note that in this figure, the spikes in the laterally averaged overall effectiveness represent film cooling hole row locations, where effectiveness is locally elevated. The hole locations are marked on this graph using vertical dashed lines; the laterally averaged effectiveness at these locations should not be regarded as representative of the effectiveness between the holes, and the presence of any hot spots at the same streamwise location as a hole row would not be identifiable by examining the laterally averaged data alone.

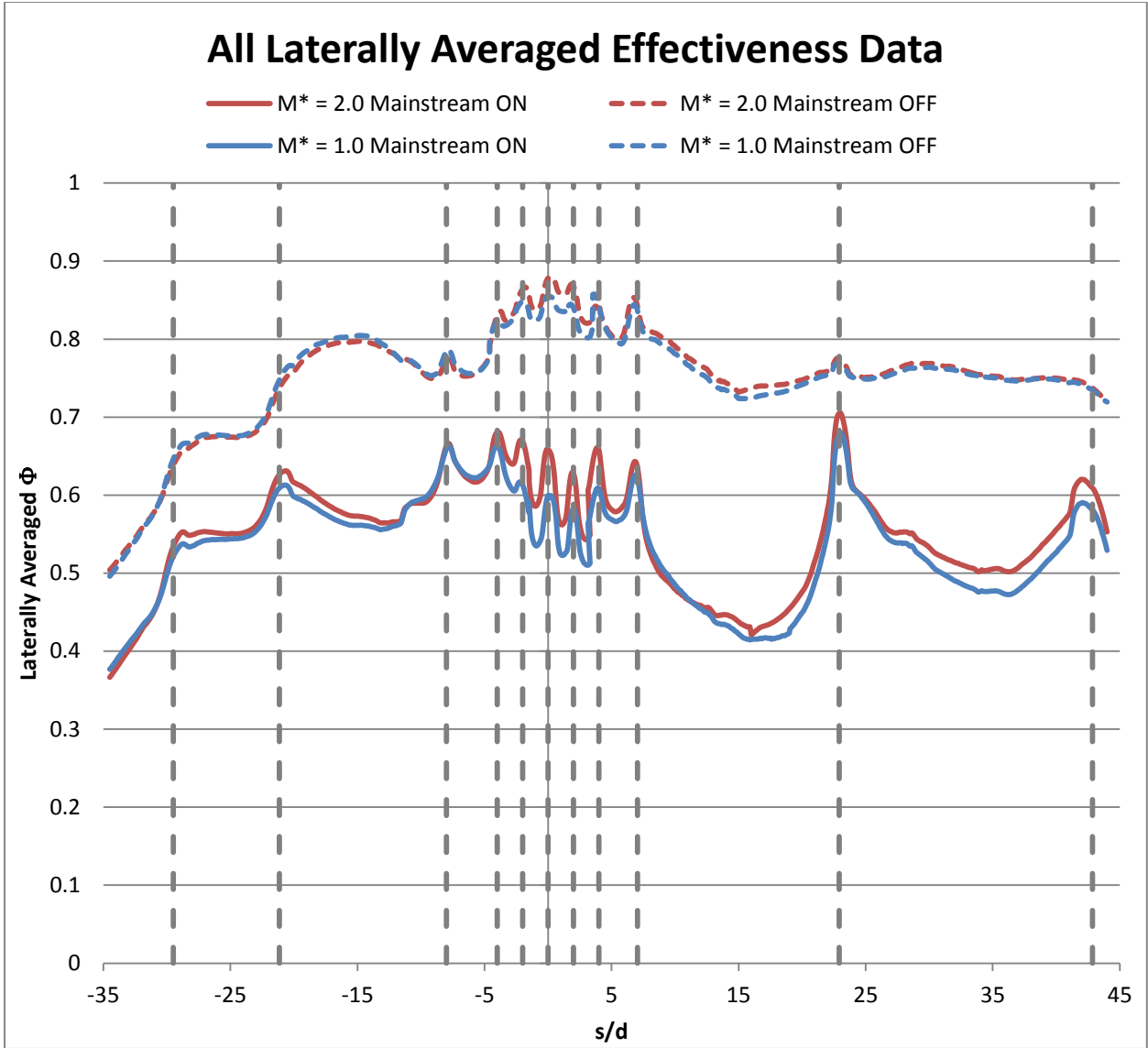


Figure 3.2: Laterally averaged effectiveness data for both with-mainstream and no-mainstream cases

As expected, the removal of the hot mainstream causes a sharp increase in the laterally averaged overall cooling effectiveness of the turbine vane test article (Figure 3.2). This is explained by the reduction in the external heat transfer coefficient upon removal of the mainstream. With the mainstream flow, the test article experiences a range of relatively high external heat transfer coefficients due to the application of forced convection around the body of the vane. In absence of any mainstream flow impinging

upon the blade, the heat transfer is dictated by natural convection, giving a much lower heat transfer coefficient. This, combined with the fact that the internal heat transfer coefficients are the same for both the mainstream on and off cases, means that the mainstream off test case experiences considerably less heat load for a given coolant mass flow rate; this is exhibited by the significant increase in overall effectiveness.

The higher levels of $\bar{\phi}$ for the no-mainstream case were expected, but an important part of this study was to determine whether there was a correlation between $\bar{\phi}$ measured with no mainstream and the correct $\bar{\phi}$ measured with mainstream flow. When comparing the overall effectiveness of the with-mainstream and no-mainstream cases, it is worth noting that there is no obvious single correlation that would relate the cooling effectiveness at different mainstream conditions, as the difference in the effectiveness between those cases vary with x/C . No obvious single value of $\bar{\phi}$ can be added to the with-mainstream results to obtain the no-mainstream results; similarly, there is not one multiplicative constant that will have a similar effect (Figure 3.3). It is presumed that this difference in effectiveness is a function of the laterally averaged external heat transfer coefficient in each case. Evidence for this hypothesis can be seen in that the difference in laterally averaged effectiveness between the mainstream-on and -off cases for a particular blowing ratio vary with position on the vane: the pressure side, which experiences the lowest local velocities and h_o (Figure 3.4), sees an effectiveness differential of $0.13 < \Delta\Phi < 0.25$ away from hole locations, with the lower differentials occurring at low-curvature regions. The suction side, which experiences much higher local velocities and un-augmented heat transfer coefficients h_o , sees an effectiveness differential of $0.20 < \Delta\Phi < 0.31$, with the highest differentials occurring in the regions of highest curvature.

However, it is fairly clear that h_o does not paint a complete picture of the difference in overall effectiveness, since the film jets in the with-mainstream case will augment the heat transfer at the wall. The arrows superposed on the plot indicate which data sets belong to which vertical axis.

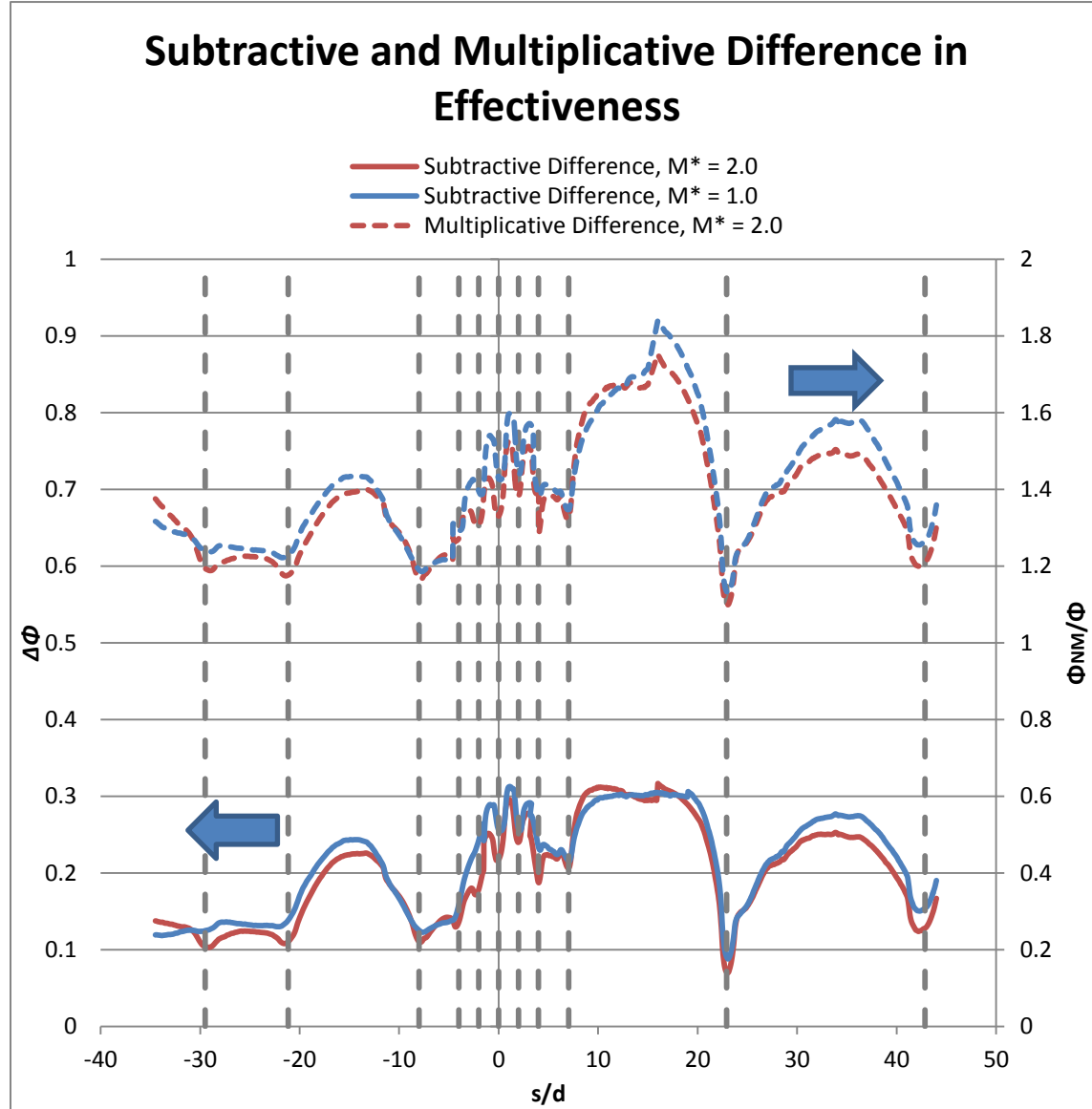


Figure 3.3: Subtractive and multiplicative difference between effectiveness values taken with and without mainstream

Heat Transfer Coefficient for Uncooled C3X Vane

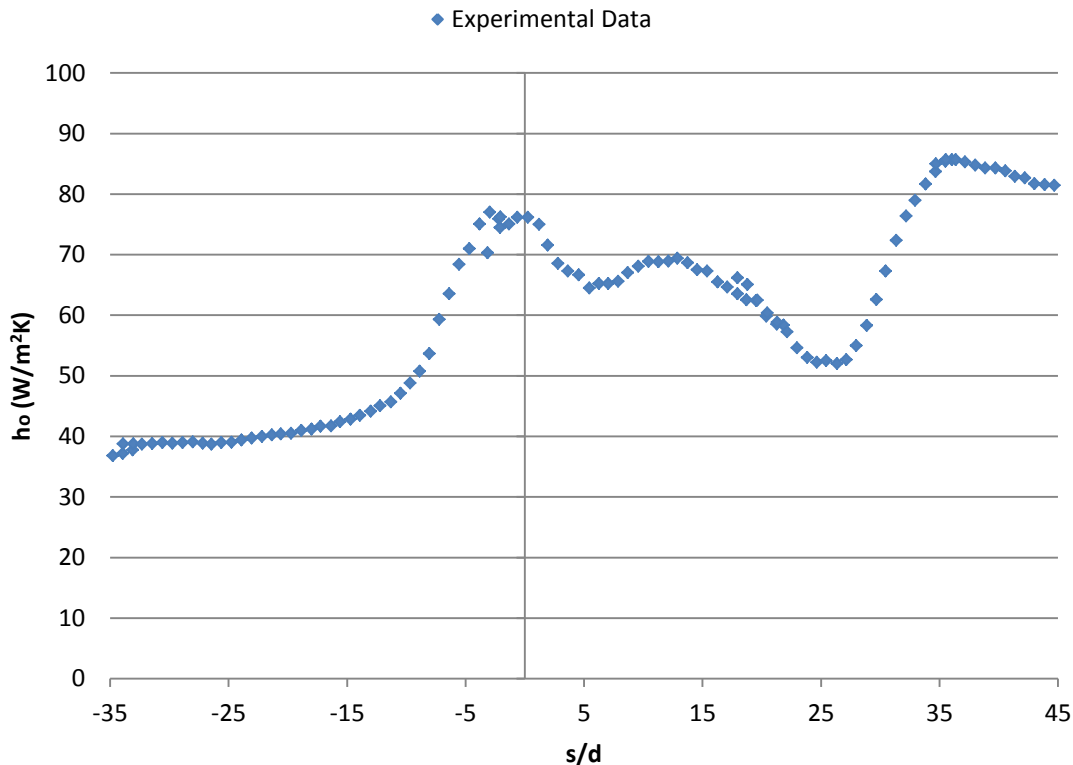


Figure 3.4: Heat transfer coefficient for an uncooled C3X vane, mainstream $T_u = 20\%$ (Dees, 2011)

A result that is immediately apparent from the laterally averaged data is that the no-mainstream test method provides highly unrealistic information about the cooling configuration effectiveness. Cooling effectiveness is unilaterally over-predicted, which would make this test method dangerous to use as a design tool, since the lifetime of a turbine component would be greatly reduced from what this test predicts. It is interesting to note that the difference in overall effectiveness of $\Delta\phi \approx 0.2$ between the mainstream-on and -off cases is roughly equal to the rise in effectiveness that comes about when a layer of thermal barrier coating (TBC) is applied to the outer vane wall (Figure 3.5). Any

relationship between the results obtained in the mainstream-off case and comparable results for a with-mainstream with-TBC case might therefore be an interesting area of future study.

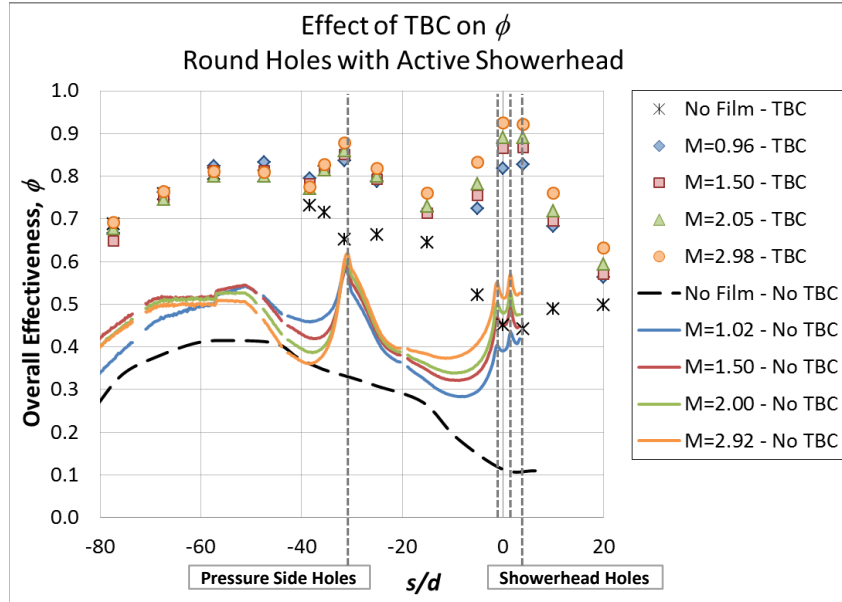


Figure 3.5: Effect of TBC on the overall effectiveness of a vane with round holes and an active showerhead
(Davidson, Kistenmacher, & Bogard, 2012)

3.2.2.2 Contour Data

A comparison of the contour data taken from the with-mainstream and no-mainstream cases reveals much of the same information as does the laterally averaged data: broadly, that effectiveness levels are much higher when no mainstream is applied (Figure 3.6). However, there is another significant result that is captured only in the contour data. Namely, there is a much greater spanwise variation in overall effectiveness in the with-mainstream case that is caused by the jet interacting with the surface of the test article. In the no-mainstream case, little variation in the spanwise overall effectiveness is observed, as all jets immediately separate upon exiting the film cooling holes.

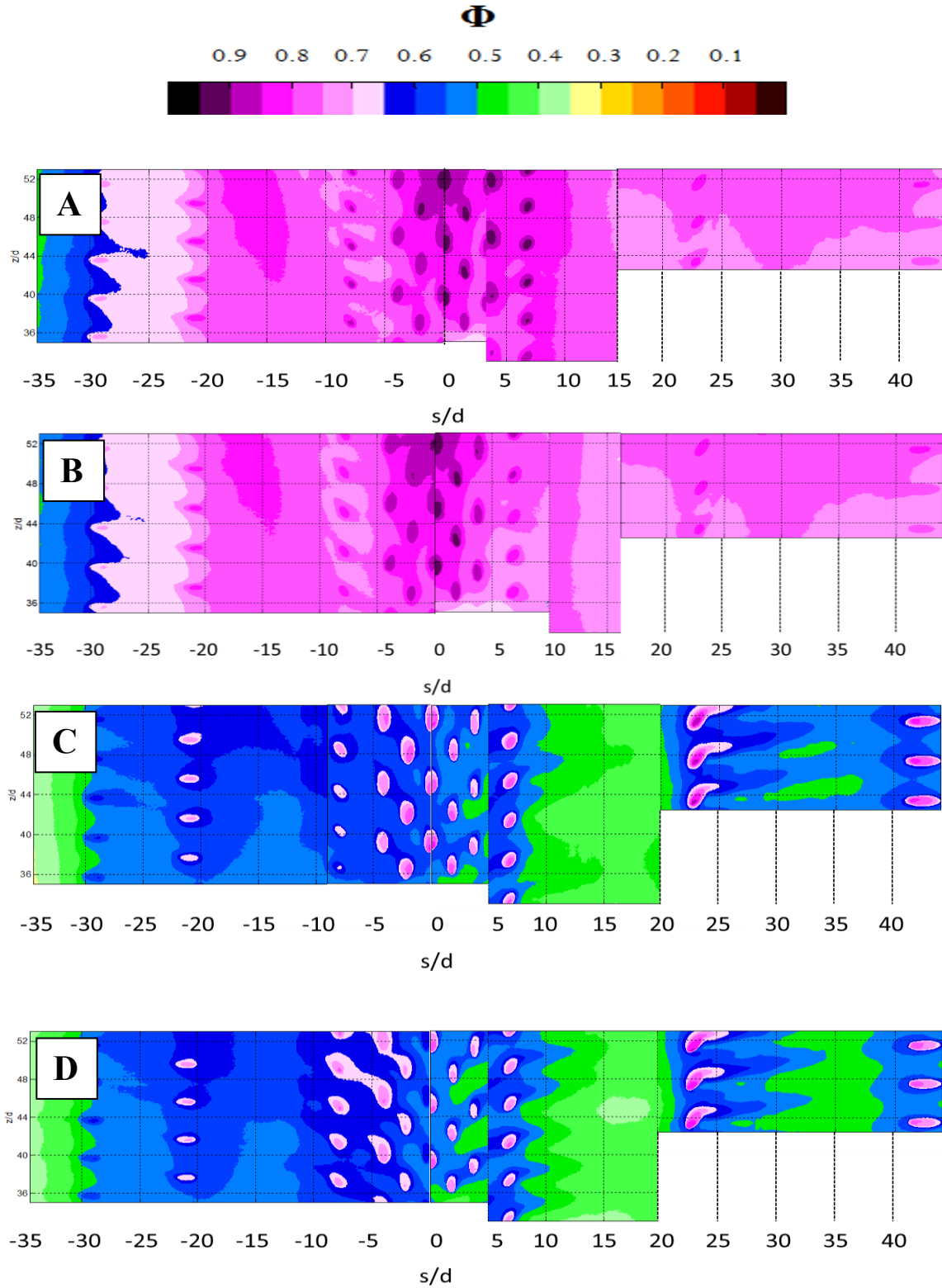


Figure 3.6: Contour plots of overall effectiveness (A) $M^* = 2.0$, Mainstream OFF; (B) $M^* = 1.0$; Mainstream OFF; (C) $M^* = 2.0$, Mainstream ON; (D) $M^* = 1.0$, Mainstream ON

These results are not out of line with expectations, but they do point to a potential flaw in any thermal defect testing methodology that takes place outside of a wind tunnel. It is significantly more difficult to identify the location of a cooling hole in the case without mainstream, since the temperature field is relatively uniform, making the detection of any improperly manufactured hole difficult to detect by thermal means. The with-mainstream case has an additional advantage, as not only is the hole visible, but a portion of the jet being discharged from it is as well. Being able to detect an individual jet's influence on surface temperature means that a fully or partially blocked hole would be more readily identified by a thermal inspection of the part, and therefore any test method that is able to accomplish this is preferred. The with-mainstream test is also able to detect hot spots that are not apparent in the no-mainstream case—for example, the showerhead hotspot appearing in the nominal case between $2 < x/d < 5$ and $40 < z/d < 48$ for both blowing ratios is not apparent in the mainstream-off case. Since hot spot detection is a major advantage of the overall cooling effectiveness test scheme, losing this capacity removes much of this methodology's utility.

3.2.3 Discussion of No-Mainstream Results

In the no-mainstream condition, laterally-averaged effectiveness for different blowing ratios collapse in the pressure side and suction side regions of the vane test article. This is contrary to the expected result, which would be a noticeable increase in cooling effectiveness with blowing ratio due to the increase in internal heat transfer. The external heat transfer coefficient is expected not to vary significantly between the high and low mass flow rate cases for the mainstream-off condition, since there is no forced mainstream convection in either case, and the film cooling jets separate immediately in

both cases, meaning they do not interact with the vane surface. A possible explanation for this effect is that since the test article is ejecting coolant into a relatively enclosed wind tunnel as opposed to an open room, the ejected coolant collects locally and has an indirect effect on the local external heat transfer coefficient. Ultimately, this hypothesis was not investigated further, since it was already abundantly clear that the no-mainstream case would not yield results representative of engine conditions. Since this test method was inherently unlikely to reproduce accurate results, subtleties in its execution were deemed unimportant.

In the showerhead, a different effect is observed. The laterally-averaged effectiveness experiences a slight overall increase when the blowing ratio is increased. An increase in blowing ratio in the showerhead would cause the heat transfer coefficient on the inside of the film cooling holes to increase in turn. As such, when the blowing ratio increases, the cooling effectiveness in this region would likewise rise due to the additional heat being convected into gas flowing through the holes and convected out through the densely-packed film holes. This would be an interesting result in that it complements the already fairly well-established notion that adiabatic effectiveness increases with blowing ratio in the showerhead region (Nathan, 2011), (Polanka, 1999). However, it is important to acknowledge that the increase in effectiveness in this area is somewhat less than the estimated uncertainty in overall effectiveness, and therefore was not clearly established.

3.3 Suggestions for Future Work in Testing of Vane Models in the Absence of a Mainstream

There are a number of possibilities for future work in vane testing without a hot mainstream. One weakness of this experiment as performed was that a small number of blowing ratios (two) were tested, over a range that was likewise relatively small (between $M^* = 1.0$ and $M^* = 2.0$ in the nominal condition). Since the result of a higher level of effectiveness in the showerhead region for a higher blowing ratio was close to the boundary of the measurement uncertainty, it would be worthwhile to test another higher blowing ratio (e.g. $M^* = 3.0$) to gain additional insight on whether this effect is physical, and to see if it continues with increasing blowing ratio even without a mainstream to heat the test article.

Another possibility is that the primary result seen in this test—that overall effectiveness increases steeply upon the removal of the mainstream, despite a presumed adiabatic effectiveness of nominally zero—is very similar to how the application of thermal barrier coating (TBC), a thin thermally insulating layer of ceramic, largely isolates the film cooling effectiveness from the overall effectiveness measured on a turbine vane (Kistenmacher, Davidson, & Bogard, 2013). If the results from testing a particular vane configuration with TBC and a hot mainstream were similar to the results from testing a vane without TBC and without a hot mainstream, the testing of actual blades on an assembly line might be greatly simplified for turbine components utilizing TBC. Alternately, tests could be conducted with and without a mainstream flow for a vane with TBC, and if those results were deemed sufficiently similar to one another, then this technique could be adapted for TBC-coated turbine components. If such a study

were undertaken, it would also be worthwhile to verify that the adiabatic effectiveness is in fact zero, as would be anticipated without any mainstream, to ensure that the no-mainstream test results are totally independent of film effect.

A final possibility for future testing is that laterally averaged external heat transfer coefficient data could be combined with the effectiveness data taken in the no-mainstream test to synthesize an estimate for the overall internal cooling effectiveness data in the nominal case. Note that previous work has involved predicting overall effectiveness by superposing adiabatic effectiveness and internal-only overall cooling effectiveness; the proposed future work would provide a new way of obtaining the internal cooling effectiveness. Since the heat transfer coefficient and adiabatic effectiveness data for the mainstream-on case already exist, the validity of this estimation method could be evaluated.

3.4 Overall Effectiveness Test Conclusions

It was shown that the level of overall effectiveness increases sharply upon the removal of the hot mainstream flow, which was in agreement with the initial hypothesis. This increase in effectiveness is at all locations on the vane; however the amount by which effectiveness increases depends on the specific position on the vane wall. It was observed that there existed no simple correlation to obtain the results of the with-mainstream case from the results of the no-mainstream case, and that knowledge of the external heat transfer coefficients in each case would be required to make such an estimation. Because of the failure of the no-mainstream case to predict the correct effectiveness values at engine conditions, this type of method was deemed to be

categorically unsuitable for testing thermal performance of engine parts on the factory floor.

Chapter 4: Design of a Turbulence Generator and Other Components in Support of a Wind Tunnel Test Section Redesign

This chapter describes work done in support of development of a new wind tunnel facility to test cooling performance for turbine airfoils with varying angles for the approach flow. A key part of this work was to design a turbulence grid that could be placed at varying angles to the flow without disturbing the flow direction. Tests were performed to determine any change in turbulence quantities (particularly turbulence intensity and length scale) that would be due to the angling of the grid. A planar rod grid of solidity $S = 0.25$ was tested at constant downstream distance with inlet flow angles 0° , 25° , 35° , and 45° with respect to the grid normal; a second grid of $S = 0.50$ was tested with an inlet flow angle of 0° for reference. One test was performed on the $S = 0.25$ grid at 45° in which the downstream distance was varied; this was done in order to make a comparison between the results in this study and correlations defined in the literature. This chapter also includes work done to investigate major pressure losses in the current wind tunnel facility and redesign of the coolant flow loop to provide more coolant flow for the future facility.

4.1 Investigation of the Effect of Inlet Flow Incidence Angle on the Flow

Downstream of a Turbulence Generator

A new wind tunnel test section design was devised that made possible the testing of blades and vanes of different incidence angles. This particular setup required a turbulence generator to be placed at varying angles to the flow, depending on the angle of the flow incident to the blade or vane cascade. The effects of angling a turbulence generator with respect to the approach flow had not been investigated in the academic

literature, so it was uncertain as to whether or not this angling would affect turbulence properties downstream. Therefore, an experiment was performed in which a turbulence grid was angled with respect to the approach flow and the turbulence quantities were measured downstream; this was compared to a baseline test wherein the turbulence generator was placed normal to the flow, as was done in studies in the literature. The design of the turbulence generator and the test results are presented in this section.

4.1.1 Scope of Academic Literature

Baines and Peterson were among the first to quantify the decay of turbulence downstream of a passive turbulence generator (Baines & Peterson, 1951). The study, “An Investigation of Flow through Screens,” presents a correlation for the turbulent intensity at given normalized distance downstream of a turbulence generator, where the width of an individual constituent grid component (e.g. the width of a square bar, or the diameter of a cylinder) being used to generate the turbulence is used as the normalizing length:

$$\frac{u_{rms}}{\bar{U}} = 1.12 \left(\frac{x}{b} \right)^{-\frac{5}{7}} \quad (4.1)$$

Where u_{rms} is the root mean square of the fluctuations in instantaneous velocity, \bar{U} is the mean velocity, x is the distance downstream of the turbulence generator, and b is the diameter of an individual turbulence rod. This study also presented this ratio scaled by x/M , where M is the distance between turbulence bar centerlines, instead of x/b ; the increased scatter in the data when this was chosen as the scaling parameter indicates that

$\frac{u_{rms}}{\bar{U}}$ scales better with x/b . A common way of expressing this ratio is to call it turbulence intensity:

$$Tu = \frac{u_{rms}}{\bar{U}} * 100\% \quad (4.2)$$

Where the turbulence intensity, Tu , is expressed in terms of percentage.

This study focused on turbulence generators of solidities between $S = 0.125$ and $S = 0.5$, where the solidity S is defined in the following manner:

$$S = \frac{A_{solid}}{A_{total}} = \frac{b}{M} \text{ (for planar rod type grids)} \quad (4.3)$$

The variable M here represents the distance between adjacent turbulence rod centerlines. Baines and Peterson (1951) noted that the correlations began to fail above the maximum solidity of $S = 0.50$ they presented in their results; the cause of this deviation was attributed to instabilities within the flow. All of the tests in their study were for flow approaching the turbulence generator from the normal angle, and grids tested were of either the square bi-planar type or perforated plate type (Figure 4.1).

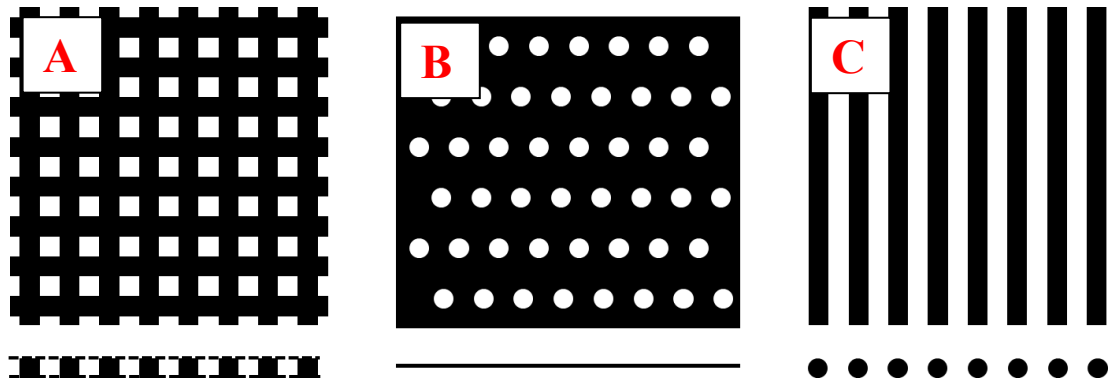


Figure 4.1: Common passive turbulence generator configurations: (A) Bi-planar square rods; (B) Perforated plate; (C) Planar rods

Roach (1987) expounded further upon the research of Baines and Peterson by testing grids of different shapes on top of the other parameters that had been varied in previous studies. These designs included square bi-planar arrays, square planar arrays, bi-planar rod arrays, planar rod arrays, and perforated plates. Each of these shapes had different correlations for turbulence intensity versus normalized downstream distance; the square bi-planar correlation developed by Roach provides results that are within 1% of those obtained using the correlation found by Baines and Peterson for similar grid geometry.

Taylor et al (1947) presented results correlating the effect of the incidence angle of flow into a screen with the angle by which the flow direction changes as it exits the screen. The correlation they developed indicated that the inflow to outflow angle difference, or angle defect, increases with the screen's loss coefficient. They also observed that the magnitude of the outflow angle with respect to the normal was always lower than the magnitude of the inlet angle. Laws and Livesy (1978) followed in the footsteps of Taylor et al (1947) by developing a correlations for angle defect that were more rigorous in terms of acknowledging that a turbulence generator is not completely flat, and that simply 2-D geometric assumptions cannot be used to obtain the flow defect angle. Davis (1962) also produced correlations for expected outflow angle and mean velocity profile downstream of a screen given a particular velocity profile incoming to the screen. However, all three of these papers stop short of characterizing turbulence produced by a screen or grid with an angled inlet flow.

4.1.2 The Design of a Turbulence Generator to be used with Off-Normal Approach

Angle Flow

A turbulence generator was designed with the goal of producing a specific turbulence intensity and integral length scale at a distance downstream of the grid. The turbulence generator was required to produce the same turbulence quantities for different flow angles for the upcoming testing of blades with different inlet flow angles to be placed in a new test section.

4.1.2.1 Design Constraints

The turbulence generator was initially designed to be an array of horizontal bars normal to the flow in the new tunnel. This design was thought to be expedient for a number of reasons. First, it followed the same physics as the vertical bar setups that have been consistently used in this laboratory, so it was believed that their design could be well-informed by data previously gathered; second, it happened to be convenient in terms of the ease of changing the setup of the wind tunnel; third, when the bars are placed horizontally as described, the solidity of the turbulence rod array does not change when the incident flow angle changes, so the same turbulence characteristics would be expected for every flow incidence angle; fourth, the turbulence array axis would always be parallel and equidistant to the blade cascade axis, no matter the incidence angle being tested (this being reflective of the design of the particular test section in question).

However, when such a horizontal bar grid is placed at a nonzero incidence angle with respect to the approach flow, the cylinders cause the flow to lose momentum in the direction of the rod axis (manifested as a force normal to the cascade axis). This has the

effect of changing the angle of the outflow toward the direction normal to the array. This angle defect increases with increased loss coefficient K value for the array; depending on the method used to estimate the K value of the array (Mehta, 1977) and the specific angular orientation being examined (Taylor et al, 1947), the angle defect as calculated via equations in the literature was estimated to be between 3 and 15 degrees. Such a significant change in outflow angle renders this particular array design effectively useless, since the direction of the flow incident to the blades is to be highly controlled in upcoming experiments. Any such change in flow angle would be deemed unacceptable, so a new design was sought.

To get around this issue, sacrifices were made in terms of convenience of setup, and a vertical bar array was chosen. A vertical rod array should not cause any defect in angle, since the drag force on the cylinder will be always be parallel to the flow: the cylinder is axisymmetric, and if the cylinder is placed vertically, then the flow incident upon it will always be normal to the individual rod axes (Figure 4.2).

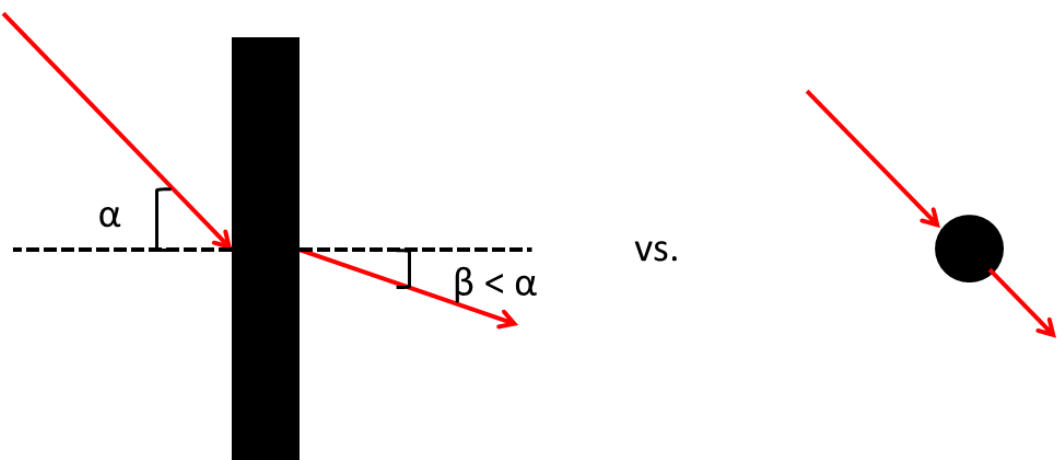


Figure 4.2: Flow angle defect caused by non-normal incident flow for a non-axisymmetric flow obstruction is avoided by using an element that is axisymmetric

4.1.2.2 Design towards a Specified Turbulence Intensity

As mentioned previously, there are numerous correlations in the literature that relate downstream distance from the grid to the turbulence intensity on that plane. Since planar rods were ultimately chosen in order to preserve the angle incidence of the outflow, a correlation from Roach (1987) was chosen for this geometric configuration:

$$\frac{u_{rms}}{\bar{U}} = 0.80 \left(\frac{x}{b} \right)^{-\frac{5}{7}} \quad (4.4)$$

Given the need for a turbulence intensity of $Tu = 5\%$ at a distance $x = 18''$ downstream of the grid, a rod diameter of $b = 0.371''$ was required; this was rounded to $b = 0.375''$ since this size rod was readily available for purchase without the need to turn it to the correct diameter value. Based on this correlation, the expected turbulence intensity value at a distance of $x = 18''$ downstream of the generator would be 5.04%, which is well within the uncertainty limit for this particular measurement and therefore deemed to be acceptable.

4.1.2.3 Design towards a Specified Integral Length Scale

There was a specified target length scale that the turbulence generator should be able to attain. However, it is worth mentioning that it is hard to predict exactly what length scales will be produced by a particular turbulence generator. There are correlations for how normalized length scales Λ_x/b grow with non-dimensional distance x/b away from the generator, but these correlations do not appear to capture all of the physics, since there is significant deviation in the data presented within the literature.

However, for all of the literature data examined, the exponential growth rate of non-dimensional length scale with non-dimensional distance is consistent.

Data from Baines and Peterson (1951) as well as Roach (1987) were used to make predictions of what length scales would be produced. Roach suggests that the length scale at a downstream distance can be predicted using the following correlation:

$$\Lambda_x/b = 0.20 \left(\frac{x}{b}\right)^{\frac{1}{2}} \quad (4.5)$$

A length scale prediction supplied by this equation at the turbulence generator design point, using the non-dimensional distance $\frac{x}{b} = 48.5$, would be $\Lambda_x = 1.39$ cm, corresponding to 4.2% axial chord length. The power growth rate is credible, but there is considerable scatter in the data presented in this paper, indicating that this length scale prediction is a fairly rough estimate (Figure 4.3). Similarly, length scale data presented in Baines and Peterson exhibits a significant amount of scatter. However, a plot from that paper (Figure 4.4) seems to imply that, at least for the range of values of b tested, smaller mesh elements have proportionately larger length scales associated with them, and that non-dimensionalized downstream grid distance itself is not the only factor in determining normalized length scales. Therefore, it is acknowledged that any such correlation may stray somewhat from experimental results.

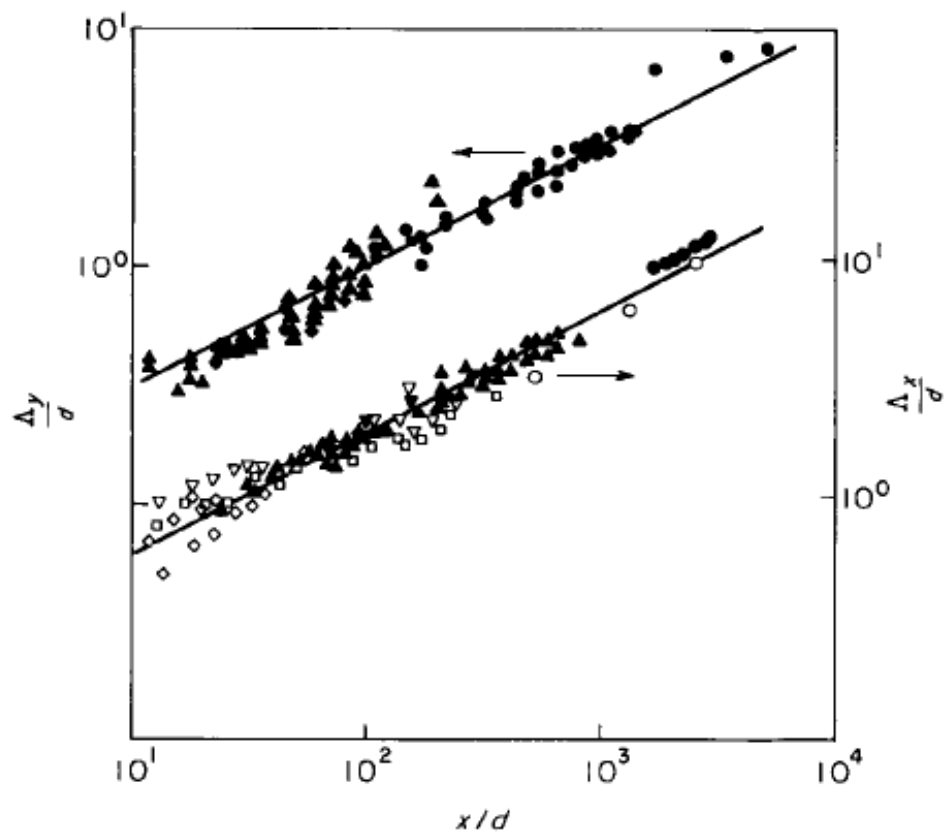


Figure 9 Integral scale growth downstream of grids. Symbols as given in Table 2. Curve fits: $\Lambda_x/d=0.20(x/d)^{1/2}$; $\Lambda_y/d=0.10(x/d)^{1/2}$

Figure 4.3: Predicted turbulence integral length scales downstream of a passive turbulence generator (Roach, 1987)

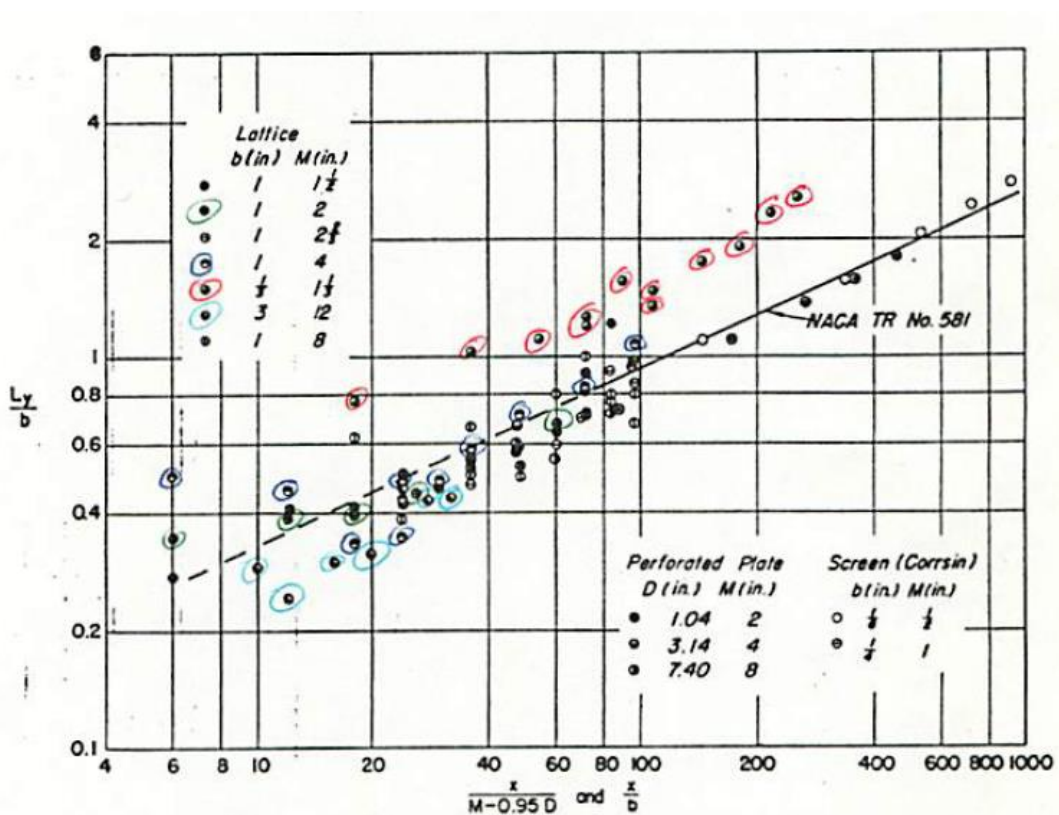


Figure 4.4: Transverse integral length scales as a function of normalized downstream distance from turbulence generator (Baines & Peterson, 1951)

Using the data for $b = 1/3"$ (circled in red in Figure 4.4) to graphically predict the length scales, a value of $\Lambda_x = 1.5$ cm was estimated; this would correspond to 4.6% axial chord length. This value is sufficiently close to the design criteria. This design to a particular desired length scale was performed acknowledging that the correlations might not be accurate for all possible test setups, and that the design might have to change based on the length scales that would be directly measured in future experiments.

Another major concern in the design of the turbulence rods was to ensure that the rods would be able to remove any evidence of a wake from the turning vanes that would

be placed just upstream of them in the new wind tunnel being designed. A design decision was made to have the number of turbulence rods per turning vane pitch to be an integer, so that the wakes coming from each turning vane would be periodic with turbulence rod position. This would allow for the grid to be adjusted somewhat, so that (for example) each of the turning vane wakes could either pass between a pair of rods or impinge directly upon a rod.

4.1.3 Angled Turbulence Generator Test Experimental Results and Conclusions

A series of experiments was conducted on the effects of grid angle with respect to mainstream flow on the turbulence quantities in the flow downstream of a turbulence generator. The experimental test matrix is described in Chapter 2 in Table 2.3.

For each of the experiments performed, the traversing line was placed 39 ± 1.5 rod diameters downstream of the turbulence grid. Ideally, all experiments would have taken place 48.5 diameters downstream of the turbulence grid in order to provide results as comparable as possible to what will be produced in the new wind tunnel facility. However, in the current facility, this proved to be unworkable for the most extreme angle being tested due to spatial limitations in the test setup. Instead, tests were all performed slightly closer to the grid in order to be consistent.

Figure 4.5 is a graph showing the turbulence intensity across a portion of the width of the wind tunnel at a distance of $x/b = 39.5$ downstream of the grid. This plot includes the data taken at all approach flow angles tested (including the normal angle). All but one test configuration is displayed: the case for 45° with variable distance is not

shown, but will be the subject of later discussion. The symbol W represents the width of the tunnel, and z the distance into the tunnel from the outer tunnel wall.

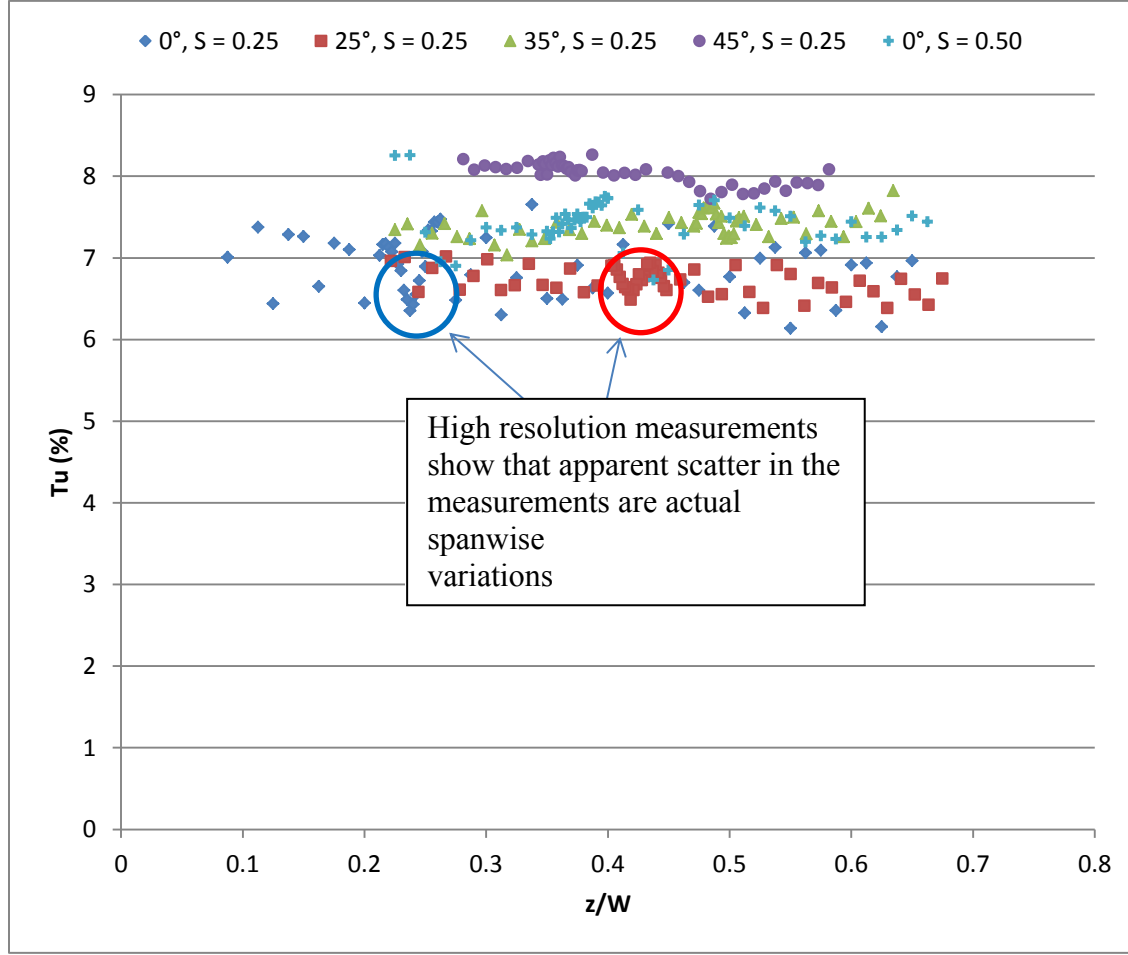


Figure 4.5: Turbulence intensity across the width of the wind tunnel at different grid angle configurations at $x/b = 39.5$

It is worth mentioning that the turbulence levels that are observed across the width of the tunnel are non-uniform. Some non-uniformity is to be expected due to the precision of the measurements being taken. However, it is apparent that the magnitude of the non-uniformity is significantly greater than the quoted precision uncertainty. The peaks and valleys in the turbulence intensity, where they are apparent, can be shown to

occur at regular intervals that correspond to the pitch between individual rods within the turbulence grid. The amplitude of these peaks is seen to decrease with increasing flow incidence angle. This is not unexpected: as the flow angle changes, the solidity of the grid with respect to the flow direction changes as well:

$$S_\theta = \frac{b}{M * \cos(\theta)} \quad (4.6)$$

Where θ is the flow angle with respect to the normal of the grid. (Note that this formulation allows the solidity to increase beyond the previous maximum of 1. Since solidity is a 2-D concept and an angled grid is 3-D in nature, the concept of solidity breaks down somewhat. The upper range of solidity values were not explored in this experiment.) This increase in solidity with the incidence angle effectively creates more interaction between the individual rods' wakes. Since the wakes are all regions of high mixing, this in turn means that the turbulent kinetic energy and turbulence intensity are likewise mixed so that they become more uniform.

Another apparent effect is an increase in turbulence intensity with flow incidence angle for a particular downstream distance. This effect is significantly more pronounced for the 35 and 45 degree cases. It is worth noting, though, that due to spatial limitations, the traversing line for the 25 degree case was placed at a distance 1.2" greater than for the 0 degree case. Therefore, the fact that this turbulence intensity seems to match the 0 degree case fairly well is artificial, and it should be recognized that a correction for distance must be applied. The added correction factor was taken to be the difference between the turbulence intensities that would be expected via Roach's correlation at the x/b values indicated—this correction value ended up being $Tu_{corr} = 0.35\%$. Using this

corrected value for the 25 degree case, the mean turbulence intensity for each test was calculated (Table 4.1). Based on the result, it can be concluded that, in the range of angles tested, there is a monotonic increase in turbulence level generated at a sufficiently far distance from the grid.

Angle (°)	Solidity	Angular Solidity	Mean Tu (%)	Uncertainty in Tu (%)
0	0.25	0.25	6.89	0.09
25	0.25	0.28	7.06*	0.04
35	0.25	0.31	7.41	0.04
45	0.25	0.35	8.19	0.04
0	0.50	0.50	7.44	0.07

*value corrected based on location being $x/b = 3$ farther downstream than other measurements

Table 4.1: Mean turbulence intensity for each angle and solidity tested

Here, the quoted uncertainties are precision only. It is important to recognize that an increase in effective rod solidity could be contributing to the rise in turbulence intensity: the decrease in projected area between the rods means the flow is forced to accelerate more through the grid. The increased velocity between the rods for a higher solidity case could mean that a greater velocity gradient is experienced between this section and the wake, thereby generating more turbulent kinetic energy. However, for the 0 degree case with $S = 0.50$, the turbulence intensity is almost uniformly lower in magnitude in comparison to the 45 degree case, wherein the projected solidity is only $S_\theta = 0.35$. Therefore, it seems quite unlikely that the relatively small projected solidity difference between the different angled cases would be the cause of this effect. The most sensible conclusion that can be drawn is that grid angle does in fact have an impact on the downstream turbulence intensity. However, this is expressed with the caveat that the turbulence intensity was not recorded over the entire width of the tunnel, and since the

spatial variation in the high solidity 0 degree case was quite high, the turbulence intensity could theoretically have been higher at other locations not examined along the same traversing line.

Although no sources in the academic literature suggest outright that turbulence intensity (or RMS velocity) is affected by grid incidence angle, a number of physical effects have been investigated that could contribute to this effect. First, it has been documented that a screen placed at an angle with respect to an approach flow of uniform velocity creates a mean velocity gradient downstream (Davis, 1962). An increased mean velocity gradient across the tunnel width would globally increase the rate of turbulence production, possibly resulting in higher observed downstream turbulence intensity. This would require the magnitude of the mean velocity gradient to decrease fairly rapidly in space, though, since no distinct mean velocity gradient was observed within the tunnel during testing (Figure 4.6). Alternately, the global increase in turbulence intensity could be caused by a local effect that mixes laterally so that it appears uniform downstream. One such possibility is that an elevated velocity gradient is produced on one half of a given rod's wake due to the local acceleration of the flow around the adjacent rod that is slightly upstream (due to the flow incidence angle) (Figure 4.7). This in turn could create a local area of increased turbulence production whose energy is transported laterally as it moves downstream, causing it to eventually appear uniform. While either one of these might be a reasonable hypothesis for the physical cause of the effect described above, insufficient data have been gathered to test these hypotheses and come to a conclusion.

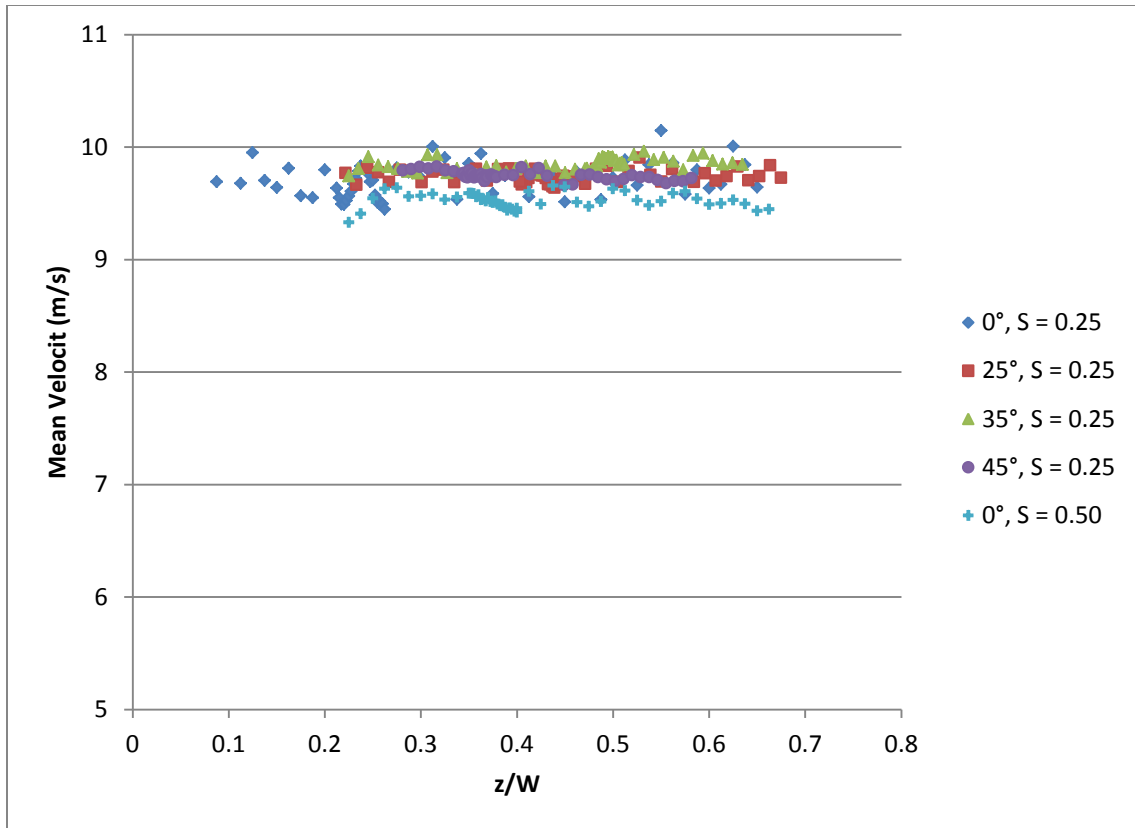


Figure 4.6: Mean velocity profiles along traversing planes during turbulence quantity experiments

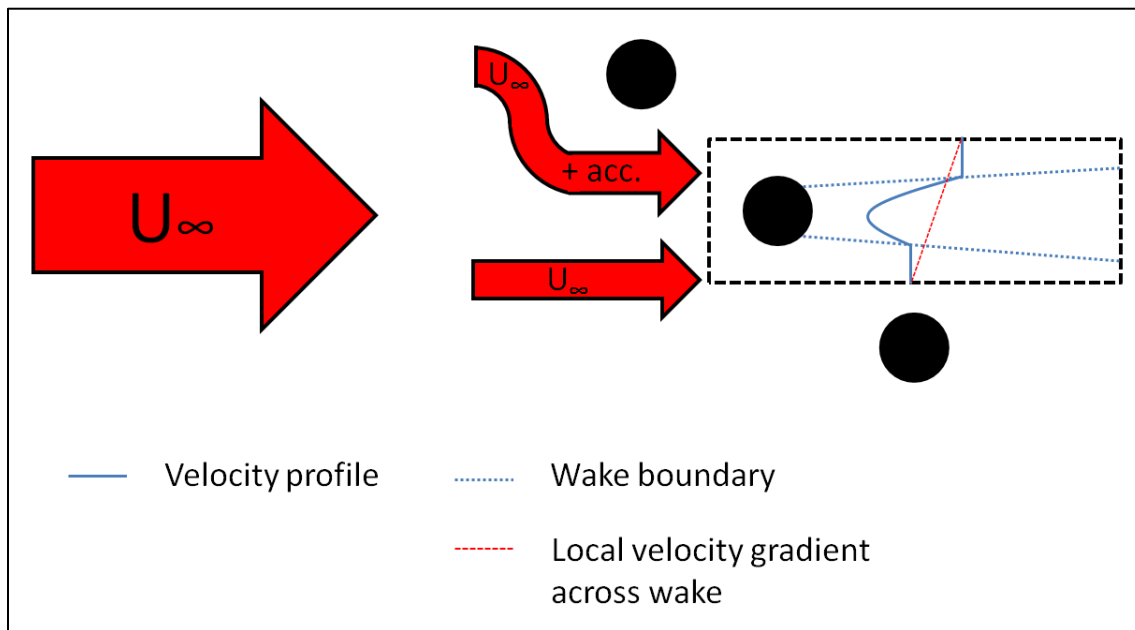


Figure 4.7: Increased velocity gradient magnitude across angled turbulence grid wakes

Another experiment was conducted for the 45 degree case in which the downstream distance between the turbulence grid and the hot wire probe was varied. This was done in order to form a basis of comparison between the most extreme angle case and the correlations formulated by Roach (1987) for the normal case (Figure 4.8).

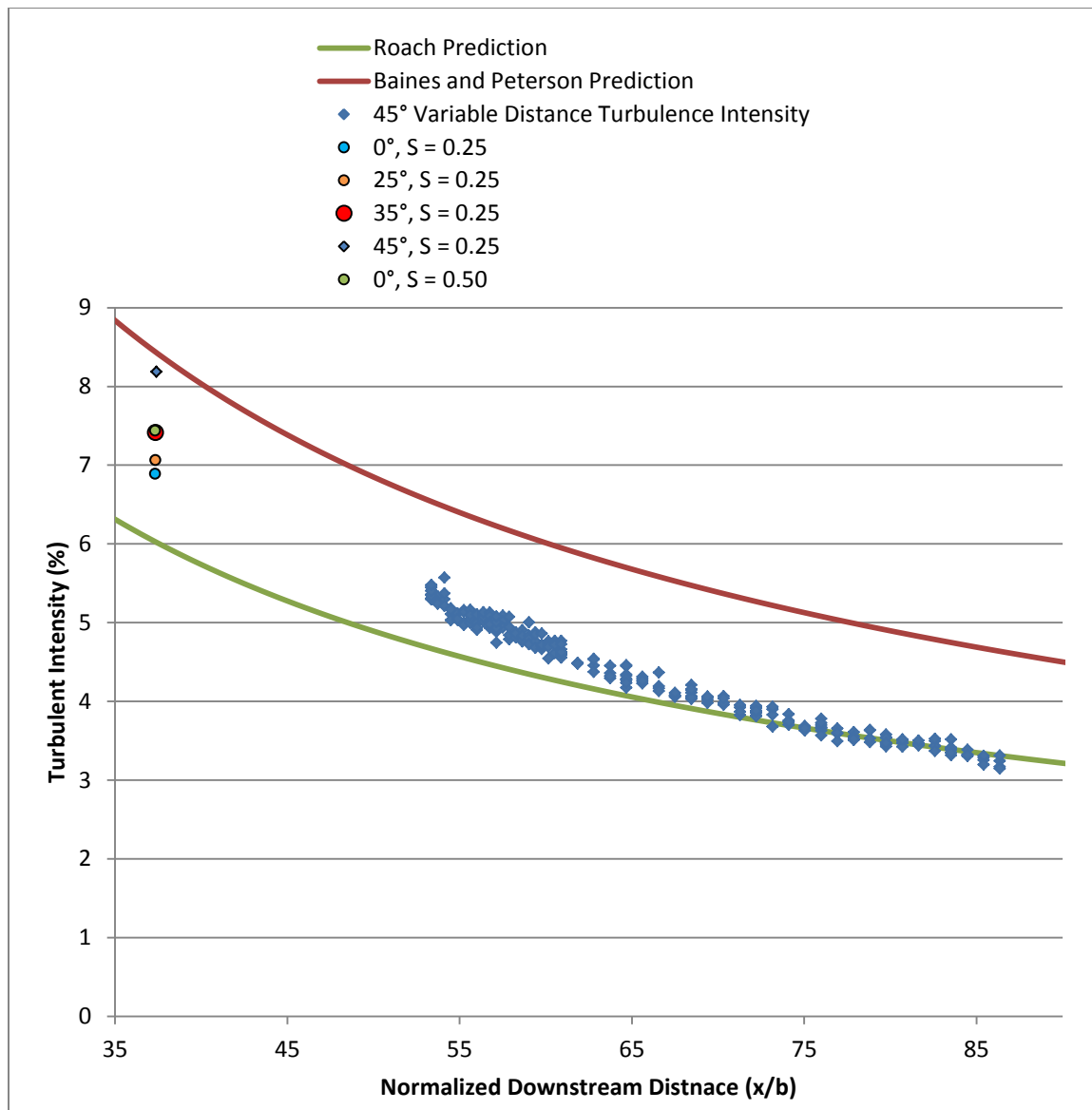


Figure 4.8: Turbulence intensity with downstream distance from a grid placed at 45 degrees with respect to the approach flow

It is interesting to note that the data taken falls reasonably well between the two predictions; it is also interesting that at a sufficiently distant location downstream of the grid, the measured turbulence intensity converges on the prediction made by Roach for grids of the type being tested. Since the 45 degree case is the most extreme angle that was tested, it also implies that the Roach correlation may be accurate for other angles at a sufficiently large downstream distance. Although a compelling idea, this is currently left as a hypothesis as it is untested.

A final consideration is turbulence isotropy. Both the Baines and Peterson and the Roach correlations assume the continual dissipation of isotropic turbulence starting immediately downstream of the grid; the -5/7ths power corresponds to the decay rate of isotropic turbulence as predicted by Kolmogorov. If this condition were satisfied, the correlation constant obtained from the experimental data (e.g. 0.80 for Roach; 1.12 for Baines and Peterson) would have exactly one value for a given grid. However, it is apparent that the data obtained in this experiment possess a range of such coefficients, since the turbulence experienced initially is greater than Roach predicts, but then decays to the expected level further downstream. This implies at least one of two things: first, it could mean that the turbulence is not decaying isotropically in this region, since it does not appear to follow the -5/7ths power law. Second, it could mean that using the grid location as the starting point for isotropic turbulence in the correlation is flawed—this is in fact quite likely, since it has been widely observed that the turbulence fields generated by a passive grid achieve isotropy at least several diameters downstream of the grid. This would imply that a new origin for the start point of isotropic turbulence decay should be created in order to be strictly more accurate:

$$Tu = A \left(\frac{x-x_0}{b} \right)^{-\frac{5}{7}} \quad (4.7)$$

Here, A refers to some constant correlation coefficient, and x_0 refers to the new origin at which purely isotropic turbulence exists and begins to decay. For example, if a value for the downstream distance at which isotropy is reached is guessed to be $x_0 = 7''$ downstream of the grid, the following is obtained (Figure 4.9). In this figure, the coefficient A is back-calculated using the calculated turbulence intensity at each point, and assuming that the turbulence does decay at a $-5/7$ exponential rate everywhere.

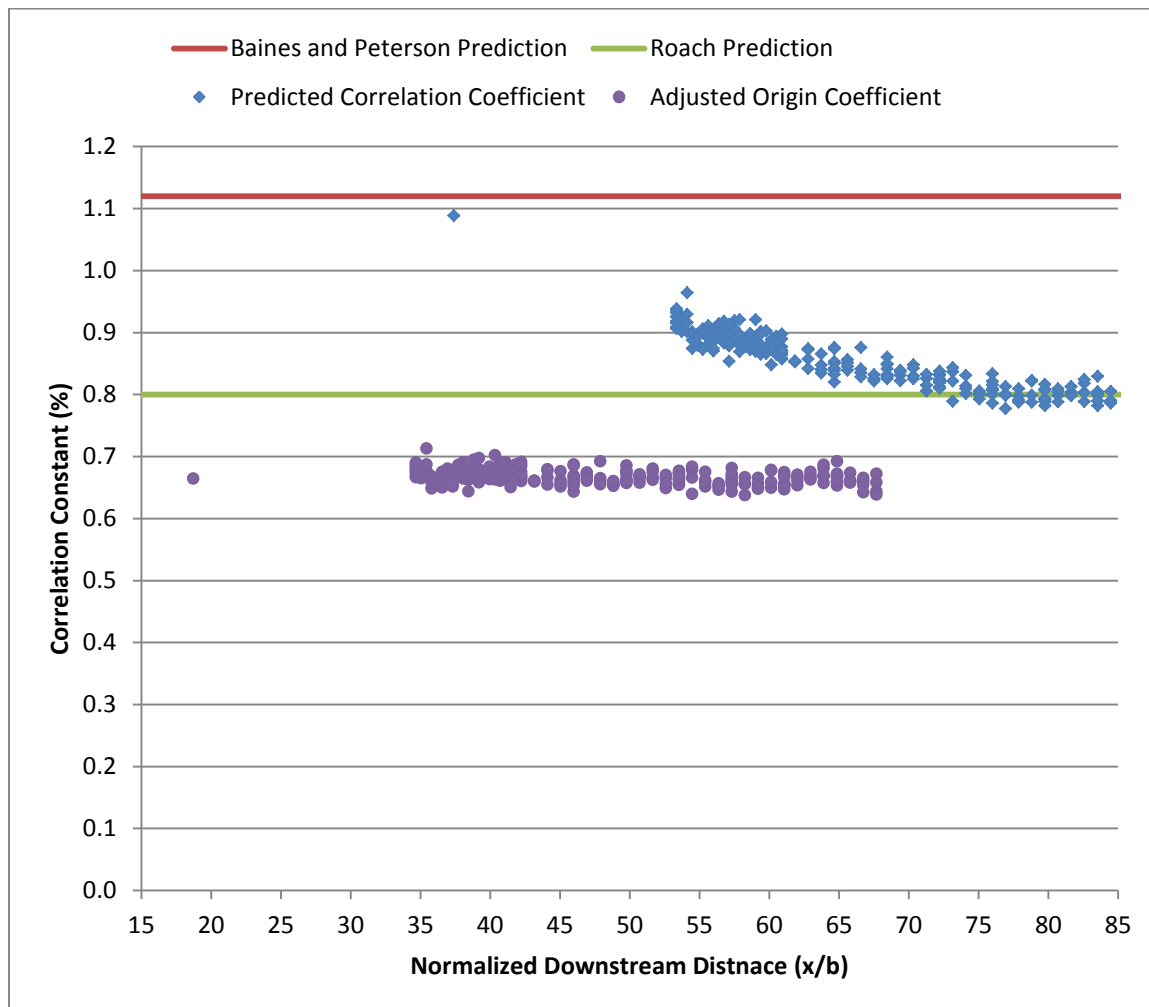


Figure 4.9: Turbulence intensity correlation coefficient for varying distance downstream of a grid

Note that the constant, A , as defined in the previous equation is much closer to invariant with downstream distance in the adjusted origin case. However, without having collected data much closer to the turbulence grid, it is impossible to ascertain the exact plane at which the turbulence becomes both isotropic or starts decaying. Additionally, it is possible that the adjusted origin coefficient data may stray away from being constant further upstream or downstream of the values measured. Therefore, this sort of analysis might be considered future work, since data has not been gathered over a great enough breadth of downstream distance to make any conclusions.

Integral length scale measurements were also made (Figure 4.10) for all configurations. As mentioned previously in Chapter 2, the low precision uncertainty of these measurements makes it difficult to draw conclusions about the effects of incidence angle on the integral length scale. The only concrete result is that there was significantly less precision uncertainty in turbulence length scale for the 0 degree high solidity case; this could have been because the reduced spacing between the rods limits the size of the eddies that can be formed, thereby also limiting the range of the sizes and the precision uncertainty of the measurement. It is also curious that virtually all of the measurements of length scale were greater in magnitude than the values predicted by either Baines and Peterson or Roach. However, it should be noted again that there was significant scatter in the length scale data from both of these papers.

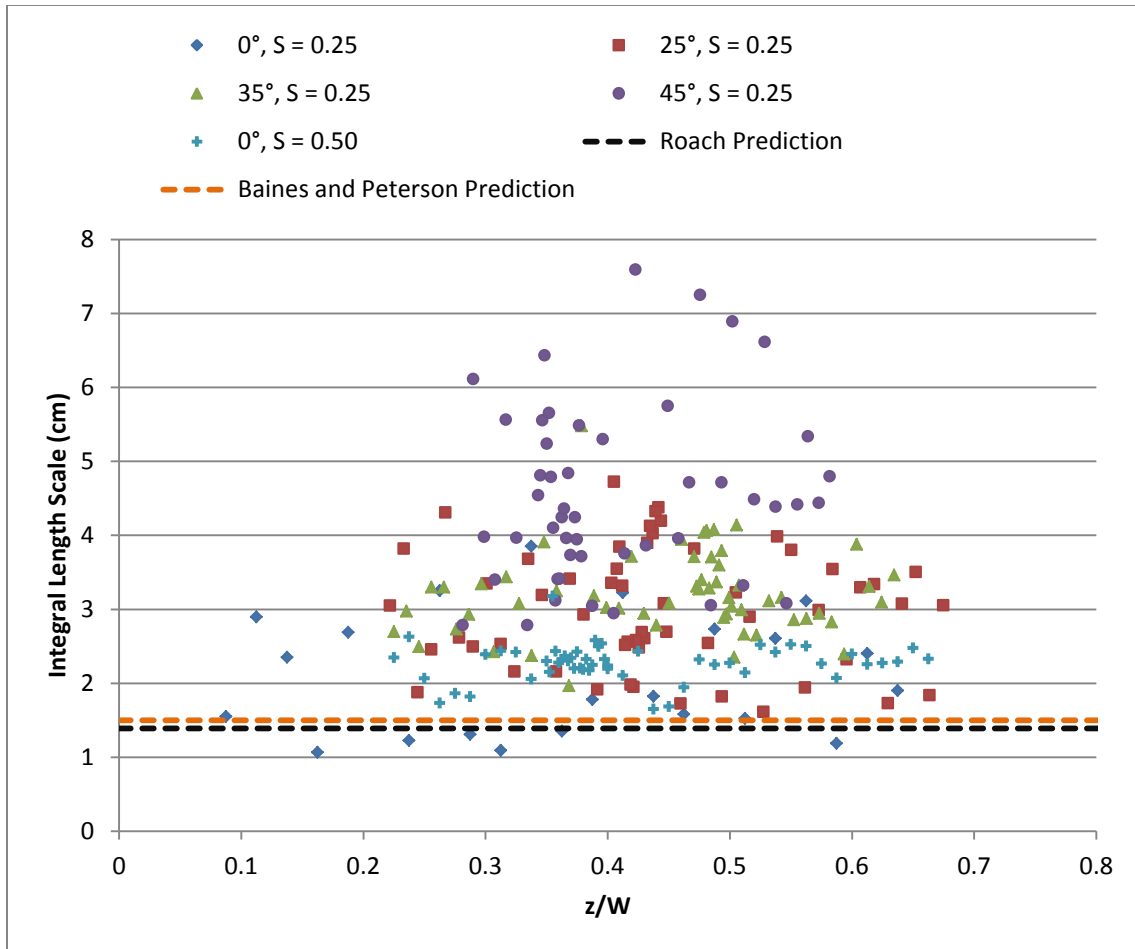


Figure 4.10: Integral length scales measured across the width of a wind tunnel test section

In an attempt to draw conclusions from the data, it was presumed that the length scale was not dependent on the probe location (i.e. the integral length scale was on average constant across the tunnel width). This allowed an ensemble average to be taken of the length scale data at each angle (Table 4.2):

Angle ($^\circ$)	Solidity	Angular Solidity	Mean L_x (cm)	Uncertainty in L_x (cm)
0	0.25	0.25	2.07	0.21
25	0.25	0.28	3.00	0.21
35	0.25	0.31	3.21	0.15
45	0.25	0.35	4.53	0.34
0	0.50	0.50	2.28	0.07

Table 4.2: Average integral length scales for each approach flow turbulence test configuration

Here, the quoted uncertainties are precision only. When an ensemble average of the data has been taken, it appears that there is a tendency towards the production of larger length scales with increasing flow incidence angle. (Note that this is difficult to say definitively, since the length scales for the 25 and 35 degree cases are more or less the same within uncertainty.) From these results, the integral length scale does not appear to be a strong function of grid solidity, as the length scales for the high and low solidity 0 degree test cases are close to equal within uncertainty, which is consistent with the correlations used to predict length scales in the literature (Roach, 1987).

4.1.4 Future Work in Quantifying the Turbulence Downstream of a Turbulence Generator with Off-Normal Approach Flow Angle

Since it is a relatively unexplored area of the study of passively generated nearly-isotropic turbulence, there is ample room for additional studies regarding the effects of having an approach flow that is at an angle with respect to the generator's normal vector. One important validation for the experiments performed in this study—that the turbulence was in fact isotropic—was presumed rather than experimentally determined. Having obtained a correlation constant A that varied with grid downstream distance draws this somewhat into question. A rigorous analysis of turbulence isotropy should be performed as a future experiment. This validation might be done using either a multiple-wire hot wire anemometer, or by using a three-component laser Doppler velocimeter (LDV) if time-resolved measurements such as length scale are not important.

Although all turbulence generator elements in this configuration are axisymmetric and individually do not produce drag forces that create an angle defect between the outflow and inflow angles to the grid, no test has been performed to ascertain whether or

not the grid as a whole produces such an effect. It would be useful to perform a validation on the velocity profiles extending downstream of the turbulence rods; this could be done with relative ease by using a particle image velocimeter (PIV) to visualize the flow field data. Traversing a multiple-component hot wire probe or a two-or-more-component LDV probe volume in a raster pattern downstream of the turbulence rods would also produce comparable results.

A third experiment that would be worth conducting would be one performed in the same manner as the turbulence measurements presented by Baines and Peterson (1951) or Roach (1987), wherein a correlation for turbulence intensity versus normalized downstream distance is performed. This would be a compact way of expressing the essence of the physical effects that have been examined in this study, and it could be done for any variety of relative inflow angles. Depending on the results of this study, it might be possible to also represent all of the data with a single correlation relating turbulence intensity to normalized downstream distance and approach flow angle. Such an experiment would ideally resolve the question of where precisely the decay of turbulence intensity becomes uniform. These sets of experiments could be performed using an LDV, a multiple-wire hot wire, or a PIV system.

Finally, this current study was insufficient in terms of identifying the effect of turbulence grid angle on the turbulence integral length scale. Another study could be performed in which a vast amount of data points were taken at downstream locations in order to reduce the precision uncertainty of the measurement. This would ideally be done with a hot wire probe in a similar manner as was undertaken in this experiment, but

would likely require a newer, more sophisticated processing scheme appropriate for more the more data-intensive experiment.

4.1.5 Wake Influence Test Experimental Results

A brief study was performed to investigate the effect of a single wake in the approach flow upstream of the turbulence generator. The purpose of this study was to make a rough evaluation of the effect that the velocity defect and increased turbulence in the wake of a turning vane would have on the turbulence quantities produced by the passive turbulence generator at one of the measurement planes previously investigated, and if the wake is removed by the turbulence generator.

For this test, a single rod was used to create a wake upstream of the turbulence generator; it was assumed that whatever effect this single rod would have would not change when multiple such rods would be placed periodically across the width of the tunnel, as a cascade of turning vanes would be arranged. The diameter of the rod and its upstream distance from the turbulence grid were set in order to match the expected wake width and maximum velocity defect that a particular existing turning vane design was expected to generate. The wake properties behind the single cylinder in cross-flow were predicted using data in a paper, “The Velocity Field of the Turbulent Very Near Wake of a Circular Cylinder”, which observed these effects at a diameter Reynolds number of $Re_d = 3900$ (Ong & Wallace, 1996). It is worth mentioning that there are papers discussing wakes behind a cylinder in cross-flow at a wealth of different Reynolds numbers, and the one that was used to determine the experimental setup was decided by estimating the cylinder size that would be used and calculating its corresponding Reynolds number. The paper citing a Reynolds number closest to the estimated value was then used to calculate

wake properties and the new, correct rod diameter; this new diameter's corresponding Reynolds number was calculated in turn and evaluated to be similar to that of the one in the paper, legitimizing the prior analysis. The turning vane wake properties were estimated by another TTCRL member, Kyle Chavez, using 2-D CFD; the turbulence model used was the $k-\omega$ SST model. At the downstream distance equal to the spacing between the turning vanes and the turbulence rods, a velocity defect of 26% and a wake half-width of $L = 0.25''$ was observed.

The process was as follows: first, a non-dimensional x/D downstream distance was chosen for which the maximum velocity defects for a cylinder and the turning vane wake matched; a matching velocity defect of 26% is seen at $x/D = 4$ (Ong & Wallace, 1996). Then, the expected wake half-width was matched, where this quantity is defined as the lateral distance between the point having the highest velocity defect to a point having half such a velocity defect. The expected half-width from the turning vane simulation was $L = 0.25''$. A half-width of $L = 0.7D$ was seen at the pre-determined x/D value. Therefore, a rod that would produce the wake of the desired characteristics would have a diameter of $D = 0.179''$; the closest standard rod size was 0.1875" in diameter, so this dimension was chosen instead for the sake of expedience. This rod was then placed 0.75" upstream of the turbulence grid in order to mimic the effects of the turning vane wake.

Two separate upstream rod configurations were tested. In the first, the rod was placed directly upstream of one of the rods in the turbulence grid (Figure 4.11). In the other, the rod was placed directly upstream of the center of the space between two rods in the turbulence grid; this was done to see if one configuration provided more favorable

results than the other (i.e. a lesser degree of wake influence on the downstream grid-generated turbulence). It was hypothesized that the interaction of the already turbulent simulated turning vane wake would cause a region of increased turbulence intensity, since a turbulent flow was to pass through a device specifically designed to further increase turbulence intensity in a mainstream flow.

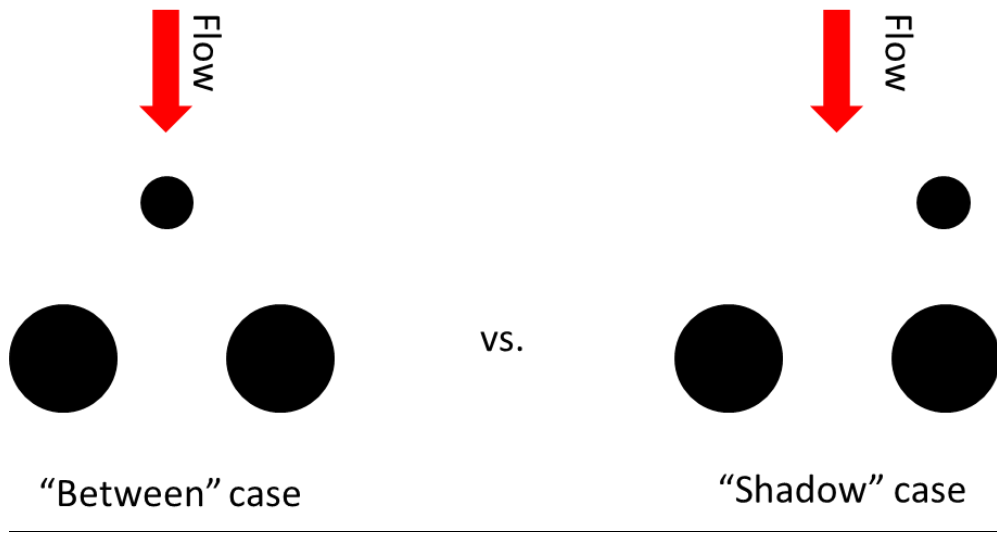


Figure 4.11: Two wake simulation rod placements used in the wake destruction test

Contrary to expectations, the region downstream of the wake simulating rod's centerline (shown by the vertical dashed line in Figure 4.12) showed lower-than-nominal turbulence intensity. This could be explained by the fact that the velocity defect coming from the wake would create a velocity gradient passing through the turbulence rods of lesser magnitude than the one produced without the turning vane wake simulator present. The reduced shear would in turn mean less production of turbulent kinetic energy and correspondingly reduced apparent turbulence intensity. Another interesting result is that the lateral placement of the wake generator had no apparent effect on the turbulence intensity profile. This was expected to be due to the relatively large downstream distance

from the turbulence generator at which these measurements were made; the merging turbulence rod wakes could have eliminated any evidence of different flow attributes between the two cases due to the enhanced transport downstream of the grid.

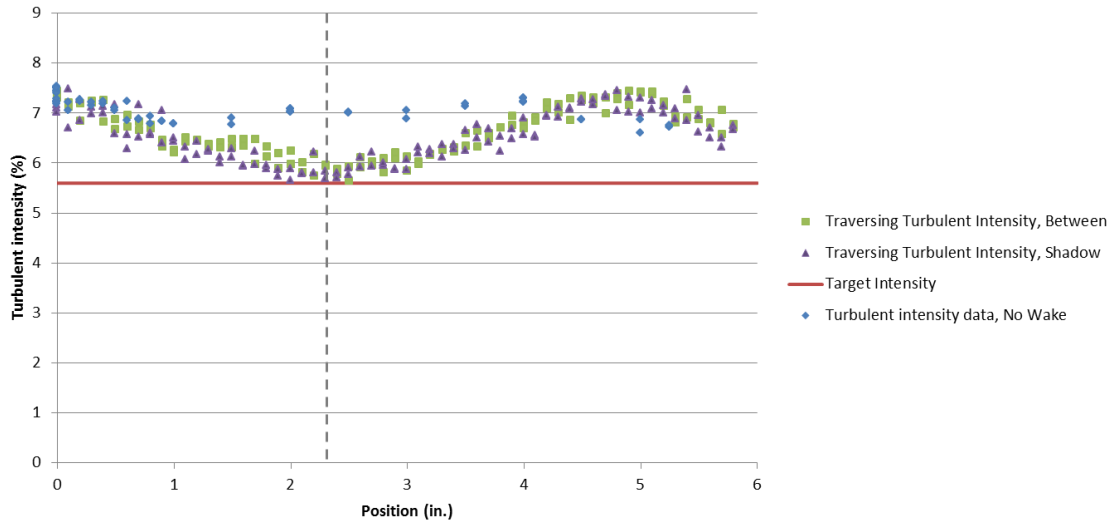


Figure 4.12: Effect of an upstream wake on grid-generated turbulence intensity uniformity

It is worth mentioning that the previously discussed dip in turbulence intensity is fairly significant—at this downstream distance, it represents a roughly 15% decrease from the nominal value. Depending on the needs of a given experiment, this could be unacceptable. However, it is important to note that this effect could be artificially magnified due to the experimental setup: the wake generator is placed within two turbulence rod diameters upstream of the generator, which is a fairly short distance. It is hypothesized that this relative closeness of the grid to the turning vane simulator could affect the flow field in the region of the turning vane simulator, which could in turn affect its wake width and strength. The presence of these items in the flow field might create an area of locally increased flow obstruction, thereby reducing the amount of flow passing through some of the turbulence rods. This local reduction in flow rate could decrease the

velocity gradient between the grid rods' wakes and the flow passing between them, decreasing turbulence production in this region. Since the actual turning vanes in the wind tunnel facility are to be placed significantly further upstream of the grid, this effect is not expected to be present. Therefore, the results from this experiment are considered to be the worst-case scenario for a wake's effect on downstream turbulence intensity.

4.1.6 Approach Flow Test Conclusions

It was shown in this set of experiments that the angle at which the turbulence generator is placed with respect to the approach flow does affect the turbulence quantities downstream. It was demonstrated that the turbulence intensity increases monotonically with the magnitude of the offset angle, and that this increase cannot be accounted for by the change in projected grid solidity alone. Two mechanisms were proposed by which the turbulence intensity could be increased due to the grid angle; both involved a greater rate of turbulence production by means of an increased mean velocity gradient in comparison to the normal-flow case. It was also observed that the average turbulence integral length scale increased with increasing grid angle, although evidence for a strict monotonic trend was not as strong as for the case of the turbulence intensity. As of the time of the writing of this document, no likely physical cause for this phenomenon has been hypothesized.

It was observed that the addition of a wake from a cylinder (intended to simulate a turning vane wake) upstream of the turbulence generator suppressed the turbulence level downstream of the grid. This result was contrary to the hypothesized effect prior to running the experiment. It was proposed that this was due to the velocity defect in the

simulated vane wake entering the turbulence rods created a local decrease in the mean velocity gradient, causing less turbulence to be generated by the grid.

4.2 Investigation of Total Pressure Losses within Different Segments of a Closed-Loop Wind Tunnel

The test article for the TTCRL's upcoming wind tunnel facility required a Reynolds number that would yield an approach flow mean velocity of $\bar{U} = 10.8$ m/s at the specified test temperature. Although it was possible to attain this velocity within the test section of the current facility, the new test section was to be 20% wider. This corresponded to a mass flow rate that would require a mean velocity of $\bar{U} = 13$ m/s in the approach flow, which was above the upper limit of what could be reached in the existing facility. Since the documentation provided by the wind tunnel OEM indicated that a velocity of 25 m/s was possible for a cross-section of the same area as the existing test section, an investigation was conducted to determine which portions of the wind tunnel were responsible for the greatest total pressure loss, and therefore the lower than expected maximum test section velocity.

Pitot-static probes were placed at a variety of mid-span locations along the path of the tunnel (Figure 4.13). A simple red dot indicates a probe that has been put through the tunnel ceiling; a red dot with a line indicates a probe that was placed through a tunnel wall. Total and static pressure were measured on separate pressure transducers with respect to atmosphere so that they could either be evaluated individually or converted to a dynamic pressure by which a local velocity could be measured. The total pressure rise across the fan was measured so that the pressure drops across the different sections of the tunnel could be expressed as a percentage of the total (Table 4.3).

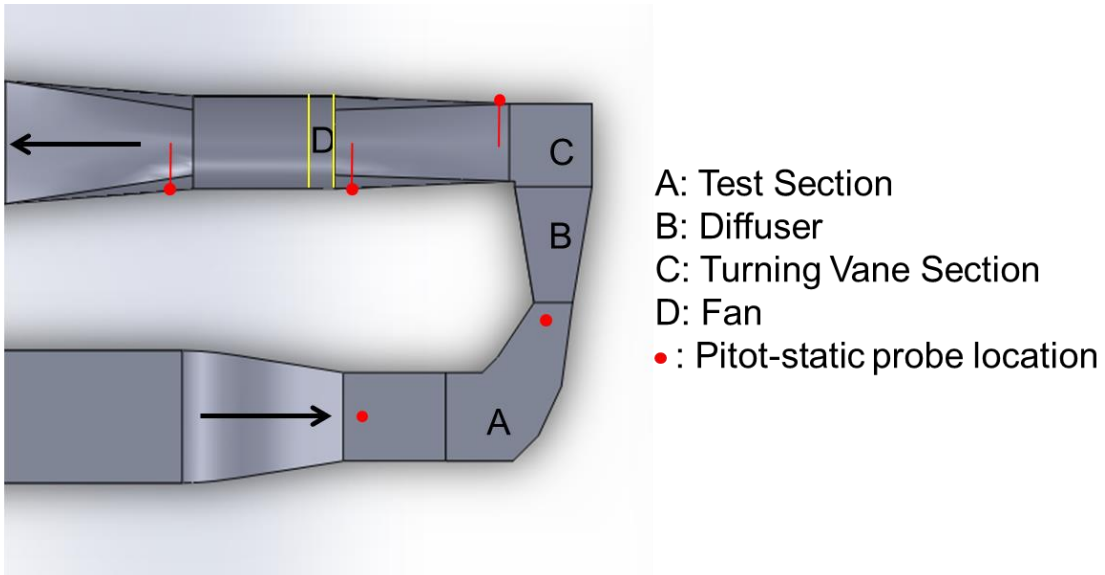


Figure 4.13: Probe locations for wind tunnel total pressure loss measurements

Section	Total Pressure Change (inAq)	Fraction of Tunnel Pressure Loss
Fan	+6.0	N/A
Diffuser and Turning Vanes	-5.2	87%
Test Section	-0.4	7%

Table 4.3: Total pressure losses within wind tunnel sections

It is immediately apparent that the diffuser section and corner turning vane section were responsible for the greatest portion of the total pressure losses within the tunnel. This is partly in line with expectations, since the diffuser inlet is the section with the greatest flow velocity in the tunnel loop. (The turning vane section would not be expected to produce much total pressure loss, but the experimental setup did not permit the individual total pressure measurement of this section.) However, a properly functioning diffuser (i.e. one not experiencing significant separation) would be expected to perform much better than was being observed; there were two other diffuser sections in

the wind tunnel, with neither being responsible for significant total pressure loss. These facts gave rise to the concern that the diffuser section was not functioning as designed.

It is worth mentioning that it is difficult to pick a single value for the total pressure that was measured at the exit of the turning vanes downstream of the diffuser as being representative. There was significant variation in the total pressure and the velocity in this section—the velocities calculated within this region were significantly higher than the mean velocity at that wind tunnel cross-section (Figure 4.14), which was calculated based on mass conservation through the wind tunnel. Since the measurement line did not reach across the entire width of the corner section, velocities must have been lower in other regions of the cross-section in order for the mass flow rate to be correct. The elevated velocity that was measured was likely due to the wide-angle diffuser not effectively decelerating the flow—the high momentum flow exiting the center of the diffuser could then not be adequately turned by the corner turning vanes, and ultimately was caused to change direction by the tunnel wall. This would account for the vastly increased velocity closer to the outside tunnel wall; if the diffuser was performing inadequately, then this would account for the decreased velocity near the top and bottom of the cross-section that would be required to balance the mass flow rate at this location.

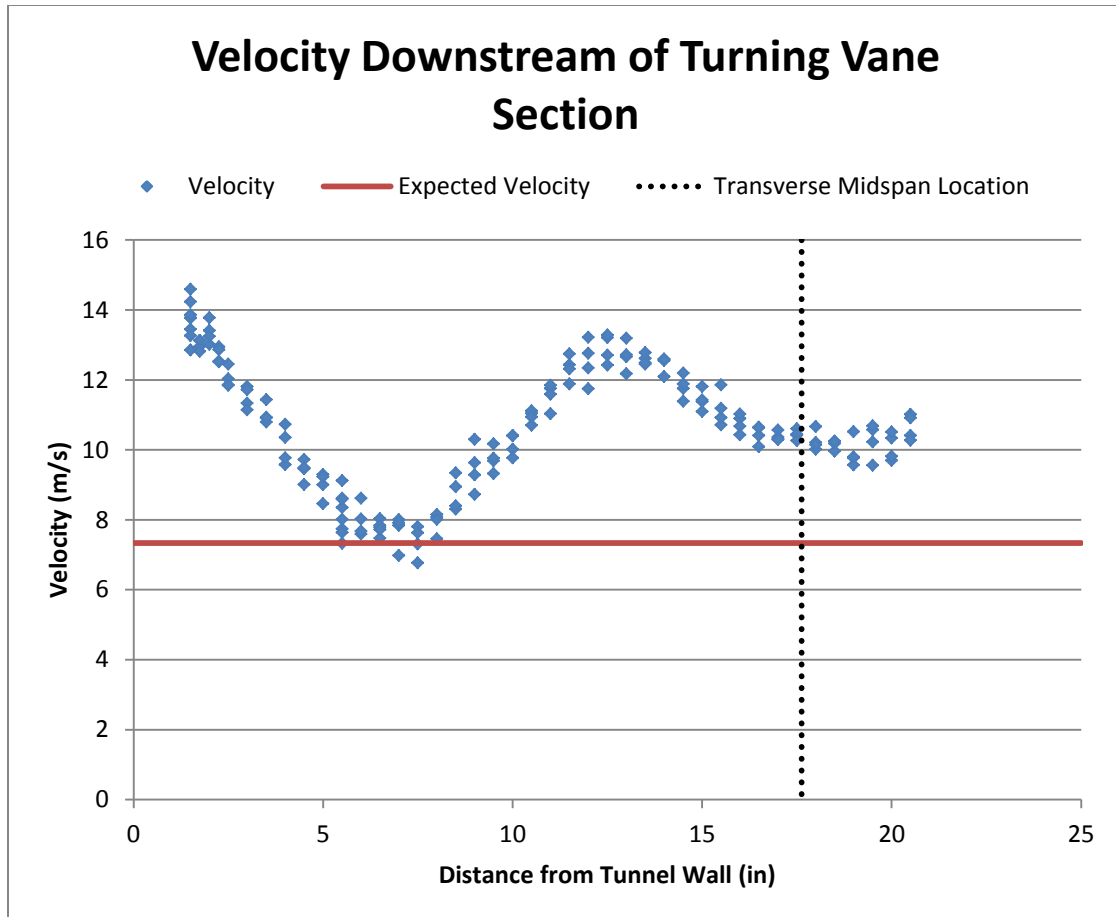


Figure 4.14: Velocity downstream of turning vane section deviates from the expected value

Since it was evident that the diffuser section downstream of the test section was performing inadequately at the required wind tunnel mass flow rate, it was deemed necessary to replace this diffuser. The design process for this new diffuser is outside of the scope of this text.

4.3 Design of a Coolant Flow Loop Based on Test Article Blowing Ratio Requirements

A coolant flow loop was designed for a test facility that would be able to accommodate a test article having three internal coolant channels. The flow loop was

designed to deliver an amount of flow that would satisfy the blowing ratio requirements for each of the film cooling hole rows. The blowing ratios and row locations were specified by engineers at the project's sponsor company, Pratt & Whitney.

Estimations of mass flow rate through the three channels were made by first estimating the flow out of a single hole at a given location based on its individual blowing ratio:

$$\dot{m}_{hole} = \rho_c u_c A_h = \rho_\infty u_\infty A_h M_{hole} \quad (4.8)$$

However, since the blowing ratio in this case is a local quantity rather than an averaged one, it is necessary to obtain the mainstream velocity at each hole location. Depending on the chord-wise location of the hole, this local velocity could be significantly greater than the velocity of the approach flow. This velocity was estimated using 2-D CFD: the static pressure profile on the blade wall was exported from FLUENT and subtracted from the total pressure in the approach flow. The difference between the pressure at a row x/C location and the approach flow total pressure was interpreted to be the dynamic pressure at the given x/C location. This dynamic pressure was converted to an equivalent local flow velocity using the standard method for incompressible flows:

$$u_\infty = \sqrt{\frac{2(P_{total,\infty} - P_{static,hole})}{\rho}} \quad (4.9)$$

Next, the number of holes in each row was determined. The non-dimensional hole pitch for each row p/d was given by the sponsor company, as was the diameter, d , so these holes could be spaced into rows. Since the height of the test article $h = 21.6''$ was known, the height of the hatch (on which all of the holes were to be machined) was set to

be 17.6" based on previous successful vane model designs. The number of holes for each row was then simply the maximum integer number of pitches, p , which could fit on the hatch. Therefore, the mass flow exiting each internal channel was equal to the sum of the mass flow of each row that was a part of the channel, which in turn was simply the mass flow of a given hole in a given row multiplied by the number of holes in that row.

The final estimated mass flow calculations were 74.2 g/s for the first passage, 30.3 g/s for the second passage, and 33.4 g/s for the third passage of the new test article, totaling 137.9 g/s for the entire test article.

As previously stated, the test article to be used in the new facility was to have three internal coolant passages; since the coolant loop in the existing facility accommodated only two channels, at the minimum, the existing piping needed to be modified to add another channel. In order to determine if this was an adequate solution, a test was performed in which the maximum flow rate through each of the coolant channels was determined. This test was performed with the same vane test article in place that was used for the tests presented in Chapter 3. The coolant passing through the flow loop was of comparable density to the coolant in a typical test, and the wind tunnel mainstream velocity was likewise set to be close to future test conditions. Under these conditions, the coolant flow loop was capable of supplying only 85 g/s in the fore passage and 27 g/s in the aft passage. The maximum flow rate through the aft passage was not significantly increased upon removing the fore passage flow. The total flow rate through the existing coolant loop was therefore deemed insufficient, leading to the design of a new flow loop.

In order to determine which part of the flow loop would benefit most from redesign, the total pressure losses across different sections of the flow loop were measured. Pressure taps were installed immediately up- and downstream of the heat exchanger; pressures were also measured in the vane plenum and within the tunnel near the vane to approximate the pressure drop through the internal channels and film holes of the vane. This allowed for loss measurements to be taken for three sections: the heat exchanger; a long length of pipe including the orifice plates; the internals of the vane. It was found that 64% of the pressure loss was through the simple PVC pipe section, prompting a redesign focus on this section.

It is worth mentioning that one drawback of the investigation of maximum flow rate is that the total pressure loss between the plenum and the exit of the film cooling holes was not necessarily representative of the total pressure losses within the same region for the new blade model that was to be tested. Since the maximum flow rate that can be produced in a piping system for a given pressure difference is a function of all of the losses within the system, it is possible that if the pressure losses within the new blade were significantly higher than in the vane that was tested, a piping system could be put into place that would not satisfy the flow rate requirements. Therefore, the piping system was designed to have a significant margin in maximum flow rate in order to prevent this uncertainty in the pressure losses in the blade model from causing issues once the new test section and coolant piping system was built.

The piping system was designed based on a maximum allowable pressure drop of 16 inAq across the piping between the heat exchanger and the new test article plenum; this number was based on actual pressure availability during the maximum flow rate test.

The rest of the pressure differential supplied by the blower would be “spent” on pushing flow through the heat exchanger and the plenum and test article internal passages. The maximum flow rate through individual passages in the coolant loop being designed was calculated by using the maximum allowable pressure drop and the sum of the individual loss coefficients, K , of each component being tested. Where available, the loss coefficients were obtained from literature supplied by the OEM of each of the parts (e.g. NIBCO, the manufacturer of the gate valve). Otherwise, K values for PVC pipe and pipe fixtures were obtained from standard fluid flow text books. Each of the pipe circuits is to be constructed of 3” schedule 40 PVC pipe; this increase in diameter from 2.5” would have the effect of reducing losses by close to 50% for a given mass flow rate due to the decrease in flow velocity inside of the pipe. Ultimately, the design was completed such that a 57% margin in flow rate was possible through all of the channels for the expected maximum pressure drop.

4.4 Conclusions and Recommendations Regarding Total Pressure Measurements for Wind Tunnel Redesign

An investigation into total pressure losses within the closed-loop wind tunnel was prompted when it was discovered that the wind tunnel was unable to produce mainstream velocities comparable to manufacturer specifications. The total pressure measurement experiments uncovered severe losses in the diffuser and turning vane sections just downstream of the test section, which accounted for 87% of the pressure losses within the tunnel. Subsequent total and static pressure measurements downstream of this region indicated that the diffuser was not successfully decelerating the flow, and consequently required a redesign. A recommendation for future wind tunnel diffuser designs would be to take care in designing a large-angle diffuser and use data presented in the academic

literature to reduce the total pressure drop through the section, allowing the wind tunnel to achieve a higher level of performance.

The secondary flow loop was redesigned to increase the mass flow rate of coolant that could be delivered to a test article to be used in a new wind tunnel test section. The maximum mass flow rates of the existing secondary flow loop were measured for reference, and it was determined that the flow rates were insufficient to support the needs of the new test article. A new flow loop was designed with pipes of a greater area to decrease total pressure losses; losses and maximum flow rate through separate sections of the new flow loop design were calculated using loss coefficients that were presented in reference texts or provided by the equipment manufacturers.

References

- Albert, J. E. (2003). *Adiabatic and Overall Effectiveness Measurements of a Forward-Diffused Film Cooling Configuration for a Turbine Blade Leading Edge*. Austin: The University of Texas at Austin.
- Albert, J. E. (2011). *Experimental Simulation and Mitigation of Contaminant Deposition*. Austin: The University of Texas, PhD Dissertation.
- Albert, J. E., Bogard, D. G., & Cunha, F. (2004). Adiabatic and Overall Effectiveness for a Film Cooled Blade. *Proceedings of ASME Turbo Expo 2004*, 1-9.
- Anderson, J. B. (2013). *Calibration of Orifice Plates used in the Large Tunnel*. Austin: Internal TTCRL Report.
- Baines, W. D., & Peterson, E. G. (1951). An Investigation of Flow through Screens. *Transactions of the ASME*, 467-477.
- Bangert, B. A., Kohli, A., Sauer, J. H., & Thole, K. A. (1997). High Freestream Turbulence Simulation in a Scaled-Up Turbine Vane Passage. *IGTI*.
- Bunker, R. S. (2009). The Effects of Manufacturing Tolerances on Gas Turbine Cooling. *Journal of Turbomachinery*, 1-11.
- Comte-Bellot, G. (1976). Hot-Wire Anemometry. *Annual Review of Fluid Mechanics*, 209-231.
- Cutbirth, J. M. (2000). *Turbulence and Three-Dimensional Effects on a Film Cooled Turbine Vane*. Austin: The University of Texas at Austin.
- Dagdas, A. (2009, November 1). *Brayton Cycle: The Ideal Cycle for Gas Turbines*. Retrieved October 26, 2013, from <http://www.yildiz.edu.tr/~dagdas/Brayton%20cycle.pdf>
- Dagdas, A. (n.d.). *Brayton Cycle: The Ideal Cycle for Gas Turbines*. Retrieved October 26, 2013, from <http://www.yildiz.edu.tr/~dagdas/Brayton%20cycle.pdf>
- Davidson, F. T., Kistenmacher, D. A., & Bogard, D. G. (2012). Film Cooling with a Thermal Barrier Coating: Round Holes, Craters, and Trenches. *Proceedings of ASME Turbo Expo 2012*, 1-12.
- Davis, G. d. (1962). The Flow of Air Through Wire Screens. *Proceedings of the 1st Australasian Conference on Hydraulics and Fluid Mechanics*, 191-212.

- Dees, J. (2010). *Experimental Measurements of Conjugate Heat Transfer on a Scaled-up Gas Turbine Airfoil with Realistic Cooling Configuration*. Austin: The University of Texas at Austin.
- Dees, J. E. (2011). *C3X Heat Transfer Database*. Austin: Internal TTCRL Report.
- Dyson, T. E. (2012). *Flow split predictions for showerhead*. Austin: TTCRL internal document.
- Han, J.-C., Dutta, S., & Ekkad, S. (2013). *Gas Turbine Heat Transfer and Cooling Technology*. Boca Raton: CRC Press.
- Hoffman, J. M. (2002, December 12). *Cool Coatings Let Engines Run Hotter*. Retrieved 10 20, 2013, from Machine Design: <http://machinedesign.com/archive/cool-coatings-let-engines-run-hotter>
- Ito, S., Goldstein, R. J., & Eckert, E. R. (1978). Film Cooling of a Gas Turbine Blade. *Journal of Engineering for Power*, 476 - 481.
- King, L. V. (1914). On the Convection of Heat from Small Cylinders in a Stream of Fluid: Determination of the Convection Constants of Small Platinnum Wires, with Applications to Hot-Wire Anemometry. *Proceedings of the Royal Society A*, 563-570.
- Kistenmacher, D. A., Davidson, F. T., & Bogard, D. G. (2013). Realistic Trench Film Cooling with a Thermal Barrier Coating and Deposition. *Proceedings of ASME Turbo Expo 2013: Turbine Technical Conference and Exposition*, 1-14.
- Koutmos, P., & McGuirk, J. (1989). Isothermal Flow in a Gas Turbine Combustor - A Benchmark Experimental Study. *Experiments in Fluids*, 344- 354.
- Laws, E. M., & Livesey, J. L. (1978). Flow Through Screens. *Annual Review of Fluid Mechanics*, 247-266.
- MatWeb. (2013). *304 Stainless Steel Property Data*. Retrieved November 9, 2013, from MatWeb - The Online Materials Information Resource: <http://www.matweb.com/search/DataSheet.aspx?MatGUID=abc4415b0f8b490387e3c922237098da&ckck=1>
- McClintic, J. (2013). *Experimental Investigation of Overall Effectiveness and Coolant Jet Interactions on a Fully Cooled C3X Turbine Vane*. Ausint: University of Texas at Austin.
- Mehta, R. D. (1977). The Aerodynamic Design of Blower Tunnels with Wide-Angle Diffusers. *Progress in Aerospace Sciences*, 59-120.

- Moran, M. J., & Shapiro, H. N. (2008). *Fundamentals of Engineering Thermodynamics*. Hoboken: John Wiley & Sons, Inc.
- Nathan, M. L. (2011). *Adiabatic and Overall Effectiveness in the Showerhead of a Film Cooled Turbine Vane and Effects of Surface Curvature on Adiabatic Effectiveness*. Austin: The University of Texas at Austin.
- Ong, L., & Wallace, J. (1996). The Velocity Field of the Turbulent Very Near Wake of a Circular Cylinder. *Experiments in Fluids*, 441-453.
- Pederson, D. R., Eckert, E. R., & Goldstein, R. J. (1977). Film Cooling with Large Density Differences Between the Mainstream and the Secondary Fluid Measured by the Heat-Mass Transfer Analogy. *Transactions of the ASME*, 620-627.
- Pichon, Y. (2009). *Turbulence Field Measurements for the Large Windtunnel*. Austin: TTCRL Internal Report.
- PipeBid. (n.d.). *Thermal Contraction and Expansion*. Retrieved November 9, 2013, from http://www.pipebid.com/faq/pvc_pipe_thermal_expansion_guide.pdf
- Polanka, M. D. (1999). *Detailed Film Cooling Effectiveness and Three Component Velocity Field Measurements on a First Stage Turbine Vane Subject to High Freestream Turbulence*. Austin: The University of Texas at Austin.
- Radomsky, R. W., & Thole, K. A. (1999). Flowfield Measurements for a Highly Turbulent Flow in a Stator Vane Passage. *Journal of Turbomachinery*, 255-262.
- Research and Innovative Technology Administration. (2012). *Airline Fuel Cost and Consumption (U.S. Carriers - Schedules)*. Washington: Bureau of Transportation Statistics.
- Roach, P. E. (1987). The Generation of Nearly Isotropic Turbulence by Means of Grids. *International Journal of Heat Transfer and Fluid Flow*, 82-92.
- Sinha, A. K., Bogard, D. G., & Crawford, M. E. (1991). Film-Cooling Effectiveness Downstream of a Single Row of Holes with Variable Density Ratio. *Transactions of the ASME*, 442-449.
- Special Metals. (2004, September 4). *Inconel alloy X-750 Specification Sheet*. Retrieved October 26, 2013, from Special Metals: <http://www.specialmetals.com/documents/Inconel%20alloy%20X-750.pdf>
- Tavoularis, S. (2009). *Measurement in Fluid Mechanics*. New York: Cambridge University Press.

Taylor, G. I., Batchelor, G. K., Dryden, H. L., & Schubauer, G. B. (1947). The effect of wire gauze on small disturbances in a uniform stream. *Quarterly Journal of Mechanics and Applied Mathematics*, 1-29.

U.S. Energy Information Administration. (2012). *Annual Energy Review*. Washington.

YXLON. (2011). *Inspecting Turbine Blades Non-Destructively*. Retrieved 10 20, 2012, from YXLON Turbine Blades: <http://www.yxlon.com/Applications/Cast-parts/Turbine-blades>

Vita

Noah Mosberg was born and grew up in Ann Arbor, Michigan; he left town in 2008 to go to Northwestern University in Evanston, Illinois, from which he graduated in 2012 as a Bachelor of Science. He decided to continue his formal education at the University of Texas at Austin by getting a Master of Science in mechanical engineering, focusing on thermal/fluid systems. Here, he worked in the lab of Professor David Bogard, where he completed the research that culminated in the writing of this thesis. He plans on moving on to full-time employment where he will be able to continue expanding his knowledge of fluid mechanics and heat transfer (or at least get by, feed himself, and shelter himself).

Permanent e-mail: noahmosberg2012@u.northwestern.edu

This thesis was typed by the author.